Calorimetry at the International Linear Collider: From Simulation to Reality

Dissertation
zur Erlangung des Doktorgrades
des Department Physik
der Universität Hamburg

vorgelegt von
Nanda Wattimena
aus Hamburg

Hamburg
2009

Gutachter/in der Dissertation: Dr. Erika Garutti
                                        Prof. Dr. Peter Schleper

Gutachter/in der Disputation: Dr. Erika Garutti
                                        Prof. Dr. Joachim Mnich

Datum der Disputation: 12. Februar 2010

Vorsitzende des Prüfungsausschusses: Prof. Dr. Caren Hagner
Vorsitzender des Promotionsausschusses: Prof. Dr. Robert Klanner

Leiter des Departments Physik: Prof. Dr. Joachim Bartels
Dekan der MIN-Fakultät: Prof. Dr. Heinrich Graener

Abstract

Calorimetry plays a crucial role in ongoing and upcoming high-energy physics experiments. To build a powerful calorimetric system with a performance tailored to the expected physics signatures, demands dedicated research and development of new readout technologies as well as dedicated reconstruction algorithms.

The presented design of a calorimetric system which meets the high demands of precision physics at the future linear collider ILC, follows the paradigm of particle flow. Particle flow is a reconstruction principle that relies on a calorimetric system with high spatial granularity. In the detector optimisation process, the development of hardware and software are interlinked and cannot be judged independently.

This thesis addresses two different aspects of detector optimisation, a test of the detector design against one example physics scenario and the development of a stable calibration procedure.

In the first part, a gauge-mediated Supersymmetry breaking scenario is used to test the design of the electromagnetic calorimeter in a full detector simulation study. The reconstruction of the neutralino properties, each decaying into a photon and a gravitino, requires a good energy resolution, as well as excellent position and angular resolution. The error bounds on the neutralino mass is strongly linked to the energy resolution, while the position and angular reconstruction of neutral particles is essential for the determination of the neutralino lifetime.

The second part of this thesis focuses on the calibration procedure for a prototype of the hadron calorimeter. 7608 novel photodetectors are operated and tested in this prototype. They are exposed to beams of well defined particle type and energy. The calibration is tested with a detailed study of electromagnetic showers inside the cubic-metre-sized prototype, with special attention paid towards the non-linearity correction.

Zusammenfassung

In laufenden und zukünftigen Hochenergiephysikexperimenten spielt Kalorimetrie eine entscheidende Rolle. Die Entwicklung neuer Kalorimeter, die auf die erwarteten Signaturen optimiert sind, erfordert sowohl die Erforschung neuer Auslesetechnolgien, als auch die Entwicklung spezialisierte Rekonstruktionsalgorithmen.

Das Design eines Kalorimetersystems mit dem die hohen Präzisionsansprüche an Messungen an einem zukünftigen Linearbeschleuniger, wie z. B. dem ILC, erfüllt werden können, basiert auf dem „Particle Flow" Prinzip. Diese Rekonstruktionsphilosophie beruht auf einem Kalorimetersystem mit hoher räumlicher Auflösung. Im Rahmen der Detektoroptimierung gehen die Entwicklung von Hard- und Software Hand-in-Hand, so dass beide Bereiche gemeinsam beurteilt werden müssen.

Diese Arbeit behandelt zwei unterschiedliche Gesichtspunkte der Detektoroptimierung. Zum einen wird das Detektordesign anhand eines physikalischen Szenarios untersucht, des weiteren wird eine stabile Kalibrierungsmethode für einen Detektorprototypen entwickelt.

Im ersten Teil werden die Anforderungen an das elektromagnetische Kalorimeter werden anhand einer vollen Detektorsimulation überprüft. Dabei werden die Eigenschaften von Neutralinos bestimmt, die jeweils in ein Gravitino und ein Photon zerfallen. Dieses Szenario ist Teil einer supersymmetrischen Theorie, in der die Symmetriebrechung durch Eichwechselwirkungen übertragen wird. Die Photonen aus dem Neutralinozerfall müssen mit guter Energie-, Positions-, und Winkelauflösung gemessen werden. Die Genauigkeit mit der die Messung der Neutralinomasse erfolgen kann, hängt von der erreichten Energieauflösung ab. Die Positions- und die Winkelauflösung bestimmen den Fehler bei der Lebensdauermessung.

Im zweiten Teil wir die Kalibrierung eines Prototypen des hadronischen Kalorimeters untersucht. In diesem Prototypen werden 7608 neuartige Lichtsensoren verschiedenen Strahlen bekannter Energie und Teilchenart ausgesetzt. Es wir das Ansprechverhalten auf elektromagnetische Schauer untersucht, das zur Bestätigung der Kalibrierung, insbesondere der Korrektur des nicht-linearen Verhaltens der SiPM, dient.

Contents

1 Introduction

The Standard Model of particle physics describes all known matter particles and the interactions between them. However, the Standard Model cannot be the theory of everything. Application of the laws of the smallest scales to the biggest experiment, the universe, reveals that the Standard Model particles can only describe a tiny fraction of the matter surrounding us. The most popular extension of the Standard Model that enables a better agreement between particle physics and cosmological observations is Supersymmetry (SUSY). The constituents of SUSY are expected to reveal themselves around the TeV scale.

In order to study this new phenomena with great precision a lepton collider should be constructed. It should have a high enough centre of mass energy to discover at least the majority, if not all of the expected new particles. The International Linear Collider (ILC), a proposed electron - positron collider with centre-of-mass energy up to $\sqrt{s} = 1\,\text{TeV}$, could fulfil these demands.

In addition, to perform precision measurements a detector with high resolution is essential. The International Large Detector (ILD) is designed as a multi-purpose detector, with the paradigm of particle flow in mind. The basic idea of particle flow is to utilise the sub-detector with the best possible resolution to reconstruct each single particle in every event, even within dense hadronic jets. The momenta of charged particles are reconstructed in the tracker and only neutral particles are reconstructed in the calorimeters, which have a worse energy resolution up to energies of a few hundred GeV. In contrast to traditional calorimetry, a high lateral and longitudinal granularity of the calorimetric system is of major interest, as this is the only way to separate single particle showers in a dense jet environment.

The successful realisation of the particle flow paradigm requires the development and understanding of calorimeter designs, including new read-out technologies, as well as of sophisticated clustering algorithms. Only the combination of both enables the precise determination of e. g. supersymmetric particle properties.

This thesis covers both topics, the understanding of new calorimeter technologies, as well as that of sophisticated cluster algorithms. The possible discovery and precise determination of one example SUSY scenario is studied in full detector simulation. The analysis poses a challenge to all the electromagnetic performance criteria, i. e. the energy, position and angular resolution. As detector design and software development go hand-in-hand, this analysis is not only used to determine whether the chosen detector geometry is sufficient to perform, only from the calorimeter information, the reconstruction of neutral particle lifetimes. It is also probing the cluster algorithm performance.

Additionally, physics prototypes are built and tested in well defined test beam environments. They serve as proof of principle that the aimed detectors can also be realised and handled in reality. The demanded high granularity requires new read-out technologies, e. g. silicon based pixelated devices for the hadron calorimeter. One

important step is the investigation of the calorimeter prototype characteristics at the electromagnetic scale, which serves as calibration validation and is a measure for the detector understanding.

This thesis is organised as follows. After a short description of the Standard Model of particle physics, its problems and Gauge Mediated Supersymmetry Breaking as a possible solution in chapter 2, the International Linear Collider and the International Large Detector are introduced in chapter 3. The principles of calorimetry are important for both presented analyses, and therefore presented in chapter 4. Afterwards, the reconstruction of the next-to-lightest SUSY particle properties are discussed in chapter 5. The introduction of the physics prototype of a hadron calorimeter in chapter 6, is followed by the analysis of electromagnetic showers in the same detector in chapter 7. Finally, the thesis in summarised and concluded in chapter 8.

2 The Standard Model and Beyond

The Standard Model of particle physics (cf. section 2.1) describes the fundamental matter particles and the interactions between them. It has successfully passed a plethora of experimental tests since it was first described 40 years ago [1, 2, 3]. Still it is not satisfactory since many questions remain open (cf. section 2.2). Therefore, theorists came up with a huge variety of extensions of the Standard Model, the most popular one being the so-called Supersymmetry (cf. section 2.3).

2.1 The Standard Model

The elementary particles in nature (that we are aware of) can be categorised by an intrinsic property called spin. All particles have spin in integer multiples of 1/2. Matter building particles possess an odd multiple and are named fermions. They can again be ordered in two groups (leptons and quarks), depending on the forces that act on them. Three generations exist in each group. While particles within one generation differ in their quantum numbers, especially in their electric charge, the corresponding particles of different generations have identical quantum numbers, but differ in their masses. In addition, every particle has a partner with the same mass, but opposite quantum numbers, its anti-particle.

Four fundamental forces act on these matter building particles: gravity, electromagnetism, the weak and the strong force. They are mediated by force carrying particles with integer spin, called bosons, that couple to the matter building particles and sometimes also to each other. The carrier of the electromagnetic force, the photon γ, couples to all particles with electric charge, i.e. to all fermions except the neutrinos, and to the $W^{\pm}$-bosons. The weak force has three mediating particles: two charged W-bosons and one electrically neutral Z-boson. All of them couple to every matter building particle and in addition the $W^{\pm}$-bosons couple to themselves. Gluons are mediators of the strong force. They appear in eight different colour states and couple to coloured particles, which means to all quarks and to each other. Finally, all particles are subject to gravity. Which, although first described by I. Newton in the 17th century, and later on described much more precisely by A. Einstein in the form of general relativity, cannot be included in the Standard Model up to now.

The name, symbol, mass, electric charge and spin of all matter building particles and force carriers of the Standard Model are summarised in figure 2.1.

2.1.1 Groups and Symmetries

The Standard Model is based on the principle of local gauge invariance. It was first described for electroweak interactions by S. L. Glashow [1], A. Salam [2] and

Figure 2.1: The Standard Model of particle physics comprises 12 fermionic matter particles (6 quarks and 6 leptons) and 3 forces mediated by bosons [4].

S. Weinberg [3] between 1960 and 1970. Later on H. Fritzsch, M. Gell-Mann and H. Leutwyler [5] extended the theory to the hadronic sector, adding a theory called quantum chromo dynamics (QCD).

As a consequence of local gauge invariance the Lagrangian $\mathcal{L}$, which describes the particle interactions, has to be invariant under certain symmetry transformations. Thus, the forces can be related to certain symmetry groups which describe this invariance.

The symmetry group underlying electromagnetism is a group of unitary 1×1 matrices, and therefore called $U(1)$. The weak force forms an $SU(2)$ and the strong force a $SU(3)$ group. The SU is a special subgroup of U, with the additional constraint that $\det(U) = +1$.

The Lagrangian of electromagnetism

$$\mathcal{L} = i\bar{\Psi}\gamma_\mu \partial^\mu \Psi - m\bar{\Psi}\Psi \tag{2.1}$$

is invariant under the global phase transformation $\Psi'(x) \rightarrow e^{i\alpha}\Psi(x)$, for a constant phase α. The gauge group $U(\alpha) = e^{i\alpha}$ with $\alpha \in \mathbb{R}$ fulfils $U^\dagger U = 1$ and is therefore a unitary group called $U(1)$.

According to E. Noether's theorem [6], any fundamental symmetry has a corresponding conservation law. In this case its the conservation of the electrical current and consequently of the electrical charge. This can be calculated from the infinitesimal transformation $\Psi' = (1 + i\alpha)\Psi$. The resulting variation of the Lagrangian has to

	I_3	Q	Y
ν_L	$1/2$	0	-1
e_L	$-1/2$	-1	-1
e_R	0	-1	-2

Table 2.1: Isospin doublet and singlet for the first lepton generation.

vanish:

$$
\begin{aligned}
\delta\mathcal{L} &= 0 \\
&= \left(\frac{\partial\mathcal{L}}{\partial\Psi}\right)\delta\Psi + \left(\frac{\partial\mathcal{L}}{\partial(\partial_\mu\Psi)}\right)\delta(\partial_\mu\Psi) + \delta\bar{\Psi}\frac{\partial\mathcal{L}}{\partial\bar{\Psi}} + \delta(\partial_\mu\bar{\Psi})\frac{\partial\mathcal{L}}{\partial(\partial_\mu\bar{\Psi})} \\
&= -2\alpha\partial_\mu(\bar{\Psi}\gamma^\mu\Psi).
\end{aligned}
$$

Inserting the electron current density $j^\mu = -e\bar{\Psi}\gamma^\mu\Psi$, one resolves the current conservation

$$
\partial_\mu j^\mu = 0. \tag{2.2}
$$

For local gauge transformations the phase $\alpha(x)$ is a function of space and time: $x_\mu = (t, -\vec{r})$. The first term of equation 2.1 includes the derivative $\partial_\mu\Psi$, which is not invariant under local gauge transformations. To recover gauge invariance the derivative has to be replaced by

$$
\partial_\mu \to D_\mu = \partial_\mu - ieA_\mu, \tag{2.3}
$$

where the gauge field A_μ has to fulfil

$$
A'_\mu = A_\mu + \frac{1}{e}\partial_\mu\alpha(x). \tag{2.4}
$$

Thus, an arbitrary function $\alpha(x)$ can be added to the gauge field without changing the physical observable, which is the characteristic of a photon field. For the electromagnetic Lagrangian the gauge field corresponds to the electromagnetic field.

2.1.2 Mathematical Formulation of the Standard Model

The symmetry group of the Standard Model is

$$
SU(3)_C \otimes SU(2)_L \otimes U(1)_Y. \tag{2.5}
$$

Invariance under colour transformation C is described by an $SU(3)_C$ group. This is the basic gauge group of the strong force, with eight eigenstates corresponding to eight gluons. The gauge group of the electroweak force is $SU(2)_L \otimes U(1)_Y$, where L denotes the invariance under left-handed isospin transformations. The hypercharge $Y = 2(Q - I_3)$ relates the electric charge Q with the third isospin component I_3. The isospin multiplets for the first lepton generation are given in table 2.1

In the mathematical description of the Standard Model particles are represented as fields $\Psi(\vec{x}, t)$ in space and time. The Lagrangian $\mathcal{L}$, describing their evolution, reads

$$
\mathcal{L} = \overline{\Psi}\gamma^\mu D_\mu\Psi - \frac{1}{4}\vec{W}_{\mu\nu}\vec{W}^{\mu\nu} - \frac{1}{4}B_{\mu\nu}B^{\mu\nu} - \frac{1}{4}F^a_{\mu\nu}F^{\mu\nu}_a. \tag{2.6}
$$

It contains the gauge boson kinetic and self-interaction terms

$$\vec{W}_{\mu\nu} = \partial_\mu \vec{W}_\nu - \partial_\nu \vec{W}_\mu + g_2 \vec{W}_\mu \times \vec{W}_\nu$$

and

$$B_{\mu\nu} = \partial_\mu B_\nu - \partial_\nu B_\mu.$$

The coupling constants of $U(1)_Y$ and $SU(2)_L$ are called g_1 and g_2, respectively. B_μ is the gauge boson field associated with the hypercharge, W_μ^i ($i = 1, 2, 3$) are that of the isospin. They mix to the gauge boson mass eigenstates

$$
\begin{aligned}
\gamma &= B \cos\theta_W + W_3 \sin\theta_W, \\
Z &= -B \sin\theta_W + W_3 \cos\theta_W, \\
W^\pm &= (W_1 \mp iW_2)/\sqrt{2},
\end{aligned}
$$

where the weak mixing angle is $\theta_W \approx 28°$.

The gluon kinetic and self-interaction term contains the gluon field strength tensor

$$F_{\mu\nu}^a = \partial_\mu G_\nu^a - \partial_\nu G_\mu^a + g_3 f^{abc} G_{b\mu} G_{c\nu},$$

where G_μ^a denote eight gluon fields and g_3 is the strong coupling constant. The third term is determined by the structure functions f^{abc} ($a, b, c = 1 \ldots 8$) of the $SU(3)_C$ group.

The quark mass eigenstates with isospin $I_3 = 1/2$, namely d_L, s_L and b_L, are mixing to the weak eigenstates d_L', s_L' and b_L' through the unitary Cabibbo-Kobayashi-Maskawa matrix V_{CKM} [7, 8]

$$\begin{pmatrix} d' \\ s' \\ b' \end{pmatrix}_L = V_{\text{CKM}} \begin{pmatrix} d \\ s \\ b \end{pmatrix}_L = \begin{pmatrix} V_{ud} & V_{us} & V_{ub} \\ V_{cd} & V_{cs} & V_{cb} \\ V_{td} & V_{ts} & V_{tb} \end{pmatrix} \begin{pmatrix} d \\ s \\ b \end{pmatrix}_L . \tag{2.7}$$

The factors $|V_{ij}|^2$ give the probability for the transition from $i \to j$. They are close to one for diagonal elements, which makes interactions within one family very likely. Transitions from the third into the second family are suppressed and transitions from the third into the first family even more so. The weak interactions via $W^\pm$-bosons are modified by V_{CKM}, however the neutral-current interactions via the Z-boson and the γ remain unchanged, i.e. there are no flavour-changing neutral currents at tree level.

The fourth force, gravity, results from a gauge invariance as well, namely the invariance under local coordinate transformations. The corresponding gauge mediator is the graviton. However, the theory of gravity, general relativity, is not embedded in the Standard Model of particle physics.

2.1.3 The Higgs Mechanism

The Standard Model Lagrangian as given in equation 2.6 is only gauge invariant for massless fermions and gauge bosons. This is no problem for the electromagnetic force, which is mediated by massless photons over an infinite range, or for the strong force, which despite its limited range of the order of 10^{-15} m, is mediated by massless gluons. However, the weak force carriers do have mass and all fermions are massive, too.

Taken only the experimentally observed ingredients, the Standard Model does not meet the observations, i.e. the observed fermion masses explicitly break the gauge invariance. The currently favoured solution to this problem, first introduced by P. Higgs, is a mechanism which generates particle masses through spontaneous symmetry breaking [9, 10, 11].

In the so-called Higgs mechanism, a doublet of complex fields

$$\mathbf{\Phi} = \frac{1}{\sqrt{2}} \begin{pmatrix} \Phi_2 + i\Phi_1 \\ \Phi_4 + i\Phi_3 \end{pmatrix},$$

comprising a quartet of real fields Φ_i $(i = 1 \dots 4)$ is introduced. This field, called Higgs field, follows a Lagrangian

$$\mathcal{L}_{\text{Higgs}} = \partial_\mu \mathbf{\Phi}^\dagger \partial^\mu \mathbf{\Phi} - V(\mathbf{\Phi}^\dagger \mathbf{\Phi}) \tag{2.8}$$

with a potential

$$V(\mathbf{\Phi}^\dagger \mathbf{\Phi}) = \lambda \left(\mathbf{\Phi}^\dagger \mathbf{\Phi} - \frac{\mu^2}{\lambda} \right)^2 \quad \lambda, \mu \in \mathbb{R}^+, \tag{2.9}$$

which is characterised by a non-zero ground state. Hence, the field does not vanish in the lowest energy states. The value at which the potential is minimal is called the vacuum expectation value v. The choice of one explicit ground state, e.g. $v = +\mu/\sqrt{\lambda}$, spontaneously breaks the original symmetry $V(\Phi) = V(-\Phi)$ of the potential. According to the Goldstone theorem [12], every spontaneous symmetry breaking generates a massless Goldstone boson. But instead of new physical particles, these bosons manifest themselves as longitudinal degrees of freedom for the gauge bosons, giving mass to them.

In addition, there has to be a new particle, the Higgs boson H, which is the only particle postulated by the Standard Model that has not been observed so far. The Standard Model Higgs potential, stated in equation 2.9, is build up in such a way that the Higgs boson can couple to itself with the self-coupling constant λ. Furthermore, it delivers a simple relation between the Higgs boson mass m_H and the Higgs self-coupling:

$$m_H^2 = 2\lambda^2 \tag{2.10}$$

The current lower experimental limit is $m_H > 114.4\,\text{GeV}$ [13] at 95 % confidence level from direct searches at the LEP experiments. Direct searches from the Tevatron experiments exclude the region $163\,\text{GeV} < m_H < 166\,\text{GeV}$ [14] at 95 % confidence level.

Although the Higgs boson has not been directly observed so far, its most probable mass can be obtained from a fit to the electroweak observables via virtual effects, e.g. with GFitter [15]. In figure 2.2(a) the $\Delta\chi^2 = \chi^2 - \chi^2_{\text{min}}$ from a fit to all Standard Model observables, excluding the results from direct Higgs boson searches, is plotted. The preferred Higgs boson mass is $83^{+30}_{-23}\,\text{GeV}$. Figure 2.2(b) illustrates the fit including the results from direct Higgs boson searches. In this case the best estimate for the Higgs boson mass is $116^{+15.6}_{-1.3}\,\text{GeV}$.

2.2 Problems of the Standard Model

Although it is a successfully tested model, there are some open questions that point towards an extension of the Standard Model:
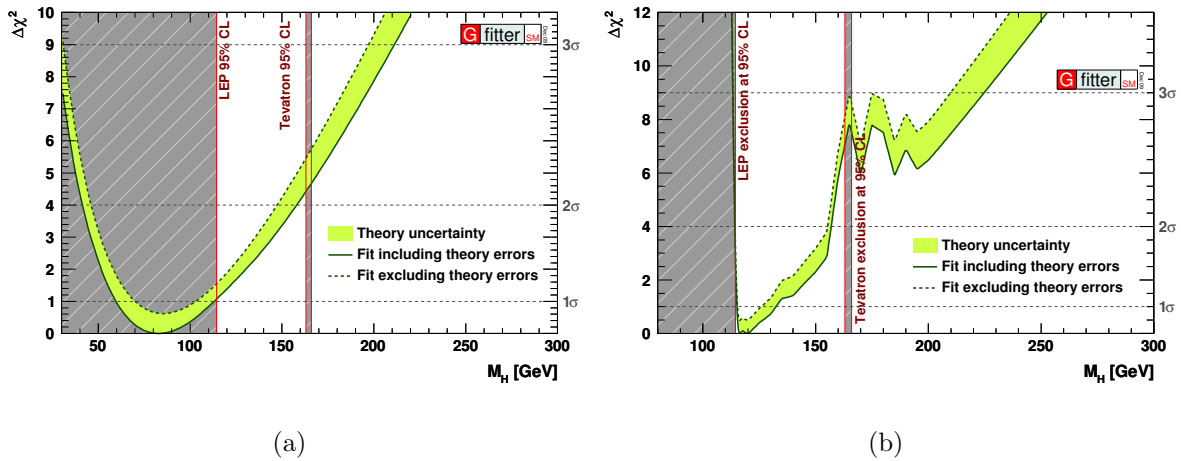
Figure 2.2: $\Delta\chi^2$ from the fit to all electroweak observables as a function of the Higgs boson mass [15] (a) excluding and (b) including results from direct Higgs boson searches. The grey areas are excluded by direct searches. The solid (dashed) line represents the fit result including (excluding) theory errors.

1. a unification of the forces is not possible;

2. the anticipated Higgs boson mass cannot be obtained naturally;

3. the observed matter-antimatter-asymmetry of the universe cannot be explained;

4. gravity is not included;

5. it does not offer any dark matter candidate.

The first problem is addressed in grand unified theories (GUTs) [16]. At high energies all forces are expected to couple with the same strength. But as shown in figure 2.3, a unification of the coupling constants, as required by GUT, is not possible within the Standard Model.

Related to this is the naturalness problem stated in the second item. The Higgs boson mass squared receives quantum corrections from loop effects of every particle that couples to the Higgs boson. The dominant contributions to the self-energy of the Higgs boson are the Higgs, fermion and boson loops sketched in figure 2.4. If the Standard Model is valid up to a scale Λ, the size of these contributions is

$$\Delta m_H^2 \sim \Lambda^2. \tag{2.11}$$

Thus, if the Standard Model is valid up to the Planck scale $\Lambda_{\mathrm{Planck}} = 10^{19}\,\mathrm{GeV}$, the natural Higgs boson mass is $\Lambda_{\mathrm{Planck}}$. To stabilise the Higgs boson mass at the weak scale, it has to be fine-tuned with a precision of $m_H/\Lambda_{\mathrm{Planck}}$, which is 23 orders of magnitude, to cancel quadratic divergences [18].

The third item touches the problem of CP violation. Although all experiments investigating CP violation can be described with high precision and agree with the prediction from the Standard Model, the CP violation is much weaker than the one desired by
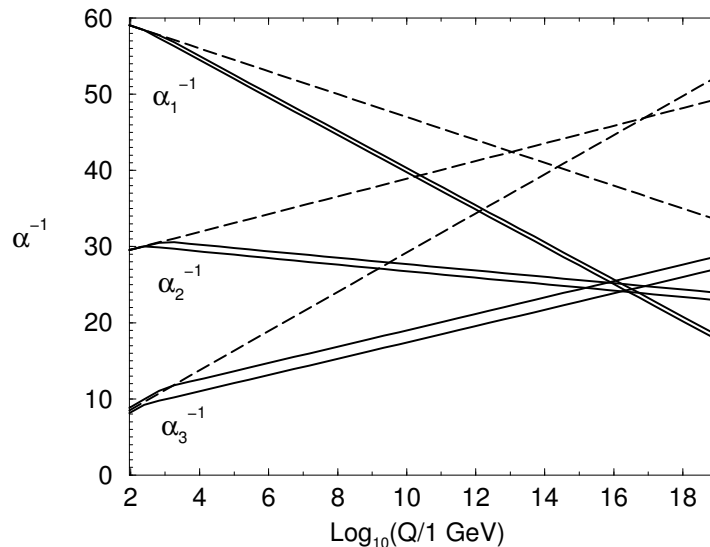
Figure 2.3: Running of the coupling constants ($\alpha_1 \sim$ electromagnetic, $\alpha_2 \sim$ weak, $\alpha_3 \sim$ strong) in the Standard Model (dashed lines) and in the minimal super-symmetric Standard Model (solid lines) as a function of the energy scale [17].

(a)   (b)   (c)
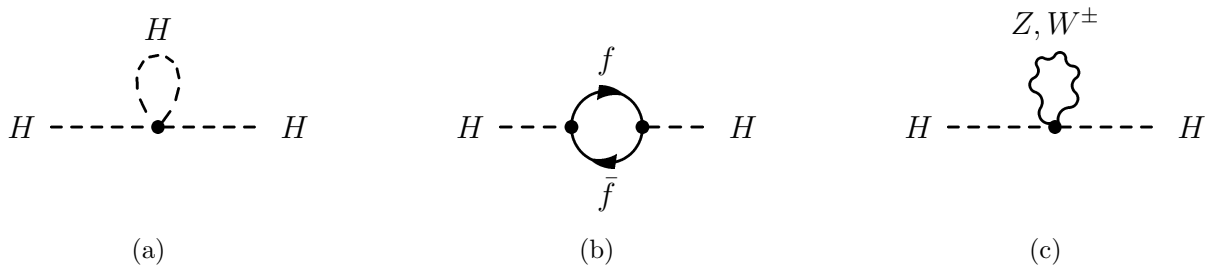
Figure 2.4: Divergent loop contributions to the Higgs boson mass in the Standard Model.

cosmology [19]. Without additional violation matter and anti-matter would have annihilated each other shortly after the Big Bang.

Furthermore, as stated in the fourth item, the Standard Model cannot be the theory of everything, if it does not include gravity. Usually, the gravitational force is weak enough to be neglected in particle physics, but at the Planck scale it should become as strong as the other interactions. At this energy quantum effects of gravity become strong and the theory needs to include gravity.

Finally, cosmological observations of the rotational velocity of galaxies, from gravitational lensing and measurements from the Wilkinson Microwave Anisotropy Probe (WMAP) of the anisotropy in the cosmic microwave background all agree that the matter building particles described so far can only make up about 4 % of the actual energy density of the universe [20]. Almost one quarter of our universe, namely 23 %, should consist of dark matter, the remaining 73 % being dark energy. Dark matter particles may only interact weakly and/or via gravitational interactions. The only Standard Model candidates, the neutrinos, are excluded due to their small mass.

There are several solutions to many of the above mentioned problems on the market [21], e. g. Technicolour [22], where a new strong gauge force binds fermions and

anti-fermions. Some physicists introduce small extra-dimensions [23] to solve the problems. The most popular and best studied proposal is Supersymmetry, which is discussed in the next section.

2.3 Supersymmetry

This section describes the basic idea of Supersymmetry (SUSY) [24] in the context of a minimum extension to the Standard Model. Furthermore, SUSY breaking and the gauge-mediated SUSY breaking mechanism are introduced.

2.3.1 Positron Analogon

Something similar to today's naturalness problem, occurred in classical electromagnetism to the electron mass. In classical electromagnetism, the only dynamical degrees of freedom are electrons, electric and magnetic fields. An electron in the vacuum is surrounded by a Coulomb electric field with energy

$$\Delta E_C = \frac{1}{4\pi\varepsilon_0} \frac{e^2}{r_e},$$

where r_e is the size of the electron, introduced to cutoff the divergent Coulomb self-energy and ε_0 is the permittivity of free space.

Since every electron has this Coulomb self-energy, it has to be considered as part of the electron itself and contributes to the electron mass. If there was only the electron, with an experimentally measured radius of $r_e \lesssim 10^{-15}\,\mathrm{cm}$ the self-energy ΔE_C had to be few GeV and the bare electron mass $(m_e c^2)_{\mathrm{bare}}$ must be negative to obtain the observed electron mass $(m_e c^2)_{\mathrm{obs}}$ with a fine-tuning of

$$
\begin{aligned}
(m_e c^2)_{\mathrm{obs}} &= (m_e c^2)_{\mathrm{bare}} + \Delta E_C, \\
0.000511\,\mathrm{GeV} &= (-3.141082 + 3.141593)\,\mathrm{GeV}.
\end{aligned}
$$

The solution to this problem was found almost eighty years ago by the discovery of the anti-particle to the electron by the discovery of the positron by C. D. Anderson in 1932 [25]. This discovery doubled the degrees of freedom in classical electromagnetism. Electrons and positrons can be produced in pairs and annihilate each other and the resulting vacuum fluctuations cancel the leading term in the Coulomb self-energy [26]

$$\Delta E = \Delta E_C + \Delta E_{\mathrm{pair}} = \frac{3\alpha}{4\pi} m_e c^2 \log \frac{\hbar}{m_e} c r_e. \tag{2.12}$$

The remaining dependence on the electron radius is only logarithmic, resulting in a $9\,\%$ increase of the electron mass at the Planck scale. The proportionality between the bare electron mass and its correction is the consequence of a symmetry between particles and antiparticles, called chiral symmetry. If this symmetry was exact, electrons would be massless. The fact that they do have a finite mass explicitly breaks the chiral symmetry.

2.3.2 Supersymmetric Principles

Just as in the positron analogon, doubling the degrees of freedom by introducing new particles, could solve many problems of the Standard Model. The proposed theory of Supersymmetry correlates bosons and fermions in supermultipletts. The SUSY generator Q transforms fermions into bosons and vice versa:

$$\begin{aligned} Q \,|\, \text{fermion}\rangle &= |\,\text{boson}\rangle, \\ Q \,|\, \text{boson}\rangle &= |\,\text{fermion}\rangle. \end{aligned}$$

The required operators, Q and its hermitian conjugate $Q^\dagger$, are anti-commuting spinors. Together with the momentum operator P^μ they satisfy the following commutation relations:

$$\begin{aligned} \{Q, Q^\dagger\} &= P^\mu \; ; \\ \{Q, Q\} &= \{Q^\dagger, Q^\dagger\} = 0 \; ; \\ [P^\mu, Q] &= [P^\mu, Q^\dagger] = 0 \; . \end{aligned}$$

Eigenstates which can be transformed into one another by the SUSY generators are called 'superpartners'. Since $(-P^2)$ and the gauge group generators commute with Q and $Q^\dagger$, superpartners have the same masses, gauge quantum numbers and couplings.

Introducing Supersymmetry could potentially solve all the problems mentioned in section 2.2. As shown in figure 2.3, within the minimal supersymmetric Standard Model (MSSM) the running couplings converge in one point at the GUT scale of 10^{16} GeV [17].

The quadratically divergent loop contribution to the Higgs boson mass by Standard Model particles, shown in figure 2.4, are automatically cancelled by a contribution from the corresponding superpartner, sketched in figure 2.5. Just as in the positron analogon (cf. section 2.3.1), the remaining Higgs boson mass contributions only scale logarithmically and the Higgs boson mass is naturally stabilised at the weak scale.
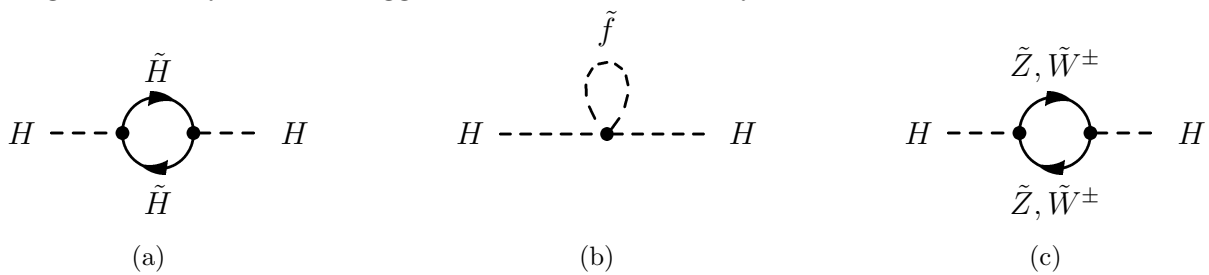
Figure 2.5: SUSY contributions to the Higgs boson mass. They cancel the quadratic divergences introduced by the graphs in figure 2.4.

SUSY extensions add up to 43 additional complex phases, which could contribute to the CP violation. This is an important condition to allow for the matter dominance in the universe.

Furthermore, supersymmetric transformations also include space-time transformations. Therefore, SUSY becomes automatically a theory of gravity, if it is treated as a local gauge symmetry.

Particle		Spin	Sparticle		Spin
Leptons	e, μ, τ	1/2	Sleptons	$\tilde{e}, \tilde{\mu}, \tilde{\tau}$	0
Neutrinos	ν_e, ν_μ, ν_τ	1/2	Sneutrinos	$\tilde{\nu}_e, \tilde{\nu}_\mu, \tilde{\nu}_\tau$	0
Quarks	$u, d, ...$	1/2	Squarks	$\tilde{u}, \tilde{d}, ...$	0
Photon	γ	1	Photino	$\tilde{\gamma}$	1/2
Z-boson	Z	1	Zino	$\tilde{Z}$	1/2
Higgs bosons	H, h, A	0	Higgsinos	$\tilde{H}_1, \tilde{H}_2$	1/2
W-bosons	$W^\pm$	1	Winos	$\tilde{W}^\pm$	1/2
Higgs bosons	$H^\pm$	1	Higgsinos	$\tilde{H}^\pm$	1/2
Gluons	g	1	Gluinos	$\tilde{g}$	1/2
Graviton	G	2	Gravitino	$\tilde{G}$	3/2

Neutralinos $\tilde{\chi}^0_{1,2,3,4}$ (for the Photino/Zino/Higgsinos rows); Charginos $\tilde{\chi}^\pm_{1,2}$ (for the Winos/Higgsinos rows).

Table 2.2: Particle - sparticle correspondence in the minimal supersymmetric Standard Model.

The naming convention for the SUSY scalar particles, the partners to the fermions, is to precede an 's' to the name of their Standard Model counterpart. The notation convention is to put a tilde above the symbol used for its Standard Model equivalent. For example, the partner of the tau τ is a stau $\tilde{\tau}$, the partner of the top t is called stop $\tilde{t}$. Continuing the analogies to the Standard Model language, SUSY particles are ordered into squarks and sleptons. The fermionic gauge boson partners are named with the suffix 'ino', e.g. the neutral fermionic partners of the gauge bosons are named wino $\tilde{W}^0$ and bino $\tilde{B}^0$.

2.3.3 Minimal Supersymmetric Model

Many different implementations of SUSY exist. This thesis will only consider the MSSM [27], i.e. models that introduce as few new particles as possible, while still providing a phenomenologically viable model.

In the MSSM, either only left- or only right-chiral superfields can be used to construct the Lagrangian. And since the hermitian conjugate of a left-chiral superfield is right-chiral and vice versa, the coupling to a hermitian conjugated Higgs superfield is forbidden. Thus, the MSSM requires at least two Higgs boson doublets [28] with different hypercharge. They create five Higgs boson mass eigenstates. Two neutral scalar Higgs bosons h^0 and H^0, one neutral pseudo-scalar Higgs boson A^0 and two charged scalar bosons H^+ and H^-.

The wino $\tilde{W}^0$ and the bino $\tilde{B}^0$, have the same quantum numbers as the neutral fermionic Higgs boson partners $\tilde{H}^0_{1,2}$. Together they mix to four neutralinos $\tilde{\chi}^0_{1,2,3,4}$. Accordingly, the charged higgsinos $\tilde{H}^-_d, \tilde{H}^+_u$ can mix with the charged winos $\tilde{W}^\pm$ to two charged mass eigenstates, the charginos $\tilde{\chi}^\pm_{1,2}$.

The relationship between Standard Model particles, SUSY partners and mass eigenstates is summarised in table 2.2.

A new quantum number called R-parity is introduced:

$$P_R = (-1)^{3(B-L)+2S}, \tag{2.13}$$

where S is the spin and L is the lepton number. It is a multiplicative quantum number, which is $P_R = +1$ for all Standard Model particles and the five Higgs bosons and $P_R = -1$ for all squarks, sleptons, gauginos and higgsinos.

If R-parity is conserved, this implies

- SUSY particles can only be produced in pairs;

- SUSY particles can only decay into odd numbers of lighter SUSY particles and their Standard Model partners;

- the lightest SUSY particle (LSP) has to be stable. If it does not carry electric charge, it can only interact weakly and thus is an excellent dark matter candidate.

R-parity conservation also ensures baryon number B conservation. If the baryon number is not conserved, protons would decay, e.g. $p \rightarrow e^+\pi^0$. Experiments like Super-Kamiokande have searched for this signature, but did not find any evidence for proton decays. Thus, they set a lower boundary on the proton partial lifetime of $\tau_p > 8.8 \cdot 10^{33}$ years [29]. In the following, only R-parity conserving MSSM scenarios are discussed.

2.3.4 Supersymmetry Breaking

If SUSY was exact, the Standard Model particles and their SUSY partners would have the same mass. Since no SUSY particles have been discovered up to now, SUSY particles must be much heavier than Standard Model particles. Thus, SUSY has to be a broken symmetry. To allow SUSY to solve the naturalness problem mentioned in section 2.2, the differences between particle and sparticle masses may not be larger than a few TeV. This implies that if SUSY exists and is a solution to the open questions of the Standard Model, it is experimentally accessible.

The so-called 'soft breaking' requires the effective Lagrangian to be the sum of an unbroken MSSM Lagrangian and an additional Lagrangian, containing the SUSY violating mass terms:

$$\mathcal{L} = \mathcal{L}_{\text{SUSY}} + \mathcal{L}_{\text{soft}} . \tag{2.14}$$

In this way, the unknown SUSY breaking mechanism can be parametrised by the introduction of soft terms. The drawback is the large amount of new free parameters. While an unbroken MSSM requires only one new parameter, the ratio of the vacuum expectation values of the two Higgs boson doublets, $\tan\beta = \frac{v_2}{v_1}$, a general breaking of the MSSM introduces 105 parameters [17].

To construct a model consistent with experimental observations, e.g. limits on flavour-changing neutral currents, it is assumed that SUSY breaking arises radiatively. The SUSY breaking sector is then referred to as 'hidden', the Standard Model part is called 'visible' and in-between some intermediate states act as 'messenger'. Just as in the Higgs mechanism, these messengers transport the SUSY breaking from the hidden to the visible sector through loop corrections. This can happen for example via gravitational interactions (mSugra), through the conformal anomaly (AMSB), or via gauge interactions (GMSB). While the historically favoured models are based on gravity-mediated SUSY breaking, this thesis is investigating a gauge-mediated SUSY breaking scenario.

2.3.5 Gauge-Mediated Supersymmetry Breaking Scenarios

Breaking the global Standard Model gauge symmetry creates a massless Goldstone boson. In analogy to this, breaking SUSY creates a massless neutral fermion, the goldstino. According to the Higgs mechanism, the goldstino is absorbed by the spin-3/2 partner of the graviton, called gravitino $\tilde{G}$.

The gravitino mass can be estimated as:

$$m_{\tilde{G}} = \frac{F}{\sqrt{3}\Lambda_{\text{Planck}}}. \tag{2.15}$$

With a SUSY breaking scale around $\sqrt{F} \simeq 10^{10} - 10^{11}\,\text{GeV}$ in gravity mediated SUSY breaking scenarios, the gravitino would be very heavy. On the other hand, in GMSB scenarios, the breaking occurs at an energy scale much smaller than the Planck scale: $\sqrt{F} \ll \Lambda_{\text{Planck}}$. Thus, in these scenarios the gravitino mass is small and the gravitino is always the LSP.

Since gravitinos couple very weakly, all SUSY decay chains end up with the next-to-lightest SUSY particle (NLSP), which is then decaying into a gravitino. Another feature of GMSB scenarios is that colliders can provide information on the fundamental SUSY breaking scale by measuring the NLSP properties [30].

GMSB models can be parametrised by six parameters:

- Λ is the effective visible sector SUSY breaking parameter, determining the universal SUSY particle mass scale. All sparticle masses scale linearly with Λ, which is of the order of $100\,\text{TeV}/\sqrt{N_5}$.

- N_5 is the number of messenger chiral $SU(5)$ supermultipletts that build the messenger sector. The gaugino masses scale linearly with N_5, while the scalar masses scale like $\sqrt{N_5}$. For low values the NLSP is a neutralino, for larger values its a right-handed slepton.

- M_{mess} is the messenger mass scale. Sparticle masses depend logarithmically on M_{mess}, the NLSP lifetime scales quadratically with M_{mess}. To avoid colour and charge breaking in the messenger sector requires $M_{\text{mess}} > \Lambda$.

- $\tan\beta$ is the ratio of the Higgs boson vacuum expectation values. It lies in the region $1 < \tan\beta < 60$. Lower values lead to a CP-even Higgs scalar lighter than the LEP exclusion limits, while larger ratios lead to a $\tilde{\tau}$ slepton that is significantly lighter than the lightest neutralino, which is chosen to be the LSP for the presented studies.

- $\text{sgn}(\mu)$ is the sign of the Higgs boson mass parameter. It appears in the gaugino mixing matrices.

- c_{grav} is the scale factor of the goldstino coupling. It can be used to control the NLSP lifetime, which scales with c_{grav}^2.

The underlying SUSY breaking order parameter F, which determines the goldstino couplings, is related to the GMSB model parameters via:

$$F = c_{\text{grav}} \cdot \Lambda \cdot M_{\text{mess}} . \tag{2.16}$$

The collider phenomenology of GMSB depends on the NLSP, which can either be the lightest right-handed slepton $\tilde{l}_R$, or the lightest neutralino $\tilde{\chi}_1^0$. For small values of $\tan\beta$ the selectrons $\tilde{e}$, smuons $\tilde{\mu}$ and staus $\tilde{\tau}$ degenerate. This region is also called co-NLSP region. With increasing values of $\tan\beta$, the mass difference between the two $\tilde{\tau}$ states increases, and the lightest slepton $\tilde{\tau}_1$ becomes the NLSP.

As $m_{\tilde{\chi}} \propto N_5$ and $m_{\tilde{\tau}} \propto \sqrt{N_5}$, large N_5 reduce $m_{\tilde{\tau}}/m_{\tilde{\chi}}$. On the other hand, renormalisation group evolution increases right-handed slepton masses relative to gaugino masses, therefore large values of M_{mess} increase $m_{\tilde{\tau}}/m_{\tilde{\chi}}$. Furthermore, as noted above, large $\tan\beta$ values decrease $m_{\tilde{\tau}}$ and thus reduce $m_{\tilde{\tau}}/m_{\tilde{\chi}}$.

This is illustrated in figure 2.6(a) which sketches the $\tilde{\tau}_1$ and $\tilde{\chi}_1^0$ NLSP regions in the $M_{\text{mess}} - N_5$ plane for various values of $\tan\beta$ between 3 and 30 [31]. The region above the labelled contours has a $\tilde{\tau}_1$ NLSP, while in the region below the NLSP is a $\tilde{\chi}_1^0$. The shaded grey region in the upper left corner, indicates the parameter space where gauge coupling constants become non-perturbative below the GUT scale under two-loop renormalisation group evolution. For $N_5 \geq 2$ the NLSP is a $\tilde{\tau}_1$ for almost the full parameter space, whereas for $N_5 = 1$ it is very likely to have a $\tilde{\chi}_1^0$ NLSP.

(a)   (b)
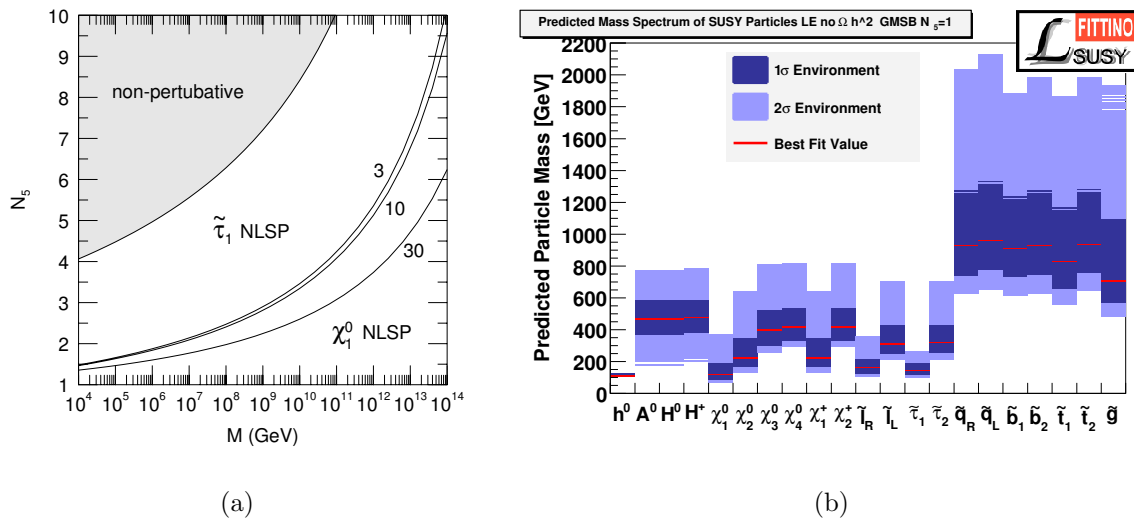
Figure 2.6: (a) The NLSP in the GMSB parameter space as a function of the messenger mass scale and the number of messenger multiplets [31]. (b) GMSB sparticle masses predicted by Fittino [32]. Plotted are the fit results for the most probable sparticle mass (red solid line), as well as the 1σ (dark blue area) and 2σ (light blue area) range.

The most probable sparticle mass spectrum can be predicted by Fittino [32], a program for determining MSSM parameters from collider observables using various advanced fitting techniques. Fittino derives MSSM parameters from available low-energy (LE) measurements, including observables from K- and B-meson decays, the anomalous magnetic moment of the muon $(g-2)_\mu$ and precision electroweak data from colliders. As GMSB models tend to give very small Gravitino masses, which correspond to warm or even hot dark matter, cosmological constraints from measurements of the cold dark matter density Ωh^2 are excluded.

The fit is performed for several values of $\text{sgn}(\mu)$ and N_5, leaving the continuous variables

$\tan\beta$, Λ, M_{mess} and c_{grav} as free parameters. The best fitting results with a $\chi^2/ndf = 19.3/21$ is obtained for $\text{sgn}(\mu) = +1$ and $N_5 = 1$. The fitted values for the continuous parameters in this scenario are

$$\Lambda = 87^{+32}_{-17}\,\text{TeV}, \quad M_{\text{mess}} = 430^{+1740}_{-350}\,\text{TeV}, \quad \tan\beta = 19.2^{+15.3}_{-6.7}, \quad c_{\text{grav}} = 411^{+10000}_{-411}.$$

While the large errors on M_{mess} and c_{grav} indicate that the fit cannot place any sensitive limits on them, Λ and $\tan\beta$ can be constrained.

Figure 2.6(b) shows the sparticle mass spectrum for the most probable parameter point with the fit result for the most probable sparticle mass. The lightest Higgs boson has a mass of $113.5 \pm 2\,\text{GeV}$, the NLSP is a neutralino with $150\,\text{GeV}$ as the most probable value for its mass, followed by the lightest stau with a mass around $200\,\text{GeV}$. The squarks are more than twice as heavy, and tend to be heavier than mSugra scenario predictions. If this sparticle spectrum is realised in nature, the Large Hadron Collider, a proton - proton machine with $7\,\text{TeV}$ per beam, that started data taking in November 2009, should be able to observe all the SUSY particles.

One special feature of GMSB models, which is not available in mSugra scenarios and thus might help to distinguish between them, is that the decay of the NLSP into the LSP does not have to be immediate. Depending on the NLSP mass, the decay length

$$c\tau = \frac{1}{k_\gamma} \cdot \left(\frac{100\,\text{GeV}}{m_{\text{NLSP}}}\right)^5 \cdot \left(\frac{\sqrt{F}}{100\,\text{TeV}}\right)^4 \cdot 10^{-2}\,\text{cm}, \tag{2.17}$$

ranges from few $10^{-5}\,\text{cm}$ to several $10^4\,\text{cm}$. It depends on $k_\gamma \equiv |N_{11}\cos\theta_W + N_{12}\sin\theta_W|$, with the neutralino mixing angles N_{ij} and scales with F^2. Therefore, measuring the NLSP lifetime provides a direct (and unique) access to the SUSY breaking scale in the hidden sector.

The expected detector signature for a neutralino NLSP, on which this thesis is focusing, are photons from the two $\tilde{\chi}_1^0 \to \tilde{G}\gamma$ decays and missing transverse momentum carried away by the gravitinos. For intermediate neutralino lifetimes, one expects displaced vertices. If the lifetime is large, the neutralino might decay outside the detector system and escape undetected. In this case, it will be hard to distinguish the signature from mSugra models, where the neutralino is the LSP and also escapes undetected.

2.3.6 Search Status

The most constraining limits on searches for new phenomena at high energies result from earlier collider experiments at LEP and Tevatron. Each of the four experiments at LEP has collected approximately $1\,\text{fb}^{-1}$ of data from 1989 to 2000. None of them found any evidence for neutralino decays [33, 34, 35, 36]. The Tevatron at Fermilab is still running. Until the end of 2008, $5\,\text{fb}^{-1}$ have been recorded. The data set is expected to gain another $1.5\,\text{fb}^{-1}$ with each year of operation. Experiment wise [37, 38, 39] and combined analyses [40] did not find any hints for new physics.

One example for a search for GMSB signatures with photon final states, is an analysis of the CDF collaboration [38]. They search for neutralino decays with low lifetime into photons and gravitinos in the two photons plus missing transverse energy $\not{E}_t$ channel. They select events with two isolated photons in the central detector region

$(\Delta\Phi < \pi - 0.15)$ with $E_t \geq 13\,\mathrm{GeV}$ each. Since the largest background is expected from QCD events with fake $\not{E}_t$, the missing transverse energy significance is estimated from performing pseudo-experiments that generate $\not{E}_t$. This allows to determine the expected $\not{E}_t$ distribution for mis-measured background events. The significance is a measure for the probability that the measured $\not{E}_t$ distribution is larger than the one expected from background events. CDF selects events with significance larger than 3. Furthermore, the transverse energy sum of all identified objects in the event has to be $H_t \geq 200\,\mathrm{GeV}$.

After all selections CDF observes 1 candidate event, which is consistent with the expectation of 0.62 ± 0.29 background events in $2\,\mathrm{fb}^{-1}$ data. Thus, they set cross section and mass limits, sketched in figure 2.7(a). Plotted are the $95\,\%$ confidence level exclusion limits in the neutralino mass, neutralino lifetime plane from CDF and from ALEPH measurements, as well as the cosmologically favoured region. For $\tilde{\chi}_1^0$ lifetimes below $2\,\mathrm{ns}$, masses below $140\,\mathrm{GeV}$ are excluded.

(a)   (b)
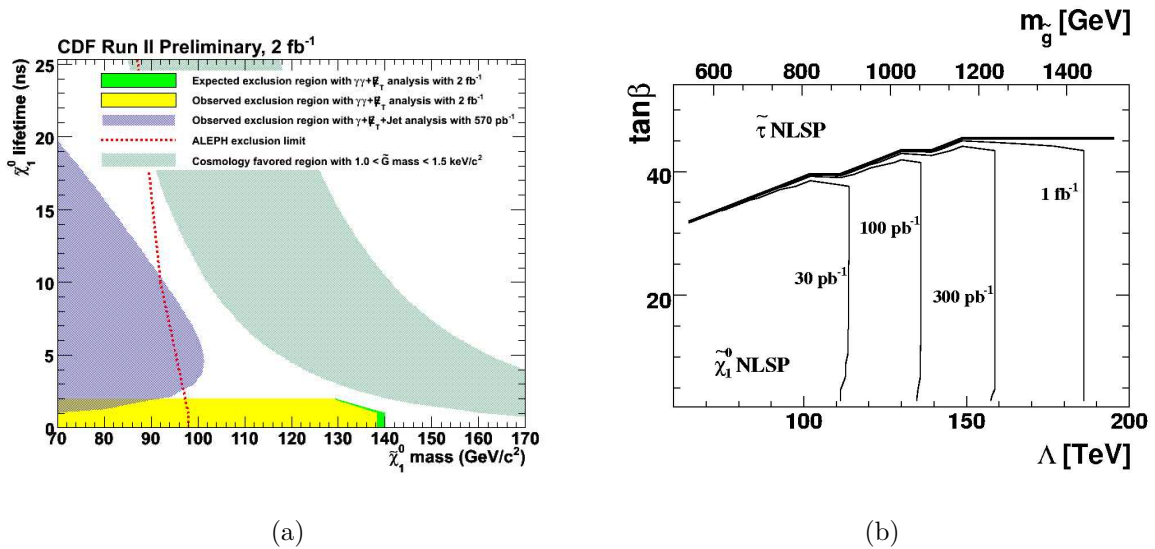
Figure 2.7: (a) GMSB domain excluded by Tevatron searches in the neutralino NLSP mass and lifetime plane [38]. (b) Predicted LHC discovery potential of neutralino NLSP in the di-photon channel [41].

This thesis is investigating neutralinos with $m_{\tilde{\chi}_1^0} = 151\,\mathrm{GeV}$ at lifetimes between $0.2\,\mathrm{ns}$ and $11\,\mathrm{ns}$. This region has not been excluded by any measurements so far, and falls into the cosmologically favoured region indicated in figure 2.7(a).

Based on the experience from Tevatron, the two multi-purpose experiments CMS and ATLAS, running at the LHC, have developed search strategies for GMSB searches [42]. Already with a fairly small amount of $1\,\mathrm{fb}^{-1}$ of data ATLAS is capable to select $511 \pm 20^{+33}_{-58}$ signal events[1] with a negligible amount of $2 \pm 2^{+0}_{-0}$ background events [41]. Since the background is vanishing, the discovery potential, plotted in figure 2.7(b), is described as contour lines with ten signal events for different integrated luminosities in the Λ-$\tan\beta$ plane, while all other parameters are kept constant. A discovery, possible in the region below and left of the contour lines, is possible in a large parameter space already with a small amount of data.

---

[1]for a GMSB scenario with $\Lambda = 90\,\mathrm{TeV}$, $N_5 = 1$, $M_{\mathrm{mess}} = 500\,\mathrm{TeV}$, $\tan\beta = 5$, $\mathrm{sgn}(\mu) = +$, $c_{\mathrm{grav}} = 1$

SUSY models are also of interest for cosmology, since they provide good dark matter candidates. These dark matter candidates can be classified according to their velocity dispersion, which defines their free-streaming length. Most cosmological models favour cold dark matter, which is heavy and slow. These models have a bottom-up hierarchy, in which single stars cluster to galaxies.

GMSB models predict cold gravitino dark matter to occur for $10\,\mathrm{keV} \lesssim m_{\tilde{G}} \lesssim 10\,\mathrm{MeV}$ and a messenger scale $100\,\mathrm{GeV} \lesssim M_{\mathrm{mess}} \lesssim 1\,\mathrm{TeV}$ [43]. Scenarios with smaller gravitino masses and higher messenger mass scale are cosmologically acceptable, but yield warm or hot gravitino dark matter.

Hot dark matter, which is light and fast, has a free-streaming length that is so long that it smooths out fluctuations in the total matter density. Therefore, the structure formation of the universe can only be realised in a top-down hierarchy, i.e. galaxies form through fragmentation of super-clusters of galaxies. Since these models require a much more inhomogeneous galaxy distribution than the one observed, they were abandoned by the mid-1980s [44].

Although this thesis focuses on a GMSB scenario with a mass of $m_{\tilde{G}} = 1.5 \cdot 10^{-7}\,\mathrm{GeV}$, and hence offers a hot dark matter candidate, GMSB models with a light gravitino NLSP can not be generally excluded by cosmological observations. For instance, the limits on the GMSB parameter space depend strongly on cosmological assumptions, such as the details of inflation and leptogenesis [45, 46]. Furthermore, the collider phenomenology does not change significantly for a Gravitino with a mass of a few keV.

3 ILC and ILD

As shown in the last chapter, new physics is expected to show up around the TeV scale. Currently this region is tested by the LHC with a centre-of-mass energy up to $14\,\mathrm{TeV}$. The LHC is expected to reveal whatever lies beyond the known borders. Nevertheless, as a hadron collider it suffers from large backgrounds and, since hadrons are composite states, undetermined initial states.

Once the hadron machine discovers new physics signatures, it is necessary to perform complementing precision measurements at the TeV scale, to determine what kind of new physics appeared. This can be fulfilled by a lepton collider, which offers a cleaner environment and well-defined initial states.

The International Linear Collider (ILC), a proposed electron - positron collider with a centre-of-mass energy up to $\sqrt{s} = 500\,\mathrm{GeV}$ in its first phase, is able to deliver the required precision data.

In order to perform precision measurements a detector with high resolution is indispensable. The International Large Detector (ILD) is designed as a multi purpose detector for the ILC, with the paradigm of particle flow in mind.

Both projects, ILC and ILD are still in their design phase. This thesis describes part of the R&D towards a detector design. The detector optimisation is not only considering physics requirements in full detector simulation, as discussed in chapter 5, but also the construction of large scale prototypes for the evaluation of new detector technologies using test-beams, as described in chapter 6, to exploit the technologies.

This chapter will give a short overview of machine and detector design. The description follows the electrons from the source through the accelerator and the detector system.

3.1 The International Linear Collider

The ILC has a tunable centre-of-mass energy ranging from $200\,\mathrm{GeV}$ to $500\,\mathrm{GeV}$. In addition, it can run at the Z-pole ($91\,\mathrm{GeV}$) and has the option to be upgraded to $1\,\mathrm{TeV}$. The accelerator is based on superconducting radio frequency (RF) cavities with an accelerating gradient of $31.5\,\mathrm{MV/m}$. The anticipated luminosity of $\mathcal{L} = 2{\cdot}10^{34}\,\mathrm{cm}^{-2}\mathrm{s}^{-1}$ is expected to yield an integrated luminosity of $\int \mathcal{L}\,dt = 500\,\mathrm{fb}^{-1}$ in the first four years of operation.

Polarised beams with an energy stability and precision better than $0.1\,\%$ allow for a rich high precision physics programme. This programme comprises top-quark physics and Higgs boson measurements, as well as anything that might exist beyond the Standard Model, e. g. Supersymmetry.

19
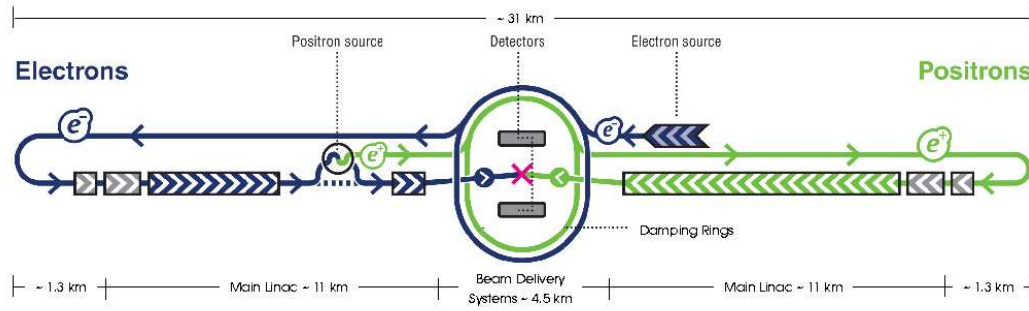
Figure 3.1: A schematic layout of the International Linear Collider.

3.1.1 Machine Layout

A Reference Design Report [47], from which all machine design parameters have been taken, has been released in 2007. A Technical Design Report is anticipated for 2012. Since this project is still under development, details and dates may be subject to future changes.

The main machine components, as sketched in figure 3.1, are

- a source for polarised electrons;

- an undulator-based positron source, driven by the partially accelerated main electron beam;

- damping rings with a circumference of 6.7 km, housed in a common tunnel at the centre of the ILC;

- beam transport from the damping rings to the linear accelerators followed by a bunch-compressor system;

- two 11.3 km long main linear accelerators with a beam pulse length of 1.6 ms and a repetition rate of 5 Hz;

- a two times 2.25 km long beam delivery system to each side of the interaction point, which enables collision at a 14 mrad crossing angle.

The only interaction region is shared by two detectors. The detectors will consecutively be pushed into and pulled out of the interaction region to take data. The non-operating detector can be maintained, repaired or upgraded in the meantime.

3.1.2 Particle Source

The electron beam is produced by a laser illuminated photocathode in a direct current (DC) gun.

The positron source is based on a 150 m long superconducting helical undulator, driven by the partially accelerated (150 GeV) electron beam. An undulator is a periodic structure of dipole magnets, which forces the traversing electrons to emit synchrotron

radiation. In contrast to conventional undulators, a helical one is producing two times more synchrotron radiation power per period and delivers circularly polarised photons. Although positron polarisation is not in the ILC baseline design, but only a possible design option, photons produced from a helical undulator that are directed on a rotating $0.4\,X_0$ titanium target, automatically produce longitudinally polarised electron and positron pairs. The electrons and remaining photons are dumped, while the positrons are fed into the accelerator.

The electron source allows for a polarisation of more than $|\mathcal{P}_{e^-}| \geq 80\,\%$, which is also given in the baseline accelerator design. It is likely to yield $|\mathcal{P}_{e^+}| \geq 60\,\%$ positron polarisation without any loss of luminosity [48], if the helical undulator positron source is realised.

Both beams are pre-accelerated to $5\,\mathrm{GeV}$ before being passed on to the damping rings.

3.1.3 Damping Ring

The damping rings have a circumference of $6.7\,\mathrm{km}$, and are located in a common tunnel around the centre of the ILC. Their purpose is to reduce the beam emittance, which is a measure for the occupied phase space. In beams with low emittance particles are confined to a small distance and have a small momentum spread. The nominal design values for the ILC are a horizontal emittance of $10\,\mathrm{mm}\cdot\mathrm{mrad}$, and a vertical emittance of $0.04\,\mathrm{mm}\cdot\mathrm{mrad}$ at the interaction point. In addition the damping rings are used as delay lines to compensate for pulse-to-pulse variations in parameters such as the bunch charge. The damping lasts $25\,\mathrm{ms}$, while a bunch-train is $1\,\mathrm{ms}$ long, therefore the ring has to be able to contain a full bunch train of 2625 bunches with $2 \cdot 10^{10}$ particles per bunch.

On the way from the damping rings to the main accelerator, the beam is further collimated and the bunches are compressed by a factor of 30 to 45 to provide very short bunches ($0.3\,\mathrm{mm}$) to the main linear accelerator, and thus also to the interaction point. Furthermore, the beam is accelerated from 5 to $15\,\mathrm{GeV}$, and the vertical beam polarisation can be rotated to any arbitrary angle.

3.1.4 Main Accelerator

The main linear accelerators (linacs) accelerate the beams from 15 up to $250\,\mathrm{GeV}$ each. During acceleration, the low beam emittance and the small beam energy spread have to be preserved, and no transverse or longitudinal jitter must be introduced.

The acceleration is achieved with superconducting niobium cavities. They are operated at the temperature of super-fluid helium ($2\,\mathrm{K}$), with a frequency of $1.3\,\mathrm{GHz}$. The repetition rate is $5\,\mathrm{Hz}$ for a pulse length of roughly $1\,\mathrm{ms}$.

The accelerator tunnel is accompanied by a service tunnel, which is e.g. housing the RF sources and power supplies. Both tunnels are situated underground, connected to the surface by vertical shafts.

The beams are then focused towards the interaction point with a crossing angle of $14\,\mathrm{mrad}$, which is shared by two multi-purpose detectors.

To achieve the intended luminosity, the focused bunches have to be very small. This implies a high space charge, and thus the bunches are accompanied by high electric

Beam Parameter	Value at IP	[unit]
Bunch population	2	$\times 10^{10}$
N_{bunches} per train	2625	
Repetition rate	5	Hz
Bunch interval	369	ns
RMS bunch length	300	μm
Normalised horizontal emittance	10	mm $\cdot$ mrad
Normalised vertical emittance	0.04	mm $\cdot$ mrad
RMS horizontal beam size	640	nm
RMS vertical beam size	5.7	nm

Table 3.1: Nominal ILC beam parameters at the interaction point [47].

fields. The fields are strong enough to exert a force on the approaching bunch of opposite charge. As a result the bunches attract each other and individual particles are focused even more towards the centre of the opposite bunch. On one hand this is beneficial, since the luminosity increases by a factor of about two, on the other hand the accelerated particles radiate photons. This effect, known as beamstrahlung, deteriorates the beam energy spectrum and leads to a considerable amount of machine-background in the detectors [49].

The nominal beam parameters at the interaction point (IP) are summarised in table 3.1.

3.2 The Physics Programme

The physics programme of a lepton collider in the TeV range is rich. One of the main interests lies in the investigation of the Higgs sector. But even in the absence of a Higgs boson, there are many topics the ILC can contribute to.

Being the heaviest constituent of the Standard Model, the top-quark is of special interest. It is the particle coupling most strongly to electroweak symmetry breaking and many predictions of new physics depend on the top-quark mass. As of today it is only known with an uncertainty of $\Delta m_t = 1.3\,\text{GeV}$ [50]. At the ILC, the top-quark mass can be measured with an uncertainty of $\Delta m_t = 30\,\text{MeV}$ [51].

Despite the Standard Model's numerous successes in explaining present data, without experimental observation of the Higgs boson, it is incomplete. If it exists, the discovery will most likely happen during the next couple of years at the LHC [52, 53]. A precise determination of the Higgs properties can only be provided by the ILC. As shown in figure 3.2(a), the dominant Higgs production channels are WW fusion $e^+e^- \to \bar{\nu}_e \nu_e \text{H}$ and Higgs-strahlung $e^+e^- \to \text{Z H}$. The decay branching ratios plotted in figure 3.2(b) reveal that a light Higgs decays dominantly into $b\bar{b}$, while a Higgs with $m_H > 140\,\text{GeV}$ mostly decays into $\text{WW}^{(*)}$ and $\text{ZZ}^{(*)}$ pairs, where one of the bosons is virtual for Higgs masses below threshold [54].

With $\int \mathcal{L}\,dt = 500\,\text{fb}^{-1}$ and a $m_H = 120\,\text{GeV}$ Higgs boson, the Higgs boson mass can be measured with a precision of $\Delta m_H \sim 80\,\text{MeV}$ [55]. Measuring the cross section
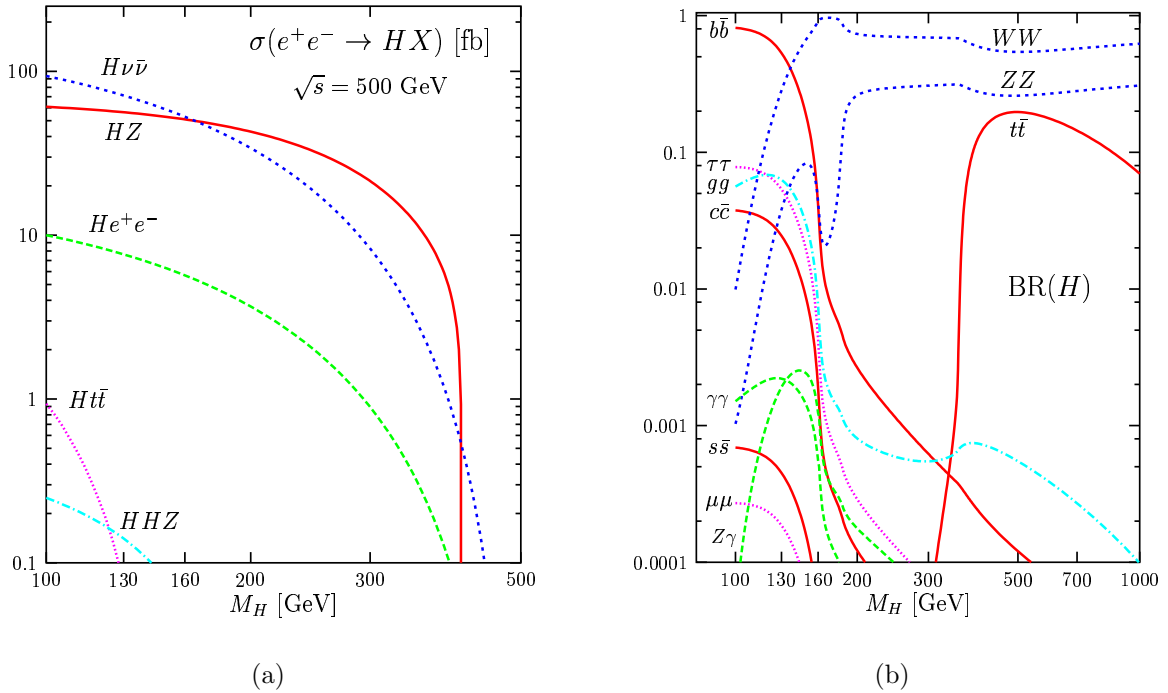
Figure 3.2: The Standard Model Higgs boson (a) production cross section and (b) decay branching ratios as a function of the Higgs boson mass [54].

rise at the ZH threshold allows the determination of the spin and parity. Furthermore, it can be used to verify that the Higgs boson couplings to W-/Z-bosons are proportional to the boson masses. The same can be done for heavy fermions, by precisely measuring the Higgs boson branching ratios. Another very important feature of the Higgs-mechanism is the Higgs boson self-coupling capability. The precision test of equation 2.10 will reveal whether the new particle is a Standard Model Higgs, or maybe part of a supersymmetric world.

If supersymmetric particles are produced at the ILC, their properties can be determined with large precision, e.g.

- measure their masses, mixings, decay widths, production cross sections, decay branching ratios, . . . ;

- determine their spins, parities, gauge quantum numbers and couplings to verify they are really super partners of Standard Model particles;

- reconstruct the low-energy soft SUSY breaking parameters in a way that is as model-independent as possible.

Furthermore, the precise knowledge of the properties of the lightest SUSY particle is required to resolve whether it accounts for dark matter (DM).

Cosmological data from the WMAP satellite determine the dark matter mass density in the universe to be [20]

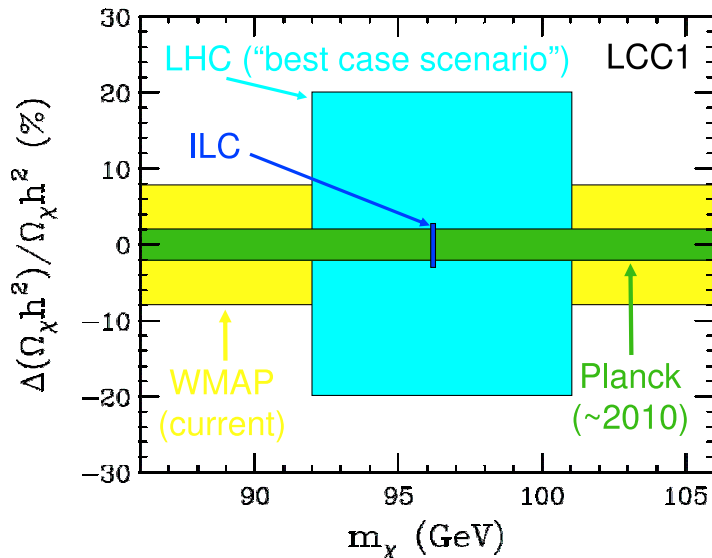$$\Omega_{\mathrm{DM}}h^2 = 0.111 \pm 0.006, \tag{3.1}$$

Figure 3.3: Accuracy of the dark matter density and mass measurement from WMAP
in the LCC1 scenario, and expected performance from Planck, LHC and
ILC [56].

where $\Omega_{\mathrm{DM}} \equiv \rho_{\mathrm{DM}}/\rho_{\mathrm{crit}}$ is the ratio between the dark matter density ρ_{DM} and the
critical mass density ρ_{crit}. This implies the overall energy-mass density of the Universe
is $\Omega_{\mathrm{tot}} = 1$, corresponding to a flat Universe. The accuracy of currently $6\,\%$ is expected
to improve to the percent level by future measurements from the Planck satellite [57].

As shown in figure 3.3 for an mSugra scenario (cf. section 2.3.4), the ILC is expected
to deliver an accuracy compatible with Planck. Furthermore, ILC measurements can
constrain the dark matter particle mass, which the satellite experiments cannot. Con-
sistency of the ILC and WMAP/Planck measurements would provide evidence that the
lightest supersymmetric particles are stable and possibly form all of the non-baryonic
dark matter.

3.3 Detector Design for ILC

In contrast to detectors at hadron machines, at ILC the data rates are much smaller,
and radiation damage plays a less significant role. However, to fully exploit the physics
potentials of the ILC a very high precision has to be achieved.

At the time this thesis is written two major detector concepts are being developed:
the silicon tracking technology based Silicon Detector (SiD) [58], and the International
Large Detector (ILD) [51] which is described in some more detail later on. They are
based on the particle flow concept described in section 3.3.1. Tracking and calorime-
try are combined to achieve the best overall reconstruction, including single particle
reconstruction within hadronic jets.

3.3.1 Particle Flow

At energies below approximately $100\,\mathrm{GeV}$, the accuracy of momentum reconstruction
of charged particles in the tracking system exceeds anything that could be achieved

with calorimeters. This is illustrated in figure 3.4(a), which shows the expected resolution of the ILD sub detectors as a function of particle energy. The energy resolution of the hadron calorimeter (HCAL) scales with $\sigma_E/E = 49.2\,\%/\sqrt{E}$, the electromagnetic calorimeter (ECAL) has a resolution of $\sigma_E/E = 16.6\,\%/\sqrt{E}$. The anticipated momentum resolution of the time projection chamber (TPC), is $\delta_p/p \sim 9 \cdot 10^{-5}$, and the full tracking system can reach $\delta_p/p \sim 2 \cdot 10^{-5}$ [51].

The idea of particle flow is to utilise this fact, by fully reconstructing every particle with the best suited sub-detector system. Ideally, the momentum of every single charged particle is fully determined in the tracker, while the energy of photons and neutral hadrons are obtained from the calorimeter. The jet energy is then given as the sum of the energies of the individual particles. The crucial step is to correctly assign the calorimeter hits to the reconstructed tracks, which requires an efficient separation of nearby showers. Thus, the performance of particle flow is determined by both pure detector resolution and reconstruction algorithms.

In average a jet is a composition of charged particles, photons, and neutral hadrons. The best overall reconstruction is achieved by combining charged particles measured in the tracking system, with photons determined in the electromagnetic calorimeter, and neutral hadrons as detected in the combination of electromagnetic and hadron calorimeter. If particle flow worked perfectly, the jet resolution σ_{jet} would be the quadratic sum of the single particle resolution weighted with their respective energy fraction f:

$$\sigma_{\mathrm{jet}} = f_{\mathrm{ch}} \cdot \sigma_{\mathrm{ch}} \oplus f_\gamma \cdot \sigma_\gamma \oplus f_{\mathrm{h}^0} \cdot \sigma_{\mathrm{h}^0} \tag{3.2}$$

σ_{ch} accounts for the (almost negligible) tracker resolution, σ_γ represents the ECAL, and σ_{h^0} the HCAL resolution, which is usually the worst. On average $f_{\mathrm{ch}} \sim 0.6$, $f_\gamma \sim 0.3$ and $f_{\mathrm{h}^0} \sim 0.1$, but event-by-event fluctuations are large.

(a)   (b)
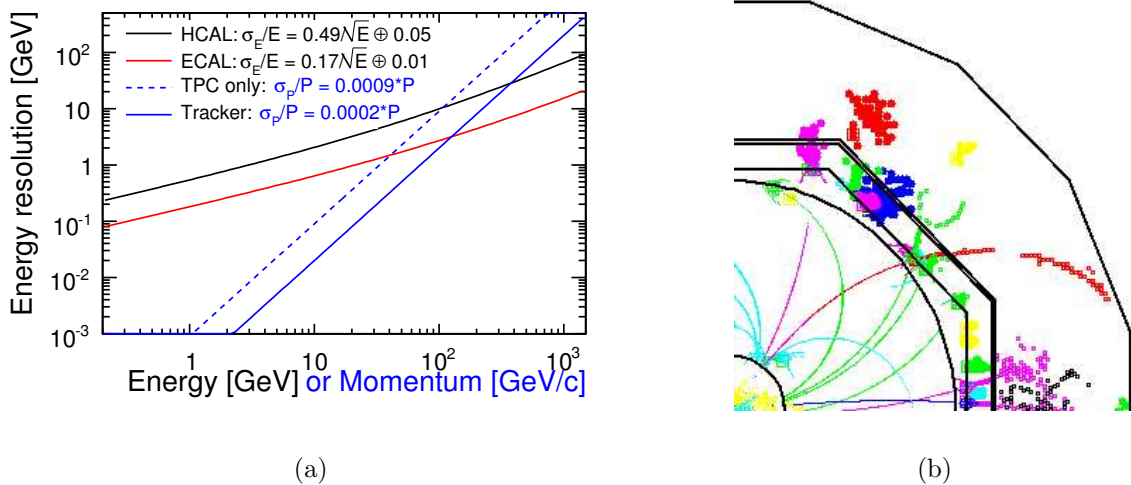
Figure 3.4: (a) Expected energy and momentum resolution of the ILD sub-detector systems. (b) Event display of a $100\,\mathrm{GeV}$ jet reconstructed with a particle flow algorithm [59]. Different colours correspond to different particles identified within a jet.

In the particle flow reconstruction, particle separation becomes more important than single particle resolution. As a consequence, the calorimetric system has to provide an

unprecedented transverse and lateral granularity, while the energy resolution require-
ments are rather modest. Nevertheless, overlapping showers cannot be avoided. The
two main problems of particle flow are 'missing energy' and 'double counting'.

Accidentally assigning a neutral shower to a close-by shower induced from a charged
particle, leads to 'missing energy'. Only the energy measured in the tracking system will
be taken into account, whereas the energy of the neutral shower will not be measured
at all. The measured energy would be smaller than the true energy. On the other hand,
accidentally splitting a shower from a charged particle will produce 'double counting'.
A second neutral particle that does not really exist would be reconstructed, and the
measured energy would be larger than the true energy.

Both effects can be summarised in a 'confusion' term σ_{conf}, that worsens the jet energy
resolution:

$$\sigma_{\mathrm{jet}} = f_{\mathrm{ch}} \cdot \sigma_{\mathrm{ch}} \oplus f_{\gamma} \cdot \sigma_{\gamma} \oplus f_{\mathrm{h}^0} \cdot \sigma_{\mathrm{h}^0} \oplus \sigma_{\mathrm{conf}}. \tag{3.3}$$

The power of particle flow algorithms is illustrated in figure 3.4(b). The event display
shows the signature of a $100\,\mathrm{GeV}$ jet from a $Z \to u\bar{u}$ decay at $\sqrt{s} = 200\,\mathrm{GeV}$ in
one quadrant of an ILD-like detector. The different colours correspond to different
particles identified within this jet. Due to the high granularity, even close-by showers
from neutral and charged particles can be separated.

3.3.2 Requirements

The main ILC detector requirements, which are all substantially higher than those on
current detectors are [60]:

Vertexing   The aspired impact parameter resolution of

$$\delta(\mathrm{IP}_{r\Phi,z}) \leq 5\,\mu\mathrm{m} \oplus \frac{10\,\mu\mathrm{m}\,\mathrm{GeV}/c}{p\sin^{3/2}\theta}, \tag{3.4}$$

where p is the momentum of the particle and θ is the polar angle of the track, has to
be twice as good as the currently best resolution from SLD [61]. This could be realised
with a multi-layer silicon based pixel detector, where the innermost layer is as close as
possible to the beam pipe. In addition, a high magnetic field confines the background
generated in colliding bunches.

Standard Model processes such as $t\bar{t} \to bW^+\bar{b}W^-$ provide challenging requirements on
b- and c-quark tagging. Furthermore, in case the Higgs boson mass is $m_H \leq 140\,\mathrm{GeV}$,
distinguishing between $b\bar{b}$, $c\bar{c}$, gg and $\tau^+\tau^-$ pairs represents a major challenge for the
vertexing system.

Track Momentum Resolution   The design goal for the momentum resolution of

$$\delta\left(\frac{1}{p_t}\right) \leq 5 \cdot 10^{-5}\,(\mathrm{GeV}/c)^{-1}, \tag{3.5}$$

is of special interest for the analysis of the di-lepton mass in the $HZ \to Xl^+l^-$ channel,
where X can be any decay product of the Higgs boson. It has to be a factor of 10
better than what was reached at LEP [62], and can be achieved by a large tracking
volume and a high magnetic field.

Energy Resolution   The key to the ILC detector design is jet energy resolution. A jet is a bunch of collimated particles, originating from a quark or a gluon. The energy of this jet corresponds to that of the originating particle, and the better the jet-energy resolution, the more precise the energy of this original particle can be determined.

Many physics processes result in multi-jet final states, often accompanied by charged leptons or missing energy. The reconstruction of the invariant mass of several jets is essential to distinguish between W, Z and Higgs bosons, and thus, allows the discovery of new states or decay modes. Ideally, the di-jet mass resolution should be comparable to the natural decay width of the primary particle, which is around a few GeV. Since a jet energy resolution of $\sigma_E/E = a/\sqrt{E\,[\mathrm{GeV}]}$ leads to a di-jet mass resolution of roughly $\sigma_m/m = a/\sqrt{E_{jj}\,[\mathrm{GeV}]}$, where E_{jj} is the energy of the di-jet system, this translates to a jet energy resolution of

$$\left(\frac{\sigma}{E}\right)_{\mathrm{jet}} \leq 4\,\% \tag{3.6}$$

for 50 to 250 GeV jets, which is about a factor of two better than what was achieved at LEP.

Hermeticity   Many physics scenarios beyond the Standard Model predict missing energy signatures. Therefore, hermeticity and particle detection capabilities at small angles are required. This implies to have good coverage of and measurement capability in the forward direction, which is also essential to allow a precision determination of the luminosity spectrum.

3.3.3 The International Large Detector Concept

The ILD detector design is summarised in an letter of intent [51]. Like many high energy physics multi-purpose detectors, it has an onion-like structure. Following the particle flow philosophy described in section 3.3.1, the highly granular calorimeter system, surrounding a Time Projection Chamber as central tracker, is placed within the superconducting coil.

To enable a 'push-pull' scenario, in which two detectors share one interaction region, the complete ILD detector is mounted on a movable platform. This ensures the integrity and calibration of the detector is least disturbed during movement.

Precision physics require exact knowledge of the beam conditions. The beam energy and polarisation are measured in small dedicated experiments shared by the two detectors in the interaction region. The luminosity is determined in the very forward calorimeters.

Figure 3.5 shows a schematic view of the ILD detector as determined in the ILD letter of intent [51]. The vertex detector is visible on the bottom of the quadrant view. It is surrounded by the main tracker cylinder, which in turn is surrounded by an electromagnetic calorimeter and an hadron calorimeter. They are placed inside the coil cylinder, which is enclosed by an instrumented return yoke. The main geometrical parameters, as well as the main design resolutions, are listed in table 3.2. A more detailed description of the detector sub-components is given in the following.
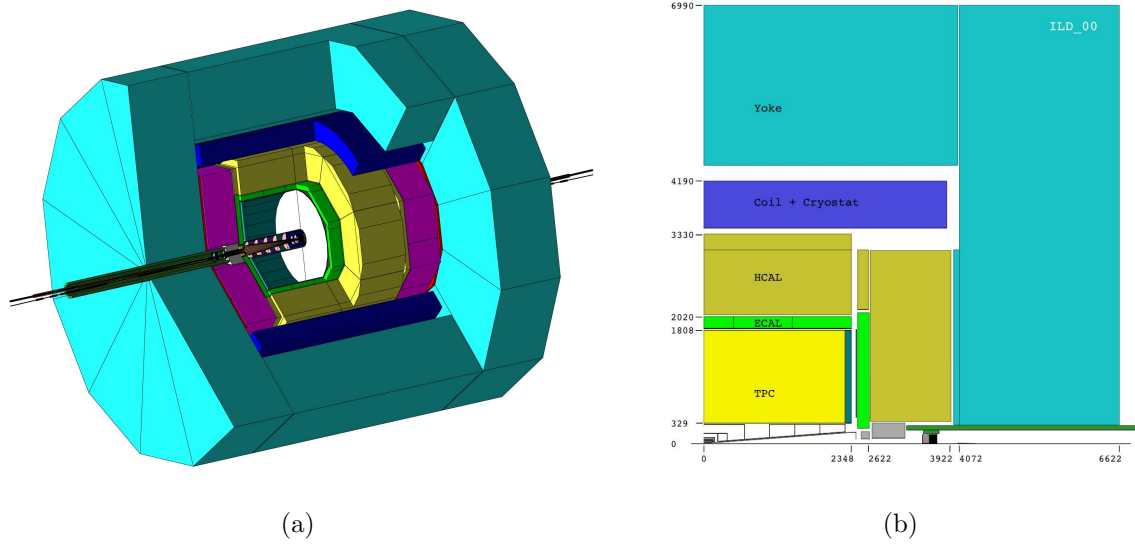
Figure 3.5: (a) 3-dimensional view of the ILD detector concept and (b) schematic view of one ILD detector quadrant [51].

Sub-detector	Geometrical Parameters		Resolution Goal
VTD	Layers	3 doublets	impact parameter resolution:
(one option)	$R_{\min}$	1.6 cm	$\delta(\mathrm{IP}_{r\Phi,z}) \leq 5\,\mu\mathrm{m} \oplus \frac{10\,\mu\mathrm{m}\,\mathrm{GeV}/c}{p\sin^{3/2}\Theta}$
	$R_{\min}$	39.5 cm	momentum resolution:
TPC	$R_{\max}$	173.9 cm	$\delta\left(\frac{1}{p_t}\right)_{\text{TPC only}} \leq 9 \cdot 10^{-5}\,(\mathrm{GeV}/c)^{-1}$
	$z_{\max}$	224.8 cm	$\delta\left(\frac{1}{p_t}\right)_{\text{full Tracking}} \leq 2 \cdot 10^{-5}\,(\mathrm{GeV}/c)^{-1}$
	$R_{\min}$	184.7 cm	energy resolution:
ECAL	Layers	20 + 9	$(\sigma/E)_{\mathrm{ECAL}} = \frac{10\,\%}{\sqrt{E}} \oplus 1\,\%$
	depth	23.6 X_0	
	$R_{\max}$	333.0 cm	energy resolution:
HCAL	Layers	48	$(\sigma/E)_{\mathrm{HCAL}} = \frac{50\,\%}{\sqrt{E}} \oplus 4\,\%$
	depth (ECAL + HCAL)	6.86 λ_i	$(\sigma/E)_{\mathrm{jet}} = 3 - 4\,\%$

Table 3.2: Geometrical parameters and design resolutions of the ILD detector [51].

Tracking System

The tracking system has to enable the reconstruction of charged particle momenta and energies with high precision and high efficiency. ILD has a large gaseous main tracker, complemented by silicon tracking, embedded in a 3.5 T solenoidal magnetic field. Each of the tracker subsystems is capable of stand-alone tracking, and designed to minimise the amount of material in front of the calorimeters.

Vertex Detector (VTX)   The vertex detector has to provide the required flavour tagging capabilities. It is also important for track reconstruction, especially for low momentum particles that do not reach the main tracker due to the high magnetic field. Furthermore, it provides time-stamping information for bunch separation. To fulfil the requirements stated in equation 3.5, the single point accuracy should be better than approximately $3\,\mu$m. Two alternative geometries are under consideration. One is built of three cylindrical super-layers, each comprising two layers of thin pixel sensors. The second option comprises five equidistant single layers. In both cases, the innermost layer has a radius of $16\,$mm, the outermost one is $60\,$mm away from the interaction point. The final technology choice still has to be taken.

The complete VTX system, including support, cryostat and cage may not add up to more than $0.74\,\%\,X_0$. It has to be radiation hard enough to handle the beam background dose of annually $1\,$kGy by electromagnetic particles and $10^{11}\,\mathrm{n}_{eq}/\mathrm{cm}^2$ by neutrons. The high occupancy, especially in the innermost layer, poses a very demanding requirement on the read-out technology choice. Two alternative approaches are currently under investigation. One with continuous read-out of the sensors, and one where the signal is stored during the whole train and read out during the beam-less period between two consecutive trains.

Silicon Tracking   A silicon tracking system extends the tracking capabilities and ensures low-angle coverage. It can be utilised to monitor field distortions in the Time Projection Chamber, and contribute to alignment and time stamping.

- The Silicon Internal Tracker (SIT) is located between the VTX and the TPC in the barrel. Thus, it enhances the linking efficiency of tracks between them. Furthermore, it improves the reconstruction of long-lived stable charged particles. It is built up from double-sided strip detectors.

- The Silicon External Tracker (SET) is also positioned in the barrel. It provides an entry point to the ECAL outside the outer TPC barrel. Just as the SIT it consists of double-sided silicon strips. Together SIT and SET provide three precision space points, which improve the momentum resolution and provide time-stamping information for bunch separation.

- The Forward Tracking Detector (FTD) covers the very forward region down to $0.15\,$rad. Seven disks on each side of the VTX are foreseen. The first three disks are equipped with silicon pixel detectors, while the latter four are read out by silicon micro-strips.

- The Endcap Tracking Detector (ETD) is located between the TPC end cap, and the ECAL end cap. This single-sided silicon micro-strips detector improves the matching efficiency between tracks and showers in the ECAL. Together with the FTD it ensures full tracking hermeticity.

Time Projection Chamber   A large-volume TPC is the central tracking component. It provides up to 224 precise measurements along the track of a charged particle. A momentum resolution of $\delta\left(\frac{1}{p_t}\right) \sim 9 \cdot 10^{-5}\,(\mathrm{GeV}/c)^{-1}$ can be achieved, while keeping the material budget as low as $0.04\,X_0$ for the field cage and $0.15\,X_0$ for the readout

endcaps. While the single point resolution of $\sigma_{r\Phi} < 100\,\mu$m and double-hit resolution of approximately $2\,$mm are moderate compared to silicon tracking, it provides quasi-continues tracking. This is of special interest for non-pointing tracks, which might be the signature of certain SUSY channels. In addition it provides dE/dx based particle identification with $5\,\%$ resolution, which is valuable for many physics analyses.

The combination of all tracking systems yields a an efficiency greater than $99\,\%$ for tracks with $p_t > 1\,$GeV$/c$.

Calorimeter System

To minimise confusion in the separation of close-by particle showers, the particle flow paradigm requires very fine transverse and longitudinal segmentation of the calorimeters. The calorimeter design is driven by the requirements of pattern recognition, rather than intrinsic single particle resolution. Still the latter is important, and the high granularity even offers the possibility of efficient software compensation for the difference between electromagnetic and hadronic response (cf. section 7.6.3). The main requirements on the calorimetric system are:

- hermeticity down to small polar angles;

- excellent energy resolution for jets;

- good angular resolution;

- capability to reconstruct non-pointing photons as a stand-alone device;

- good time resolution, to avoid event pile-up.

In addition, lepton identification from high to low momenta is important to separate purely hadronic jets from jets containing leptons, and thus enhance the flavour tagging capabilities.

The calorimetric system is divided into an electromagnetic section, optimised for the measurement of photons and electrons, and a hadronic one, dealing with showers induced by hadrons. Both calorimeters are placed within the magnetic coil, in order to minimise the amount of dead material in front of them. In z-direction ECAL and HCAL are divided into a barrel region, with approximately cylindrical symmetry, and two endcaps each.

Electromagnetic Calorimeter   The geometrical ECAL design is sketched in figure 3.6(a). An eightfold symmetry is approximating the cylindrical barrel shape of the TPC. Each octant is subdivided into five modules. The layout of one barrel module is illustrated in figure 3.6(b). The large size of the modules helps to minimise the number of cracks in the barrel region. Furthermore, the inter-module boundaries do not point back to the interaction point. The ECAL endcaps are divided into four modules each.

The ECAL provides 30 active layers and high transverse granularity. It can either be realised in silicon-tungsten structure, or as scintillator-tungsten sandwich. The first option, where the sensors are based on individual pin-diodes of $0.5 \times 0.5\,$cm^2 size, is assumed for the presented analysis.
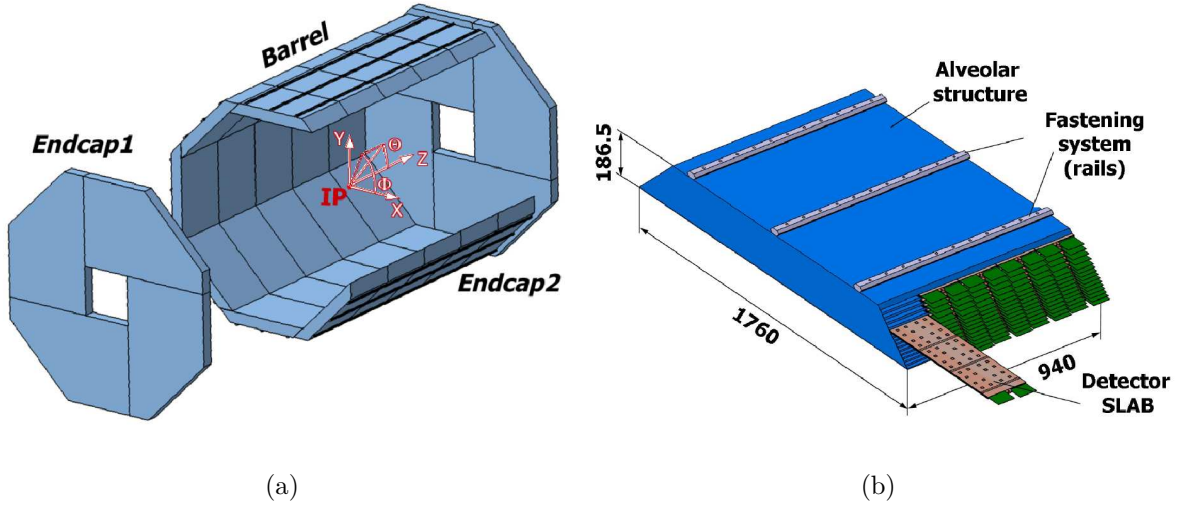
(a)   (b)

Figure 3.6: The electromagnetic calorimeter (a) global design and (b) module layout [51].

Tungsten ($X_0 = 0.35 \, \text{cm}$, $R_M = 0.93 \, \text{cm}$, $\lambda_i = 9.9 \, \text{cm}$) as ECAL absorber structure allows for a compact design, and provides a good separation of near-by electromagnetic showers. The high ratio of interaction length to radiation length facilitates the separation of electromagnetic and hadronic showers, since hadrons on average penetrate more material before developing a shower. For a given number of sampling layers the energy resolution improves if the inner part of the calorimeter is more finely segmented than the latter part. Therefore, the ECAL starts with an active layer, and the first 12 radiation lengths are filled with 20 layers of $0.6 \, X_0$ thick tungsten absorbers, followed by 11 radiation lengths of $1.2 \, X_0$ thick tungsten in 10 more layers. Altogether, they add up to a total depth of $23.6 \, X_0$, or roughly $1 \, \lambda_i$, within $20 \, \text{cm}$. With a cell size of $0.5 \times 0.5 \, \text{cm}^2$ pixels, which is smaller than the Molière radius of $0.9 \, \text{cm}$, this sums up to around 10^8 readout channels.

Measurements with a prototype, using $1.0 \times 1.0 \, \text{cm}^2$ pixels with 10 layers of $0.4 \, X_0$, 10 layers of $0.8 \, X_0$ and 10 layers of $1.2 \, X_0$ tungsten plates, achieved an energy resolution of

$$\frac{\sigma_E}{E} = \frac{(16.6 \pm 0.1) \, \%}{\sqrt{\text{E[GeV]}}} \oplus (1.1 \pm 0.1) \, \%. \tag{3.7}$$

The signal-over-noise ratio, defined as most probable value of a non-showering muon signal divided by the pedestal width, is measured to be $S/N \approx 7.5$ [63].

Hadron Calorimeter   The HCAL geometrical design is following the octagonal ECAL structure. It provides up to 48 longitudinal samples, and small cell sizes. Currently two technology options are under closer investigation. A digital version with only $1 \times 1 \, \text{cm}^2$ cell size, and a scintillator based one with slightly larger cells and analogue readout are under discussion. Both will be interleaved with steel plates as absorber. The digital HCAL design proposes gaseous active layers read out by glass resistive plate chambers [64]. In this thesis scintillating tiles are assumed to be the active medium (cf. chapter 6).

Stainless steel ($X_0 = 1.76 \, \text{cm}$, $R_M = 1.7 \, \text{cm}$, $\lambda_i = 16.8 \, \text{cm}$) is chosen as HCAL absorber structure. It is non-magnetic, and offers the possibility of a self-supporting structure.

Furthermore, the λ_i/X_0-ratio of steel allows a fine longitudinal sampling in terms of radiation length with a reasonable number of layers in a given depth in terms of interaction length. This is beneficial for the measurement of the electromagnetic component in hadronic showers. In addition a high granularity enables the application of weighting techniques to compensate for the difference between electromagnetic and hadronic response, which improves the energy resolution.

Each absorber plate is 2.0 cm thick, 48 of them sum up to $5.5 \lambda_i$ in the barrel. The active medium are scintillating tiles with 3.0×3.0 cm^2 width and 0.3 cm thickness.

Forward Calorimeters High precision calorimeters in the very forward region extend the angular coverage to almost 4π, which helps to tag background, e. g. in new particle searches.

- The LumiCal is a cylindrical electromagnetic calorimeter centred around the outgoing beam. Positioned within the ECAL end cap, it covers the polar angle from 32 mrad to 74 mrad. Its purpose is to provide a precise luminosity measurement with an accuracy of better than 10^{-3}, using Bhabha scattering as gauge process.

- The BeamCal delivers a fast luminosity estimation on bunch-to-bunch basis from beamstrahlung pairs. Just like the LumiCal, it is designed as cylindrical electromagnetic calorimeter. Located in front of the final focusing quadrupoles, it covers the polar angle range between 5 mrad and 40 mrad.

- The LHCAL is a hadron calorimeter, located inside the HCAL end cap. It is extending the HCAL coverage to small polar angles.

- The GamCal is an electromagnetic calorimeter, positioned 100 m downstream of the detector. It will assist in beam-tuning, by exploiting photons from beamstrahlung.

These very forward detectors have to deal with very high occupancies and a radiation dose of several MGy per year. Thus, the ongoing detector R&D focuses towards the development of radiation hard detectors, e. g. polycrystalline CVD diamond sensors for the BeamCal, and fast front-end electronics.

Magnet Coil and Muon System A superconducting coil surrounds the calorimetric system. It creates a solenoidal central field of 3.5 T in a volume of 6.9 m in diameter and a length of 7.35 m. The required integral field homogeneity is [65]

$$\left| \int_0^{2.25\,\mathrm{m}} \frac{B_r}{B_z}\, dz \right| \leq 10\,\mathrm{mm} \tag{3.8}$$

within the TPC volume.

The coil is surrounded by an instrumented iron yoke with twelve-fold symmetry, which returns the magnetic flux to the coil. The inner part of the barrel yoke is made from ten 10 cm thick iron plates interleaved with 4 cm spacing for instrumentation. Three 56 cm thick iron plates interleaved with 4 cm gaps for instrumentation form the barrel yoke rear part. The weight of the barrel yoke is around 7000 t.

The end caps follow a similar twelve-fold structure with ten 10 cm thick iron plates followed by two 56 cm thick iron plates. Analogue to the barrel structure, the iron plates are interleaved with 4 cm gaps for instrumentation. An additional 10 cm thick field shaping plate is added inside each end cap to improve the field homogeneity. The total weight of each yoke end plate sums up to 13400 t.

The instrumentation can be used as muon detector and tail catcher. Here two technologies are under consideration as well: scintillator strips, or resistive plate chambers.

Machine Detector Interface   The interaction region is a compromise between machine performance and detector backgrounds, while minimising the overall costs.

A small crossing angle of 14 mrad ensures that entering beams collide almost head-on, while allowing the outgoing beams to be guided safely out of the detector. To recover the full luminosity, the incoming beams are slightly rotated by crab-cavities before they reach the interaction point. Due to this rotation the beams pass through each other side-ways and hence the overlap of bunches is maximised.

The machine detector interface takes care about the final focusing quadrupoles, including their integrated sextupole and octupole correction elements, the beam position monitors and kickers that keep the beam in collision. In addition, it comprises the crab-cavities that rotate the incoming beams and the extraction line quadrupole magnets that direct the outgoing beams to the beam dumps.

Furthermore, to minimise background from the collided beam remnants, the outgoing beams are guided towards the beam pipe by an anti-DID (detector integrated dipole) field. This additional magnet is located outside of the solenoid.

4 Calorimetry

Calorimeters are instrumented blocks of matter, in which particles interact and deposit their energy in the form of a cascade of particles. The deposited energy is then detectable in the form of a visible signal E_{vis}, which is proportional to the energy of the incoming particle E_{p}:

$$E_{\mathrm{vis}} \propto E_{\mathrm{p}}. \tag{4.1}$$

This proportionality is the basis of all calorimetric measurements.

4.1 Calorimeter Classification

There are several ways to categorise calorimeters. They can either be homogeneous, i. e. active and absorbing material are the same, or sampling devices, where active material and passive absorbers alternate. Since only sampling calorimeters are proposed for the ILD detector, only these will be discussed in the following.

In sampling calorimeters, only the energy deposited in the active volume E_{vis} is measured. It is connected to the energy deposition in the full calorimeter (active plus absorber material) E_{tot}, via the sampling fraction

$$SF = E_{\mathrm{vis}}/E_{\mathrm{tot}}. \tag{4.2}$$

Electromagnetic calorimeters (ECAL) are optimised for the measurement of electrons, positrons and photons. Electromagnetic processes and their properties are discussed to some detail in section 4.3.

On the other hand, hadron calorimeters (HCAL) are devoted to the detection of hadronic particles, e. g. pions and kaons. Hadron showers underly much larger fluctuations than electromagnetic ones. Their cascades are still not understood in detail. This is, for example, reflected in the variety of hadronic shower models in simulations with very different predictions. It is one of the aims of the physics prototype described in chapter 6 to contribute to a better understanding of hadronic showers by exploiting the high lateral and longitudinal granularity. The presented analysis is only concentrating on electromagnetic showers. Thus, hadronic showers will not be discussed in detail.

4.2 Electromagnetic Interactions of Particles and Matter

Particles traversing matter can interact with the electric field of the atom, or with the atomic nucleus. Due to these interactions, the initial energy is degraded, and the original direction is disturbed. These interactions are important for the understanding and

development of calorimeters, and the study of shower properties. This section provides an overview of the most relevant processes for electromagnetic showers, discussed in sections 4.2.1 and 4.2.2. A more detailed discussion of the development of particle showers follows in section 4.3.

4.2.1 Interaction of Electrons with Matter

Acceleration of charged particles, e. g. the deflection of an electron passing through the electric field of an atomic nucleus, causes electromagnetic radiation called bremsstrahlung. This process is the main reason for energy loss of highly energetic electrons and positrons, and as such responsible for the development of electromagnetic cascades up to the shower maximum.

The mean energy loss dE by bremsstrahlung on a path dx is given by:

$$-\left\langle \frac{dE}{dx} \right\rangle_{\text{brems}} = \frac{E}{X_0}. \tag{4.3}$$

The natural unit of electromagnetic showers is the radiation length [66, 67]

$$\frac{1}{X_0} = 4\alpha \frac{N_A}{A} Z(Z+\zeta) r_e^2 \ln\left(\frac{183}{Z^{1/3}}\right) \approx \frac{1}{180} \frac{Z^2}{A} \left[\frac{\text{cm}^2}{\text{g}}\right], \tag{4.4}$$

where α is the fine structure constant, N_A is the Avogadro constant, A the atomic weight, Z the atomic number of the medium, r_e the classical electron radius, and $1.2 < \zeta < 1.4$ is a correction factor that accounts for the contribution of atomic electrons to the overall bremsstrahlung process. On average, an electron has lost $1/e$ of its initial energy after $1\,X_0$.

As shown in figure 4.1(a), the energy loss by bremsstrahlung is the main interaction process for electrons and positrons with high energy ($E_{e^\pm} \gtrsim 10\,\text{MeV}$). At a certain critical energy ε_c the energy loss by ionisation becomes dominant. Once the electron energy falls below this threshold, the multiplication of particles stops and the shower ceases.

Also presented in figure 4.1(a) are the less dominant energy loss processes of Møller scattering ($e^-e^- \to e^-e^-$), Bhabha scattering ($e^+e^- \to e^+e^-$) and positron annihilation ($e^+e^- \to \gamma\gamma$). Furthermore, electrons and positrons can interact via multiple scattering. This mainly causes a change of direction, and does not transfer a significant amount of energy.

4.2.2 Interaction of Photons with Matter

The interactions of photons with matter differ fundamentally from the interactions of electrons or positrons. Charged particles lose energy in a continues stream of events in which they ionise the traversed material and radiate photons. Photons on the other hand, can penetrate the same thickness of matter without being affected at all. For example, the probability that a photon interacts in 1 cm of lead is only 75 %. The main interactions of photons with matter are shown in figure 4.1(b) as a function of the photon energy.

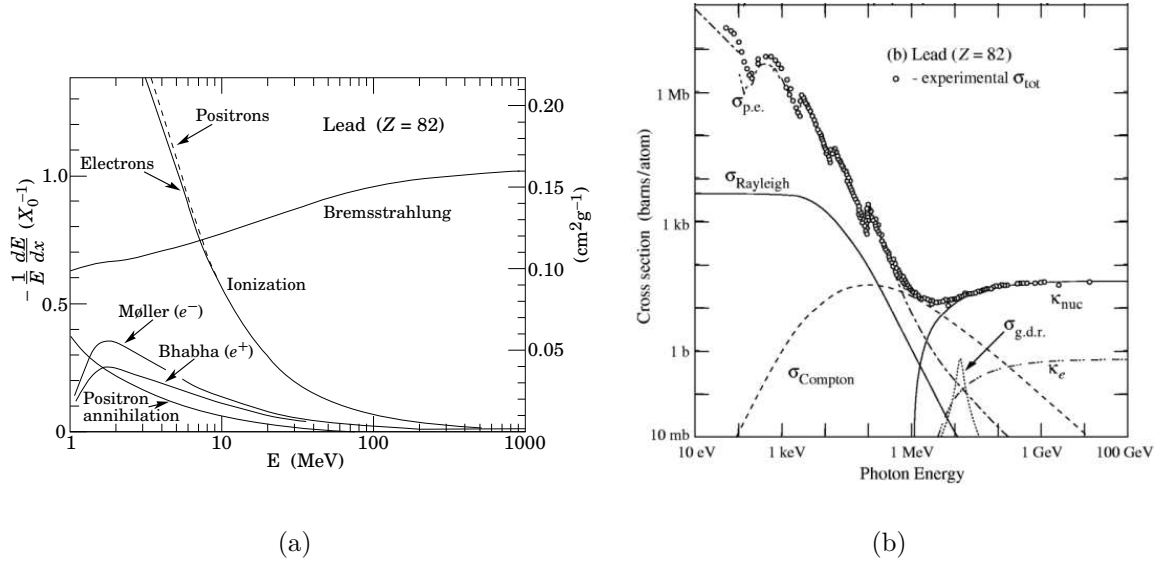(a)   (b)

Figure 4.1: Electromagnetic shower processes [4] as a function of the particle's energy. Process dependent cross section for (a) electrons and (b) photons in lead.

At high energies ($E_\gamma \geq 2 \cdot m_e c^2$) the dominant process is pair production $\gamma \rightarrow e^+ e^-$. This process determines the shower development up to the shower maximum. It can occur in the field of a nucleus κ_{nuc} or an electron κ_e and is responsible for the shower development up to the shower maximum. The produced electrons are eventually absorbed by an ion, while the positrons annihilate with electrons. The mean free path for pair production by an highly energetic photon is [68]

$$\lambda_\gamma \approx 9/7 \, X_0. \tag{4.5}$$

Compton scattering ($\gamma e^- \rightarrow \gamma e^-$), which describes the elastic scattering of a photon on a free electron, contributes to the energy loss of photons with medium energy. Typically, half of the total energy of multi-GeV electrons, positrons or photons is deposited by Compton scattered photons. Its cross section changes with photon energy as $\sigma_{\mathrm{Compton}} \sim E_\gamma^{-1}$.

At lower energies, the energy loss of photons is dominated by the photoelectric effect, where a highly energetic photon is absorbed by an electron and the electron is released from its nuclear bounds afterwards. The cross section for this process scales with $\sigma_{p.e.} \sim E_\gamma^{-3}$.

A minor contribution to the photon cross section at small energies arises from Rayleigh scattering. In this process, the photons scatter elastically on particles with a diameter smaller than their wavelength, and in which the atom gets neither excited nor ionised. At higher energies, giant dipole resonances (g.d.r.), that describe photonuclear interactions which break up the target nucleus, contribute to the energy loss of photons.

4.2.3 Interaction of Muons with Matter

Ionisation is the basis of most particle detectors. Charged particles traversing matter interact with the electrons of atoms in that material. This leads to an excitation, or

ionisation of the traversed material, and an energy loss of the traversing particle. The mean differential energy loss $-dE$ of the traversing particle on a path dx in a material with atomic number Z and atomic mass A is given by the Bethe-Bloch-Formula [69]:

$$-\left\langle \frac{dE}{dx} \right\rangle_{\text{ion}} = K \left(\frac{z}{\beta} \right)^2 \frac{Z}{A} \left[\frac{1}{2} \ln \frac{2m_e c^2 \beta^2 \gamma^2 T_{\text{max}}}{I^2} - \beta^2 - \frac{\delta(\beta\gamma)}{2} \right], \qquad (4.6)$$

in which T_{max} equals the maximum kinetic energy that can be transferred to an electron in a single collision. I is the mean excitation energy of the absorber material and $\delta(\beta\gamma)$ is a correction term describing the density effect. $m_e = 0.511\,\text{MeV}$ is the electron mass and $r_e = 2.82 \cdot 10^{-15}\,\text{m}$ is the classical electron radius. $K \approx 0.31\,\text{MeVg}^{-2}\text{cm}^{-2}\text{mol}$ is a constant factor, while z represents the charge of the incident particle.

The energy loss of relativistic muons decreases with increasing energy, until it reaches a minimum of approximately $1.5\,\text{MeV/g} \cdot \text{cm}^2$ at $\beta\gamma \approx 3.5$ in iron. A muon close to this minimum is called 'minimum ionising particle' (MIP)[1]. At increasing energies the minimum is followed by a relativistic rise.

4.3 Electromagnetic Showers

The first observations of electromagnetic showers were from P. M. S. Blackett and G. P. S. Occhialini, who investigated high-energetic cosmic rays in 1933 [70]. By now, these showers can be described with high precision within the theory of quantum electrodynamics. This section introduces the basic ideas of cascading electromagnetic showers and gives a short overview of the most important variables needed to describe the shower development.

4.3.1 A Very Simple Model

The most simplified model, sketched in figure 4.2, is based upon the following restrictions:

- The incoming charged electron has a starting energy $E_p = E_0$ that is much greater than the critical energy, ε_c.

- Each electron with $E_p > \varepsilon_c$ travels one radiation length and then gives half of its energy to a bremsstrahlung photon.

- Each photon produced with energy $E_p > \varepsilon_c$ travels one radiation length and creates an electron-positron pair with each particle carrying away half the energy of the original photon.

- Electrons with $E_p < \varepsilon_c$ cease to radiate and then lose the rest of their energy by collisions.

- Photons with $E_p < \varepsilon_c$ lose the rest of their energy via Compton scattering and the photoelectric process.

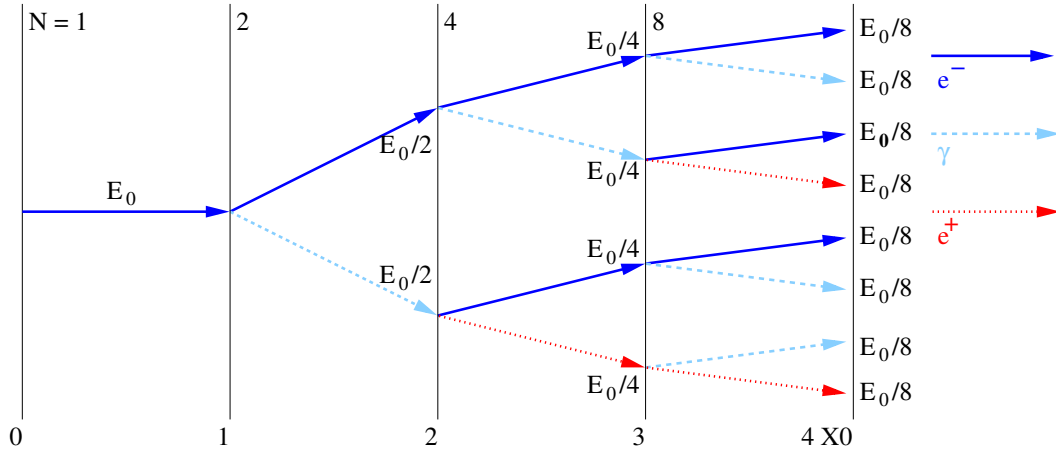- The difference in cross section for high-energy electrons and positrons are neglected.

Figure 4.2: Sketch of a simple electromagnetic shower induced by an electron with $E_0/8 > \varepsilon_c$. Electrons (solid, dark blue line), positrons (dotted, red line) and photons (dashed, light blue line) undergo an interaction after each radiation length.

In this model the number of particles is roughly doubled after each interaction step t

$$N_p(t) = 2^t,$$

while the energy per particle is on average divided in half

$$E_p(t) = \frac{E_0}{N_p(t)} = 2^{-t}E_0.$$

After $4\,X_0$ this results in 8 particles, each of them having one eighth of the initial energy.

At the maximum particle multiplication, the shower depth is

$$t_{\max} \approx \ln \frac{E_0}{\varepsilon_c}.$$

At this point, the particles reach the critical energy $E_p = \varepsilon_c$ at which the energy loss by bremsstrahlung equals the energy loss by collisions (ionisation and excitation). Afterwards the remaining soft electrons lose their energy mainly by ionisation, while soft photons interact dominantly via Compton scattering and the photoelectric process. Thus, the cascade decreases, following an exponential decay $e^{-t/\lambda_{\mathrm{att}}}$ with a characteristic attenuation length λ_{att}.

Some properties relevant to describe the shower development, are listed in table 4.1 for selected materials that are frequently used in calorimeters. Next to the material density ρ, the table lists some atomic number Z dependent properties. Namely, the radiation length $X_0 \propto 1/Z^2$ (cf. section 4.2.1), the Molière radius $R_M \propto 1/Z$ (cf. section 4.3.3) and the critical energy $\varepsilon_c \propto 1/Z$ (cf. section 4.2.1). Furthermore, the ratio of nuclear interaction length λ_i (cf. equation 4.28) and radiation length is an important characteristic for the separation of electromagnetic and hadronic showers.

---

[1] A MIP is an hypothetical particle that is only losing energy by ionisation.

Material	Symbol	ρ [g/cm^3]	X_0 [cm]	R_M [cm]	ε_c [MeV]	λ_i/X_0
Copper	Cu	9.0	1.44	1.57	18.79	10.64
Iron	Fe	7.9	1.76	1.72	21.68	7.82
Lead	Pb	11.4	0.56	1.60	7.43	31.41
Tungsten	W	19.3	0.35	0.93	7.97	28.43
Lead glass		6.2	1.27	2.58	10.05	20.00
Scintillator	$[C_6H_5CHCH_2]_n$	1.1	41.31	9.41	90.65	1.87
Liquid Argon	LAr	1.4	14.00	9.04	31.91	3.13
Silicon	Si	2.3	9.37	4.94	39.05	4.96

Table 4.1: Shower relevant properties of some elements and compounds frequently used in calorimeters [71].

On average, hadronic showers start deeper and extend into greater depth compared to electromagnetic ones. The larger the λ_i/X_0-ratio, the better the distinction between these showers. The ratio scales linearly with Z, thus the best separation can be achieved for high-Z absorber materials.

The first part of the table lists typical absorber materials, while the lower part summarises common active materials. Lead glass is a hybrid, namely absorber and active medium at the same time.

4.3.2 Longitudinal Shower Development

A simplified analytical model of the cascade development, though more complex than the one sketched in section 4.3.1, was proposed by B. Rossi, and is commonly known as "approximation B" [72]. It assumes energy independent collision losses per radiation length, and neglects differences between electrons and positrons.

The longitudinal profile of a shower induced by a particle with incident energy E in GeV traversing a matter depth t can be described as [73]

$$f(t) = \frac{dE}{dt} = at^\omega \cdot e^{-bt}, \tag{4.7}$$

with parameters ω and b. The first term represents the fast shower rise, in which the particle multiplication is ongoing. The second term parametrises the exponential shower decay.

Giving this parametrisation with t in units of radiation lengths, the particle multiplication and the energy deposition reach their maximum after

$$t_{\max} = \frac{\omega}{b} = \left[\ln \frac{E_0}{\varepsilon_c} + f \right] \tag{4.8}$$

radiation lengths from the beginning of the cascade. The constant f is -0.5 for incident electrons and $+0.5$ for photons. This position is called shower maximum.

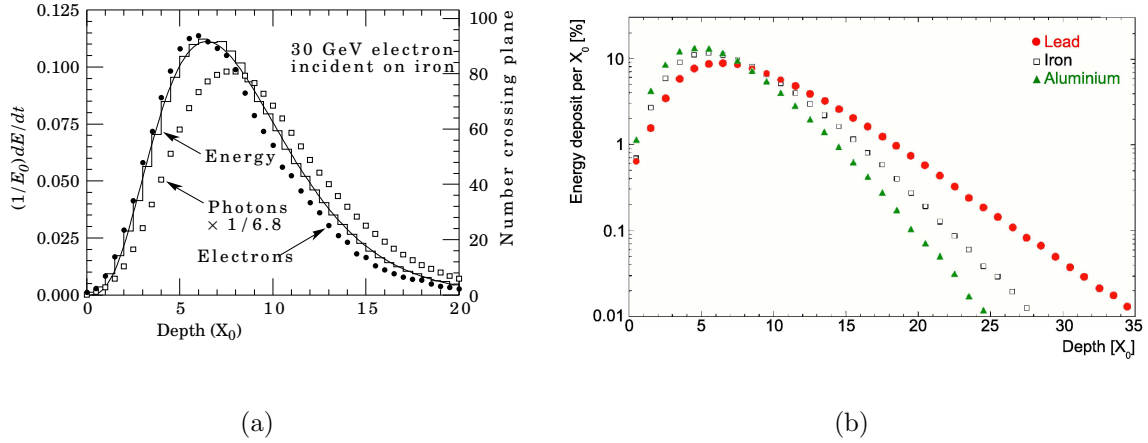(a)   (b)

Figure 4.3: Simulated longitudinal profile of (a) 30 GeV electrons in iron [4]; and (b) 10 GeV electrons in lead, iron and aluminium [74].

The decay of the cascade after the maximum can be described by the longitudinal attenuation length

$$\lambda_{\text{att}} = \frac{1}{b}. \tag{4.9}$$

It shows little dependence on the incoming particle's energy, since it is mainly effected by low energetic photons.

When the shower expands over several materials, the total radiation length is given by

$$\frac{1}{X_{g0}} = \sum_i \frac{f_i}{X_{g0,i}}, \tag{4.10}$$

with the mass fraction f_i of the i-th absorber with radiation length $X_{g0,i}$ given in units of g/cm^2. To obtain the more common radiation length X_0 expressed in cm, one has to divide X_{g0} by the material density ρ given in units of g/cm^3.

The longitudinal containment of 95 % of the cascade energy can be parametrised as [75]

$$L(95\,\%) = t_{\text{max}} + 0.08Z + 9.6, \tag{4.11}$$

again expressed in units of radiation length.

Longitudinal profiles from an EGS4 simulation of a 30 GeV electron-induced cascade in iron [4] are shown in figure 4.3(a). Plotted is the fractional energy deposition per radiation length. Circles indicate the number of electrons with energy greater than $E \geq 1.5$ MeV crossing planes at $X_0/2$ intervals (right axis). The number of photons with energy more than $E \geq 1.5$ MeV, scaled down to the same area as the electron distribution, is displayed as open squares. The curve is a fit to the distribution. The number of particles crossing a plane is sensitive to the cutoff energy, here chosen as a total energy of 1.5 MeV for both electrons and photons. The number of electrons decreases faster than the energy deposition, because with increasing depth, a larger fraction of the cascade energy is carried by photons.

The material dependence of the shower development [74] is illustrated in figure 4.3(b). The simulated energy deposition from a 10 GeV electron in aluminium ($Z = 13$), iron

($Z = 26$) and lead ($Z = 82$) is displayed as a function of the calorimeter depth. As Z increases, the shower maximum moves to greater depth and the shower decay beyond the maximum slows down.

Measuring showers with a fine longitudinal sampling, in the order of one radiation length per layer, allows an accurate topological reconstruction of the shower development. This opens the possibility to identify MIP-like tracks within hadronic showers, which can be utilised to calibrate the detector [76].

4.3.3 Lateral Shower Development

In the plane perpendicular to the incident particle, the cascade evolves due to secondary electrons, which are no longer aligned with the incoming particle. Furthermore, secondary Compton photons do not have to follow the path indicated by the primary photon. Multiple Coulomb scattering of soft electrons may change the electron direction, and contribute to the widening of the shower as well.

The lateral shower development is described in terms of the Molière radius

$$R_M = \left(\frac{E_M}{\varepsilon_c}\right) X_0, \tag{4.12}$$

where $E_M = \sqrt{\frac{4\pi}{\alpha}}(m_e c^2) \approx 21.2 \, \text{MeV}$. Analogue to the radiation length, the Molière radius of compound materials is composed as [73]

$$\frac{1}{R_{gM}} = \frac{1}{E_M} \sum_i \left(f_i \frac{\varepsilon_{ci}}{X_{g0i}}\right), \tag{4.13}$$

for a Molière radius R_{gM} in g/cm^2, and f_i, ε_{ci}, and X_{g0i} as defined in equation 4.10.

Roughly 90 % of the energy are contained within one Molière radius. The 95 % radial containment for electromagnetic cascades is given by

$$R_e(95 \, \%) = 2R_M. \tag{4.14}$$

As visible in figure 4.4, the lateral development can be divided into a narrow central, and a broader peripheral part. The central part is mainly due to multiple scattering effects produced by fast electrons. It scales with the Molière radius ρ_M and is almost Z independent, whereas the slope of the halo gets steeper as Z decreases. The peripheral part is mainly caused by soft electrons in Compton scattering and photoelectric absorption, and thus directly related to the mean free path of the photons responsible for these processes. An empirical estimation of the radial shower development, accounting for this double structure is given by [77]

$$f(r) = P\frac{2rR_c^2}{(r^2 + R_c^2)^2} + (1 - P)\frac{2rR_t^2}{(r^2 + R_t^2)^2}, \tag{4.15}$$

where $0 \leq P \leq 1$ is the probability to be in the shower core, and R_c and R_t are the medians of the core and the tail component of the radial profile. This parametrisation lead to reasonable agreement with experimental data from the H1 experiment at HERA in the core as well as in the halo of the shower [78].
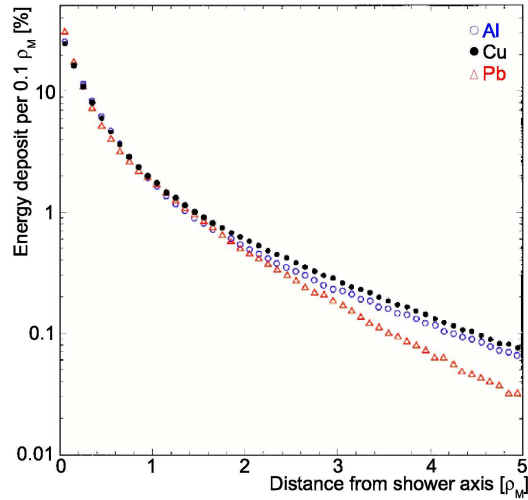
Figure 4.4: Simulated radial energy deposition of $10\,\mathrm{GeV}$ electrons in aluminium, copper and lead [74].

The spatial distribution of an electromagnetic shower can then be expressed as the product of three probability density functions

$$dE(\vec{r}) = E\,f(t)\,dt\,f(r)\,dr\,f(\Phi)\,d\Phi, \qquad (4.16)$$

describing the longitudinal (cf. equation 4.7), radial (cf. equation 4.15) and azimuthal distribution $f(\Phi)$. Here t is the longitudinal shower depth in units of radiation length, r is the distance from the shower axis in units of Molière radii and Φ is the azimuthal angle, which is assumed to be uniform, i.e. $f(\Phi) = 1/2\pi$.

A high lateral granularity, not larger than one Molière radius per cell, allows the separation of close-by showers with high accuracy, which is a key requirement for particle flow (cf. section 3.3.1). Furthermore, the distribution of each shower over several cells allows to use shower shape parameterisations, as given in equation 4.16 for particle identification and reconstruction. This improves the determination of the shower position and angular orientation (cf. section 4.3.4), which is interesting for long-lived neutral particles (cf. chapter 5).

4.3.4 Position Resolution

The impact point of the incident particle can be reconstructed from the energy weighted centre of gravity

$$\langle \vec{x} \rangle = \frac{\sum_i \vec{x}_i E_i}{\sum_i E_i}. \qquad (4.17)$$

Here, $\vec{x}_i = (x, y, z)$ and E_i are the position and the energy of cell i, respectively. Since this method implies a systematic shift of the reconstructed position towards the centre of a cell, a good position resolution requires a high lateral granularity.

The resolution improves as the number of contributing cells increases. In electromagnetic cascades, high-energetic particles stick close to the incoming particle's direction. As a consequence the lateral shower size remains very narrow. Nevertheless, in longitudinal direction more cells contribute to the position measurement. Thus, also

a high longitudinal sampling is improving the position resolution, which scales with energy as

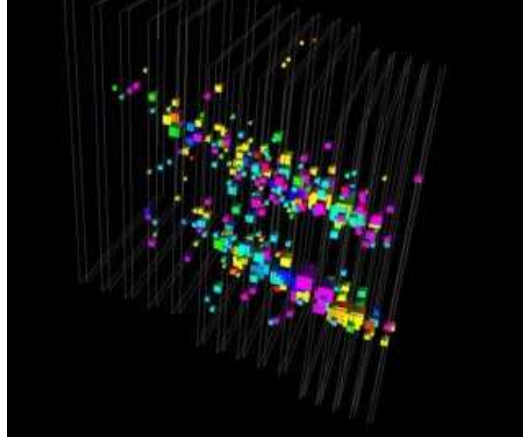$$\sigma_{\langle \vec{x} \rangle} \propto \frac{1}{\sqrt{E}}. \tag{4.18}$$

Figure 4.5: Event display of two close-by electron showers in the CALICE Si-W ECAL. Due to the high longitudinal and transverse granularity close-by showers can be separated.

In sampling calorimeters, the shower spread varies with the longitudinal depth. Projecting this lateral distribution onto a plane orthogonal to the main shower axis gives an exponential decrease, according to [79]

$$E(x) \sim \exp\left(-\frac{4x}{R_M}\right), \tag{4.19}$$

where x is the coordinate orthogonal to the main shower axis.

As the Molière radius of the absorber is usually smaller than that of the active medium (cf. table 4.1), the cascade size is smaller in the absorber. The widening of the shower due to the alternating structure of active and passive medium can lead to an overlap of adjacent showers. This effect worsens if the lateral granularity gets coarser.

The event display given in figure 4.5 demonstrates the good position resolution of the highly granular CALICE silicon-tungsten ECAL. Although the electrons are only few centimetres apart, the two resulting showers can be clearly distinguished. This high spatial resolution, inspired by the paradigm of particle flow, allows to separate single showers within hadronic jets.

The angular orientation of a shower can be determined from the inertia tensor

$$\mathcal{T} = \sum_i E_i \begin{pmatrix} dy_i^2 + dz_i^2 & -dx_i\,dy_i & -dx_i\,dz_i \\ -dy_i\,dx_i & dx_i^2 + dz_i^2 & -dy_i\,dz_i \\ -dz_i\,dx_i & -dz_i\,dy_i & dx_i^2 + dy_i^2 \end{pmatrix}, \tag{4.20}$$

where $da_i = a_i - \langle a \rangle$ for $a \in x, y, z$ is the distance of the hit position to the centre of gravity and the index i is running over all cells contributing to the shower.

The matrix is diagonalised to get the eigenvectors and eigenvalues, which correspond to the inertia axes and momenta. The axis with the largest eigenvalue is taken as main principal axis and determines the shower direction.

4.3.5 Energy Resolution

The energy is measured in the active medium of sampling devices, while the shower is mainly generated in the passive absorber. The fraction of energy deposited in the active medium underlies statistical fluctuations on an event-by-event basis. These fluctuations result in fluctuations of the visible energy E_{vis}, and thus broaden the distribution of the measured energy. Furthermore, many calorimeters have different sampling fractions at increasing depth, in which case the fraction of sampled energy E_{vis} is effected by fluctuations in the longitudinal shower evolution, too. Due to the statistical character of the cascade processes, the energy distribution for incoming particles with energy E is a Gaussian distribution with a standard deviation σ_E.

The intrinsic sampling fluctuations are proportional to the mean energy deposition per charged particle N_{cp}, which is in turn affected by the average number of particles. Therefore, the energy resolution can be described as:

$$\left(\frac{\sigma_E}{E}\right)_{\mathrm{stat}} = \frac{\sigma_{E_{\mathrm{vis}}}}{E_{\mathrm{vis}}} \approx \frac{1}{\sqrt{N_{\mathrm{cp}}}}. \tag{4.21}$$

This equation underlines one of the reasons why calorimeters become more important in recent particle physics experiments: their resolution improves with increasing energy.

Usually the statistical fluctuations are not the only contribution to a degradation of the energy resolution. Calibration uncertainties and non-linearities lead to an energy-independent degradation of the energy resolution:

$$\left(\frac{\sigma_E}{E}\right)_{\mathrm{const}} \propto c. \tag{4.22}$$

These effects are the main source of resolution degradation at high energies. Non-linearities can occur in non-compensating hadron calorimeters (cf. section 4.4), but they can also be introduced by saturation effects of the detector or the read-out electronics. Achieving a linear energy response is crucial to obtain a reasonable energy resolution, and large efforts are undertaken to realise a linear response for the ILD calorimeters. They are discussed in more detail on the example of a hadron calorimeter physics prototype in section 6.3.1 and 6.3.3.

Another source of non-linearities are lateral and longitudinal leakage. The shower start varies on an event-by-event basis, which directly influences the amount of longitudinal leakage in each event for a calorimeter with limited depth. And although in principle a calorimeter should always be deep and wide enough to contain the full shower, in practice this has to be balanced against other sub-detector requirements and cost to the best overall detector performance. Corrections for longitudinal leakage are understood and can be partly accounted for [80].

The emergence of cracks and dead areas, e. g. due to supporting structures, or in the transition region of various sub-detectors, is unavoidable and contributes to lateral shower leakage. Another origin of leakage are dead cells, but the most prominent contribution is often due to clustering effects in the reconstruction. The energy of a particle is usually determined in a certain region around the shower axis. Energy deposited outside of this cluster region is not reconstructed, and thus also some kind of lateral leakage.
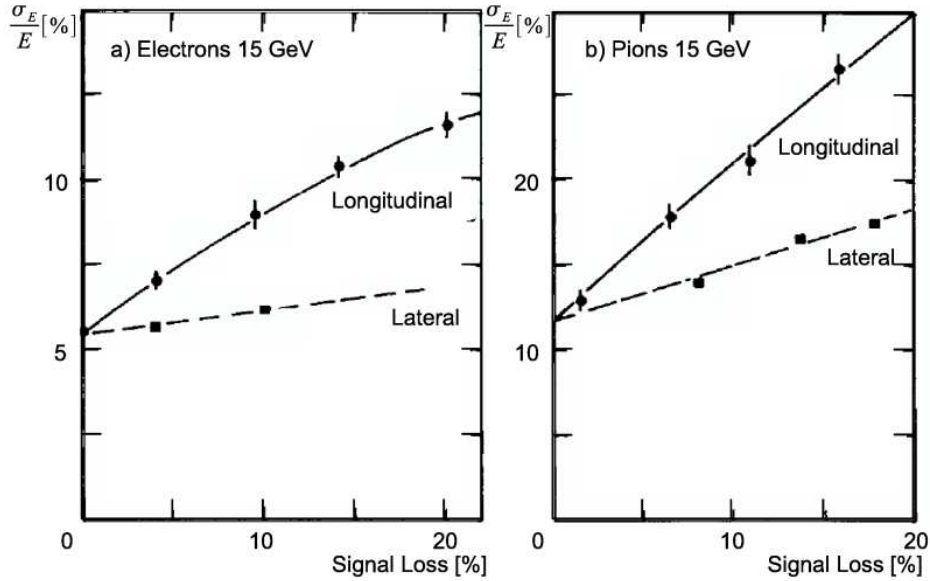
Figure 4.6: Influence of lateral and longitudinal leakage on the energy resolution [67].

The effects of lateral and longitudinal shower leakage have been studied in a marble absorber calorimeter by the CHARM collaboration [67]. The energy resolution measured as function of the signal loss, illustrated in figure 4.6, degrades much faster for longitudinal leakage than for lateral signal losses. This originates from the different fluctuations in longitudinal and lateral shower development, that lead to these leakage effects. While the longitudinal leakage is dominated by the fluctuations in the shower starting point, i. e. by the statistical behaviour of the initial particle, lateral leakage is influenced by fluctuations of some hundred particles. In the case of electromagnetic showers, lateral leakage originates from Compton and photoelectrons produced by soft photons. The lateral leakage in hadron showers is primarily caused by neutrons, depositing their energy in nuclear interactions.

Instrumental effects, e. g. electronics noise, do also play an important role. The calorimeter signal corresponds to a charge, collected during a given gating time. Since every detector has a certain capacitance, there is always some basic charge collected in this time, even in the absence of a particle cascade. Just like the signal events, it can be translated into a corresponding amount of energy. This pedestal underlies fluctuations, which are totally independent of the cascade development. They add to the energy resolution as

$$\left(\frac{\sigma_E}{E}\right)_{\text{noise}} \propto \frac{b}{E}, \tag{4.23}$$

and are the limiting contribution at low energies.

Since all these processes are statistically independent, the total energy resolution can be described as

$$\frac{\sigma_E}{E} \;=\; \frac{a}{\sqrt{E}} \oplus \frac{b}{E} \oplus c \tag{4.24}$$

$$=\; \sqrt{\left(\frac{a}{\sqrt{E}}\right)^2 + \left(\frac{b}{E}\right)^2 + c^2}, \tag{4.25}$$

Experiment	Calorimeter	$a\,[\sqrt{\text{GeV}}]$	$b\,[\text{GeV}]$	$c\,[\%]$
OPAL [81]	Lead glass ECAL	6.3		0.2
	Wire-Fe HCAL	120		
ALEPH [82]	Wire-Pb ECAL	17.8		1.9
	St. Tube-Fe HCAL	85		
ATLAS	LAr ECAL [83]	10.1 ± 0.1		0.17 ± 0.04
	Sc.-Fe HCAL [84]	58 ± 3	1.7 ± 0.2	2.5 ± 0.3
CMS	PbWO$_4$ ECAL [85]	3.4 ± 0.1	0.11	0.25 ± 0.02
	Sc.-Cu HCAL [86]	112 ± 1.1		3.6 ± 0.2
ILD [60]	Si-W ECAL	10		1
	Sc.-Fe HCAL	50		4

Table 4.2: Energy resolutions of former, operating and planned calorimeters.

where the energy E is given in units of GeV. The single contributions are also known as stochastic term $a/\sqrt{E}$, noise term b/E and constant term c.

The energy resolutions achieved with some existing calorimeters, and the design resolutions of the planned ILD calorimeters are listed in table 4.2. While the position resolution requirements for the ILD calorimeters are unprecedented, the energy resolution requirements are modest and have already been achieved by other large high-energy experiments, e.g. ATLAS.

4.4 Hadronic Showers

A complete theory of hadronic showers does not exist. The current description and simulation of hadronic interactions is based on phenomenological understanding and parametrisation of data. Therefore, it is very important to measure hadronic showers in great detail, to gain a better understanding. This is one of the motivations for the physics prototype described in chapter 6.

The particle multiplicity in a hadronic cascade increases logarithmically with the available energy. About half of this energy is carried on by leading particles, while the other half is absorbed in the production of secondaries. Not all of this energy is detectable. Neutrons often escape the detector volume without interactions, and the energy needed to break up nuclear bindings cannot be measured at all.

Roughly one third of the produced pions are neutral π^0. They give rise to the electromagnetic component f_{em} of hadronic showers. On average,

$$n_0 \approx 5 \ln E - 4.6 \tag{4.26}$$

neutral pions are produced at an energy E expressed in units of GeV [87]. The average fraction f_{em} of the incoming hadron energy deposited by electromagnetic shower scales like

$$f_{\text{em}} \approx (0.11 - 0.12) \ln E \tag{4.27}$$

with the incoming hadron energy expressed in GeV [88]. This estimation has been obtained from Monte Carlo simulations. It is only applicable to showers between few GeV and few TeV. For smaller energies it predicts negative electromagnetic fractions and above it gives electromagnetic fractions larger than one. The electromagnetic fraction of a hadronic cascade is largely determined by the production of π^0- and η-mesons in the first interaction and thus, underlies large event-to-event fluctuations.

The longitudinal development of a hadronic cascade can be described in terms of the hadronic interaction length [67, 4]

$$\lambda_i = \frac{Z}{N_A \rho \sigma_{nA}} \approx 35 \frac{A^{1/3}}{\rho} \, \text{cm}, \tag{4.28}$$

where A, N_A and ρ are the atomic weight, the Avogadro number and the material density in units of g/cm^3, respectively. Measurements of the inelastic cross section σ_{nA} expressed in cm^{-2} with incoming neutrons on a nucleus with atomic weight A, show that these cross sections are approximately independent of the particle momentum [4].

The spatial development of hadronic cascades is subject to large fluctuations, and depends strongly on the electromagnetic fraction f_{em}. Showers with large electromagnetic contributions are much more compact than those with small π^0 content. In general, hadronic showers are wider than electromagnetic ones and have a smaller energy density. Another difference, often used to discriminate between these two showers types, is the ratio of energy deposited at the beginning of a shower to the total deposited energy. In electromagnetic showers, most of the energy is deposited in the front of the calorimeter, while hadronic showers are spread over a wider range.

A large A-dependent fraction of the incoming hadron energy is spent in releasing nucleons and nucleon aggregates. This energy deposition, which has no correspondence in the electromagnetic counterpart, does not contribute to the visible energy E_{vis}. Thus, the amount of measured signal per incoming energy is smaller for hadrons than for electrons or photons.

For ideal hadronic cascades, i. e. without electromagnetic component, the ratio between electromagnetic and hadronic scale is defined as

$$e/h \equiv \frac{E_{\text{vis}}(e)}{E_{\text{vis}}(h)}, \tag{4.29}$$

where E_{vis} is the visible energy for electrons (e), and hadrons (h) at the same energy. The e/h ratio is usually larger than 1. It can be considered as an intrinsic property of the calorimeter.

However, cascades of real hadrons always carry an electromagnetic fraction. This can be parametrised as [73]

$$e/\pi \equiv \frac{E_{\text{vis}}(e)}{E_{\text{vis}}(\pi)} = \frac{E_{\text{vis}}(e)}{f_{\text{em}} E_{\text{vis}}(e) + (1 - f_{\text{em}}) E_{\text{vis}}(h)} = \frac{e/h}{1 - f_{\text{em}}(1 - e/h)}. \tag{4.30}$$

Since f_{em} is energy dependent, e/π is energy dependent as well. As it does not scale linearly with the incoming energy, most hadron calorimeters are intrinsically not linear.

To regain linearity, the compensation condition $e/\pi = e/h = 1$ has to be restored. Only if the calorimeter response is linear, the resolution improves with energy as $1/\sqrt{E}$.

Compensation can be achieved by choosing an appropriate mixture of active and passive material, as has been done by the ZEUS collaboration [89], or by applying the correct weighting factor to each hit. The latter approach, also referred to as software compensation, is the aim of the current ILD detector design.

Only if compensation is achieved, the calorimeter response to hadrons can be calibrated with electron beams of known energy, where the response to electrons is taken to be equal to the beam energy E_{beam} (cf. section 6.3.1).

4.5 Summary

Calorimetry is very important for particle physics experiments. The aimed jet energy resolution for the ILD detector can only be achieved, if special attention is given to the development of highly granular calorimeters with a moderate energy resolution, and on the development of shower reconstruction algorithms. The characteristics of electromagnetic interactions presented in this chapter can be used for the understanding of calorimeters, and the study of shower properties.

The theory of electromagnetic showers are well understood and the description of electromagnetic processes in simulations is better than 1%. Thus, they are convenient to benchmark the detector understanding of new calorimeter developments (cf. chapter 7), even if it is a hadron calorimeter. It should be emphasised that a linear response on the electromagnetic scale is crucial to judge the detector performance. Once the performance is verified at the electromagnetic scale, it is possible to proceed to the not as good understood physics of hadronic showers.

A high detector granularity enables particle identification on the basis of shower shapes. In addition, it enhances the capability of software compensation and thus allows to compensate for fluctuations of the electromagnetic component in hadronic showers. Furthermore, the determination of the direction of neutral particles, e.g. to reconstruct secondary vertices from SUSY signatures (cf. chapter 5), is only possible if the lateral cell size is not larger than the Molière radius of the absorber material.

5 Neutralino Lifetime Determination

A gauge-mediated SUSY breaking scenario is chosen to evaluate the performance of the electromagnetic sandwich calorimeter proposed for the International Large Detector. With a centre-of-mass energy of $500\,\mathrm{GeV}$, the next-to-lightest SUSY particle, which is a neutralino in the investigated scenario, can be pair-produced at the International Linear Collider. The subsequent decay results in two highly energetic photons and missing energy in the detector. Depending on the lifetime of the neutralino this decay can occur at a measurable distance from the interaction point. To reconstruct the secondary vertex from this decay is a very challenging task for the pattern recognition of the electromagnetic calorimeter.

The main motivation of this study is not to investigate a broad spectrum of SUSY scenarios, but to test the ECAL performance in terms of energy, position and angular resolution. As the reconstruction of the neutralino mass and lifetime requires both, good photon energy reconstruction and excellent photon pointing resolution, neutralino decays in GMSB are a good physics channel to test the full ECAL performance.

One example GMSB scenario is studied in full detector simulation. Three neutralino lifetimes are chosen to benchmark the ECAL performance. The short lifetime scenario ($\tau_{\tilde{\chi}_1^0} = 0.2\,\mathrm{ns}$) tests the limit of the ECAL angular resolution, the medium lifetime case ($\tau_{\tilde{\chi}_1^0} = 2.0\,\mathrm{ns}$) is not so problematic for the detector and serves as a test of the reconstruction principle. Very long-lived neutralinos ($\tau_{\tilde{\chi}_1^0} = 11.0\,\mathrm{ns}$) hit the geometrical ECAL depth limit, as more and more neutralinos tend to decay only within, or even outside of the ECAL.

5.1 Event Simulation

As neither the ILC nor the ILD exist so far, the detector performance is evaluated with a full Monte Carlo simulation. These studies can be used to develop particle identification and reconstruction algorithms well in advance to the actual data taking. Central detector characteristics, e.g. the material, depth or granularity, can be studied to build the best possible detector. Physics studies can be used to substantiate the detector requirements.

Supersymmetry is a possible extension of the Standard Model, that has not yet been discovered. Thus, first of all the particle spectrum under investigation, i.e. the particle masses, branching ratios and decay widths, has to be calculated by a SUSY spectrum generator. Afterwards, the events are generated by a Monte Carlo event generator program. And finally, they are passed to a full detector simulation.

GMSB Parameter	Chosen Value	[unit]
Λ	110	TeV
N_5	1	
M_{mess}	240	TeV
$\tan(\beta)$	3.0	
$\mathrm{sgn}(\mu)$	$+$	
c_{grav}	23.0	

Table 5.1: Basic GMSB model parameters used in the presented analysis.

Particle	Mass [GeV]	Main Decay Process	BR [%]
$\tilde{G}$	$1.46 \cdot 10^{-7}$	stable	
$\tilde{\chi}_1^0$	151.0	$\tilde{\chi}_1^0 \rightarrow \tilde{G}\gamma$	100
$\tilde{\chi}_1^+$	189.6	$\tilde{\chi}_1^+ \rightarrow \tilde{\chi}_1^0 W^+$	97.3
h^0	101.5	$h^0 \rightarrow \bar{b}b$	81.6
$\tilde{e}_R^-$	196.4	$\tilde{e}_R^- \rightarrow \tilde{\chi}_1^0 e^-$	100
$\tilde{\mu}_R^-$	196.4	$\tilde{\mu}_R^- \rightarrow \tilde{\chi}_1^0 \mu^-$	100
$\tilde{\tau}_1^-$	196.1	$\tilde{\tau}_1^- \rightarrow \tilde{\chi}_1^0 \tau^-$	100

Table 5.2: Masses and branching ratios of the kinematically accessible SUSY particles for the GMSB parameters listed in table 5.1.

5.1.1 SUSY Spectrum Generation

The SUSY spectrum is calculated by SPheno, the abbreviation for Supersymmetric Phenomenology [90]. SPheno numerically calculates the SUSY particle spectrum within a given high-scale theory, e. g. GMSB. For a minimal GMSB model, the required input parameters are Λ, N_5, M_{mess}, $\tan\beta$, $\mathrm{sgn}\,\mu$ and c_{grav}. As explained in section 2.3.5, these parameters are sufficient to determine the GMSB scenario. SPheno provides the masses and mixing matrices for the selected model, as well as the decay widths and branching ratios of all resulting SUSY particles and Higgs bosons.

The boundary conditions investigated in this analysis, fulfilling the requirements given in [91], are listed in table 5.1. This parameter set produces a rather light particle spectrum with a neutralino NLSP. The kinematically accessible SUSY particles and their dominating decay channel with corresponding branching ratio (BR) are listed in table 5.2. All SUSY particles decay via the $\tilde{\chi}_1^0$ NLSP into the $\tilde{G}$ LSP. All the decay chains from heavier particles involve charged particles and hadrons. With a tracking efficiency of 99 % they can be well separated from the trackless $\tilde{\chi}_1^0 \rightarrow \tilde{G}\gamma$ decay, and are not further investigated as background contributions.

Searches for the lightest neutral Higgs boson in SUSY models yield $m_{h_0} > 92.8\,\mathrm{GeV}$ at 95 % confidence level [4]. Searches for neutralino decays at D0 and CDF exclude $m_{\tilde{\chi}_1^0} \leq 125\,\mathrm{GeV}$ at 95 % confidence level [4]. Thus, this GMSB scenario is not excluded by any direct search.

The Feynman diagrams for neutralino pair-production at an e^+e^- collider, as well as that for the neutralino decay are given in figure 5.1. As the s-channel contribution is
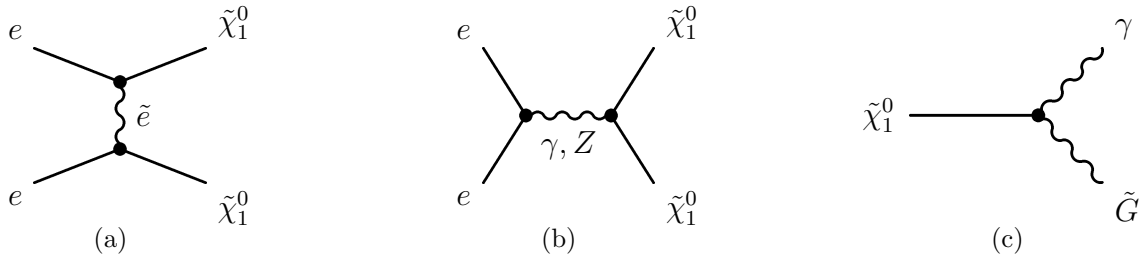
Figure 5.1: Feynman diagram of (a,b) $\tilde{\chi}_1^0$ pair production at a lepton collider and (c) a $\tilde{\chi}_1^0 \to \tilde{G}\gamma$ decay.

a process of weak interaction, it can be enhanced (or suppressed) by polarisation.

Polarisation is a measure for the spin orientation of the particle with respect to its direction of motion. The probability to find the spin parallel to the direction of motion is given by $\mathcal{P}_R$, a particle with this orientation is called right-handed. The probability to find the spin anti-parallel to the direction of motion is given by $\mathcal{P}_L$, a particle with this orientation is called left-handed. The beam polarisation

$$\mathcal{P}_e = \mathcal{P}_R - \mathcal{P}_L \tag{5.1}$$

is defined as the probability to find a randomly picked particle with a certain handedness, with the constraint that

$$\mathcal{P}_R + \mathcal{P}_L = 100\,\%. \tag{5.2}$$

If the beam polarisation is $\mathcal{P}_e = +80\,\%$, the chance to find a right-handed particle is $\mathcal{P}_R = 90\,\%$ and the chance to pick a left-handed particle is $\mathcal{P}_L = 10\,\%$.

Any s-channel cross section at an e^+e^- collider can be written as

$$\sigma = \sigma_0 \left[1 + |\mathcal{P}_{e^-}||\mathcal{P}_{e^+}| + A_{LR}(\mathcal{P}_{e^-}, \mathcal{P}_{e^+})\right], \tag{5.3}$$

where $\mathcal{P}_e$ denotes the beam polarisation and σ_0 is the cross section for unpolarised beams $\mathcal{P}_{e\pm} = 0$. The left-right asymmetry is a measure for the enhancement of the production cross section for different beam configurations:

$$A_{LR} = \frac{\sigma_{LR} - \sigma_{RL}}{\sigma_{LR} + \sigma_{RL}} \cdot \frac{1 - \mathcal{P}_{e^-}\mathcal{P}_{e^+}}{\mathcal{P}_{e^-} - \mathcal{P}_{e^+}}, \tag{5.4}$$

where in the LR configuration $\mathcal{P}_{e^-} < 0$ and $\mathcal{P}_{e^+} > 0$, and vice versa for the RL configuration. For a polarisation of $\mathcal{P}(e^-, e^+) = (+0.8, -0.6)$ the signal can be enhanced to 217,000 events in $\int \mathcal{L}\,dt = 500\,\mathrm{fb}^{-1}$, with respect to 76,000 events without beam polarisation. With 9,306 signal events for $\mathcal{P}(e^-, e^+) = (-0.8, +0.6)$ polarisation, the left-right asymmetry for this constellation is $A_{LR} = -0.92$.

5.1.2 Event Generation

The universal Monte Carlo event generator WHiZard (W, Higgs, Z and respective decays) [92, 93, 94] evaluates distributions of four-vectors, calculates the cross section of each process and generates unweighted event samples. It is interfaced with the

SUSY spectrum calculator and Guinea-Pig [95], a tool for the simulation of beam-beam interactions at e^+e^- colliders. This allows to include beamstrahlung, initial and final state radiation in the event generation.

For the signal sample, $\int \mathcal{L}\, dt = 100\,\mathrm{fb}^{-1}$ of $e^+e^- \rightarrow \tilde{\chi}_1^0 \tilde{\chi}_1^0$ reactions at $\sqrt{s} = 500\,\mathrm{GeV}$ are generated with a polarisation of $\mathcal{P}(e^-, e^+) = (+0.8, -0.6)$. The Standard Model background sample is also generated with WHiZard. Only processes that yield the same detector signature as the signal process are taken into account. These are $e^+e^- \rightarrow \nu_e \bar{\nu}_e \gamma\gamma,\ \nu_\mu \bar{\nu}_\mu \gamma\gamma,\ \nu_\tau \bar{\nu}_\tau \gamma\gamma$ and $e^+e^- \rightarrow \gamma\gamma$ events.

Standard Model processes are only simulated with $\mathcal{P}(e^-, e^+) = (+1.0, -1.0)$ and $\mathcal{P}(e^-, e^+) = (-1.0, +1.0)$. Since

$$\mathcal{P}_R = \frac{1 + \mathcal{P}_e}{2}, \quad \mathcal{P}_L = \frac{1 - \mathcal{P}_e}{2}, \tag{5.5}$$

respectively, the beam polarisation can be calculated from

$$\mathcal{P}_e = 2 \cdot \mathcal{P}_R - 1 = 1 - 2 \cdot \mathcal{P}_L. \tag{5.6}$$

Thus, the desired polarisation of $+80\,\%$ for electrons equals $10\,\%$ left-handed and $90\,\%$ right-handed particles. Accordingly, $-60\,\%$ positron polarisation equals $80\,\%$ left-handed and $20\,\%$ right-handed beam:

$$\begin{aligned}
\mathcal{P}_{e^-} &= +0.8 = -0.9 \cdot \mathcal{P}_R - 0.1 \cdot \mathcal{P}_L, \\
\mathcal{P}_{e^+} &= -0.6 = -0.2 \cdot \mathcal{P}_R - 0.8 \cdot \mathcal{P}_L.
\end{aligned}$$

The final beam polarisation is achieved by mixing

$$\mathcal{P}(e^-, e^+) = (+0.8, -0.6) = 0.9 \cdot \mathcal{P}_R(e^-) \cdot 0.8 \cdot \mathcal{P}_L(e^+) = 0.72 \cdot \mathcal{P}(+1.0, -1.0) \tag{5.7}$$

of the $\mathcal{P}(e^-, e^+) = (+1.0, -1.0)$ sample with

$$\mathcal{P}(e^-, e^+) = (+0.8, -0.6) = 0.1 \cdot \mathcal{P}_L(e^-) \cdot 0.2 \cdot \mathcal{P}_R(e^+) = 0.02 \cdot \mathcal{P}(-1.0, +1.0) \tag{5.8}$$

of the $\mathcal{P}(e^-, e^+) = (-1.0, +1.0)$ sample.

Particles in the very forward region, that escape through the beam pipe, and low-energetic particles are computing intensive, but do not contribute to the detector signal. Therefore, the following kinematic acceptance cuts are applied [96]:

- a $10\,\mathrm{GeV}$ jet cut for the minimum invariant mass of a pair of coloured particles,

- a $4\,\mathrm{GeV}$ mass cut for the minimum invariant mass of a pair of colourless particles,

- a $4\,\mathrm{GeV}$ cut for the minimum invariant mass of the exchange particle in t-channel processes.

Finally, the fragmentation of quarks is performed by the PYTHIA [97] event generator. Unlike WHiZard, PYTHIA includes the gravitino and thus, it also takes care of the decay of the neutralinos.

5.1.3 Event Simulation

For signal and background, the detector simulation is realised with Mokka [98], a detailed simulation based on Geant4 (GEometry ANd Tracking) [99]. Geant4 is used to simulate the passage of particles through matter. It can handle Standard Model particle interactions with the detector material, including energy loss, as well as interactions with the magnetic field. However, Geant4 is not aware of SUSY particles. To enable the correct handling of neutralino decays, the neutralino and the gravitino are added to the G4ParticleList. Although they are not expected to interact with the detector material, nor the magnetic field, their mass, charge, decay width and channel, and lifetime still have to be introduced to Geant4, to track them through the detector.

The chosen GMSB parameters result in a lifetime of $\tau_{\tilde{\chi}_1^0} = 0.203\,\mathrm{ns}$. As the aim of this study is to test the lifetime reconstruction capabilities of the electromagnetic calorimeter, the neutralino lifetime is artificially enhanced in Geant4 to obtain three samples of $0.203\,\mathrm{ns}$, $2.029\,\mathrm{ns}$, and $11.029\,\mathrm{ns}$ lifetime, respectively. For a neutralino mass of $151.1\,\mathrm{GeV}$, and a neutralino energy of $250.0\,\mathrm{GeV}$, this corresponds to a mean decay distance of approximately $11\,\mathrm{cm}$, $80\,\mathrm{cm}$, and $450\,\mathrm{cm}$ in the detector, respectively. Each sample is generated with roughly 21000 events.

The presented results are obtained for the ILD detector described in section 3.3.3. For a realistic detector performance study, the description of the geometry of each sub-detector is very detailed, including dead regions and support structures. The detector geometry and event topology, are displayed in figure 5.2. Two neutralinos are produced at the IP. They travel into the main tracker before decaying into a neutral gravitino and a photon each. The secondary vertices are clearly visible. The photons shower in the electromagnetic calorimeter, that is surrounded by a hadron calorimeter.

5.2 Event Reconstruction

The event reconstruction is based on Marlin (Modular Analysis and Reconstruction for the LINear collider) [100]. The most important objects for this analysis are photons. Their reconstruction is based on a fast and efficient photon-finder-kit [77], which is explained in some detail in the following. The reconstruction of other objects, e. g. tracks or jets, is not relevant for this study and therefore not further covered. More details on event reconstruction with Marlin are given in [101].

5.2.1 Photon Reconstruction

The basic idea of the photon reconstruction algorithm is to utilise the imaging capabilities of the calorimeter to extract the energy density profile of the shower. It integrates the average energy density, as defined in 4.16, over the n ECAL layers and rings around the shower starting point. This method is repeated for a distinct number of energy thresholds, which allows to identify the number of photons, to separate close-by photons and to estimate the photon energy and direction.

Due to the intrinsic shower fluctuations and the limited detector cell size, the ideal distribution gets smeared. However, within a highly granular calorimeter, as proposed for the ILD, these fluctuations stay small and the method is still applicable.
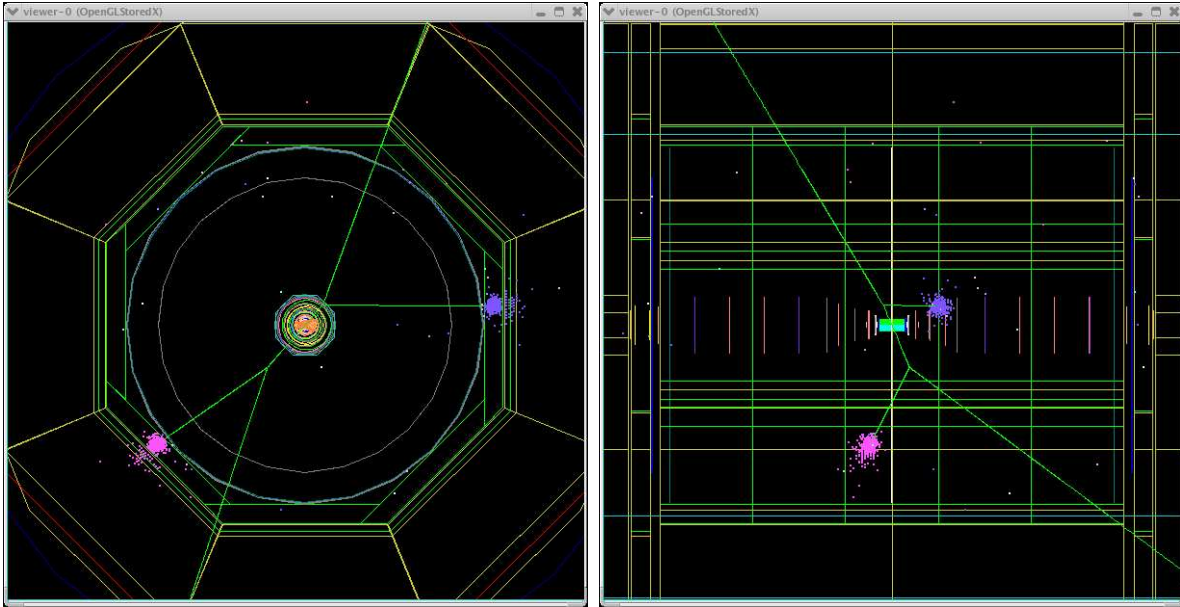
(a)   (b)

Figure 5.2: Event display of an $e^+e^- \to \tilde{\chi}_1^0 \tilde{\chi}_1^0 \to \tilde{G}\gamma\tilde{G}\gamma$ event in Mokka (a) in r-ϕ view
(b) in r-z view. The blue circle represents the TPC, the green octagon the
ECAL and the yellow octagon the HCAL. See text for further explanations.

Since electromagnetic showers are rather compact objects without discontinuities, a
nearest-neighbour cluster algorithm is suitable to reconstruct the shower. To simplify
the cluster-building, isolated calorimeter hits with less than $N_{\mathrm{neighbours}}$ neighbouring
cells being hit are ignored during all further cluster building steps until the final photon
building. This helps to smoothen the shower surface, and thus suppresses the natural
fluctuations. However, it also induces problems with low-energetic photons ($E_\gamma \leq$
$1\,\mathrm{GeV}$), that have a shower radius comparable with the cell size. Since the photon
energies in the studied scenario are expected to range between several tens and several
hundred GeV, this is negligible.

To identify the dense core of an electromagnetic shower, the selected ECAL hits are
assigned into N_{samples} sub-samples according to the hit energy E_{hit} and some threshold
levels $E_{\mathrm{threshold}}$. To allow good close-by shower separation, the threshold levels are
closer for lower hit energies. All clusters with more than N_{hits} hits are regarded photon
candidates.

The decision to split or merge close-by clusters is based on a pattern recognition algo-
rithm. A cone with opening angle $\alpha(C_1, C_2)$ is constructed from the centre and along
the assumed direction of one of the cluster candidates. If the second cluster candidate
lies within this cone, at a distance not larger than $D(C_1, C_2)$, the clusters are merged,
otherwise they are split.

The cluster building parameters are free steering parameters, that have to be adopted
to the expected physics signature. The separation criteria used in this analysis are
listed in table 5.3. They are chosen to contain the maximal fraction of the full energy,
which is important to get a good energy estimation, as described in the following.

Cluster Parameter		Chosen Value	[unit]
$N_{\text{neighbours}}$	$>$	4	hits
N_{samples}	$=$	10	
$E_{\text{threshold}}$	$=$	0.1, 1.5, 2.5, 4, 6 9, 16, 26, 41, 65	MIP/hit
$N_{\text{hits}}(C)$	$>$	8	hits/cluster
$\cos\alpha(C_1, C_2)$	$>$	0.95	
$D(C_1, C_2)$	$<$	3.0	cm

Table 5.3: Photon reconstruction parameters used in this analysis. Further explanations are given in the text.

5.2.2 Energy Estimation

All clusters passing the selection criteria are considered photon candidates. For each of them the energy is estimated from the measured energy, and the threshold-level of the sub-sample. This gives a handle to collect all hits belonging to the photon, also distant and isolated ones that have been excluded so far. Thus, it improves the energy reconstruction and provides a more accurate shower shape reconstruction.

The energy estimation requires the prior knowledge of the true energy deposition for the given detector configuration and cluster building parameter set under investigation. Thus, single photons at various energies are simulated and passed through the reconstruction scheme described above. The true energy deposition at each sub-sample is stored, and compared to the reconstructed one. As illustrated in figure 5.3, where the true energy and the reconstructed energy of 20 GeV photons with at least 1.5 MIP per hit are plotted, a linear fit is suitable to parametrise the relation between true and reconstructed energy deposition:

$$E_{\text{true}} = a + cE_{\text{reco}}. \tag{5.9}$$

Fifteen samples with single photons with energies between 0.5 GeV and 200 GeV, with 1000 events each, are used to create a calibration table for the given detector and algorithm parameter conditions. The energy for any incoming photon is then estimated from a threshold dependent energy calibration.

Finally, photons are reconstructed on the basis of a 3 dimensional model, using the estimated energy, the shower direction (cf. equation 4.20) and its starting point. The full energy density distribution, given in equation 4.16, is used to estimate the probability that a given hit belongs to one cluster or another.

5.2.3 Cluster Algorithm Performance

The clustering performance is tested with the simulation of single photons with energies ranging from 1 GeV to 200 GeV. The particle gun is positioned directly in front of the ECAL surface, to avoid multiple scattering, energy-losses and pair-production in the tracking volume. The incident angle between the photons and the ECAL surface is varied between 90° and 40° in ϕ and θ.
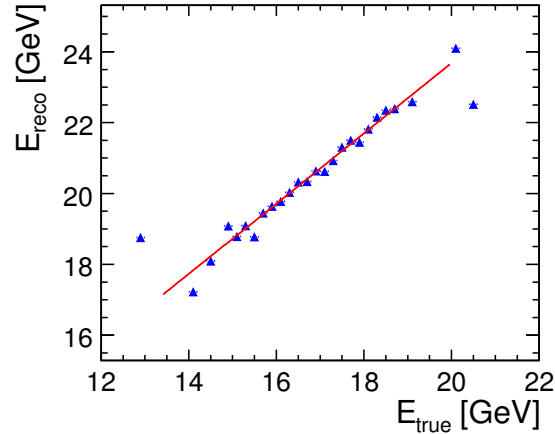
Figure 5.3: Calibration of the reconstructed photon energy, depending on the energy-per-hit threshold, for a 20 GeV photon with at least 1.5 MIP per hit.

Cluster Efficiency   As shown in figure 5.4(a), the efficiency to find exactly one photon, if one photon is shot into the detector is more than 88 % for photon energies between 1 GeV and 200 GeV at any incidence angle. The efficiency for perpendicular photons can be taken as a measure for the calibration uncertainty. It is above 99.5 % for photon energies between 5 GeV and 70 GeV. At smaller energies some photons are lost, since they do not produce enough hits and thus do not pass the $N_{\text{hits}}(C)$ requirement. At higher energies, the cluster processor tends to split clusters, which degrades the efficiency to 97 % for 250 GeV photons. This can in principle be improved by loosening the $\cos\alpha(C_1, C_2)$ and the $D(C_1, C_2)$ requirement, but this would in turn lead to a degradation in particle separation.

Energy Reconstruction   The deviation between true and reconstructed photon energy is defined as $(E_{\text{reco}} - E_{\text{true}})/E_{\text{true}}$. It is smaller than 5 % for all investigated energies and incidence angles, as shown in figure 5.4(b). The deviation gets larger with decreasing incidence angle. The deviation for photons perpendicular to the ECAL surface, a measure for the quality of the calibration method, is below 2 %. Photons at 40° incidence angle deviate up to 4 %.

The energy resolution is shown in figure 5.5. For perpendicular incidence, it can be parametrised as:

$$\frac{\sigma_E}{E} = \frac{(16.7 \pm 0.3)\,\%}{\sqrt{E[\text{GeV}]}} \oplus (0.61 \pm 0.08)\,\%. \tag{5.10}$$

This is comparable with the energy resolution of $\sigma_E/E = 16.5\,\% \oplus 1.07\,\%$, measured with the CALICE Si-W ECAL [63]. It slightly degrades down to $(18.6 \pm 0.3)\,\%/\sqrt{E} \oplus (0.62 \pm 0.09)\,\%$ for photons at 40° angle. The cluster efficiency, energy linearity and energy resolution influence the reconstructed photon energy, and thus have influence on the $\tilde{\chi}_1^0$ mass determination.
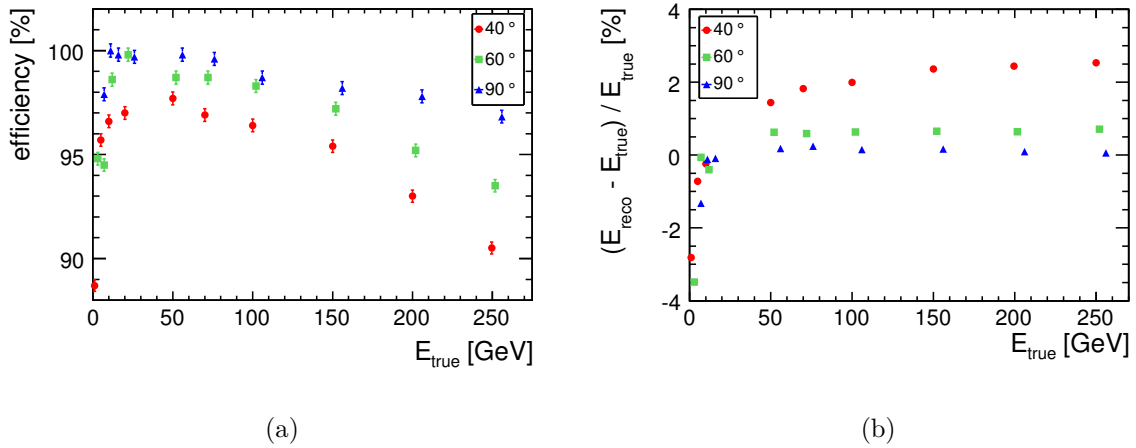
Figure 5.4: (a) Single-photon clustering efficiency of the photon reconstruction algorithm for $\Phi = 40°$ (circle), $60°$ (squares) and $90°$ (triangles). (b) Deviation of reconstructed from true photon energy. For better visibility, the data points are slightly shifted on the x-axis.
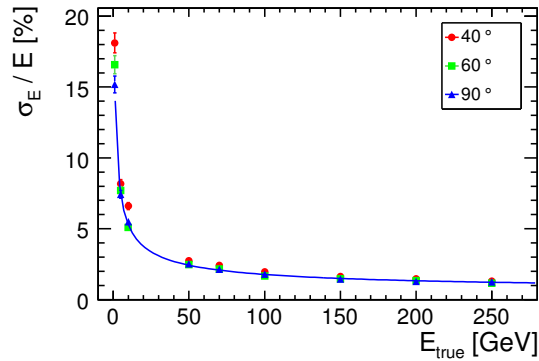

Figure 5.5: Energy resolution of the ECAL barrel for $\Phi = 40°$ (circle), $60°$ (squares) and $90°$ (triangles). The red line indicates the fit to photons perpendicular to the ECAL surface ($\Phi = 90°$).

Angular Reconstruction The angular orientation of the cluster can be calculated from the cluster principal axes (cf. equation 4.20), according to

$$\phi = \arctan \frac{y}{x}, \tag{5.11}$$

$$\theta = \arccos z. \tag{5.12}$$

The deviation from reconstructed to true incidence angle is plotted in figure 5.6(a) for $\Delta\phi(\phi)$ as a function of incidence angle, and in figure 5.6(b) for $\Delta\theta(E)$ as a function of photon energy. The interchanged plots, $\Delta\theta(\theta)$ and $\Delta\phi(E)$, are not shown, as they behave similar.

The deviation, in θ as well as in ϕ, is below 1% for particles at $90°$ incidence angle and up to 6% at $40°$ incidence angle. At energies above $20\,\mathrm{GeV}$, which are relevant for the

(a)   (b)
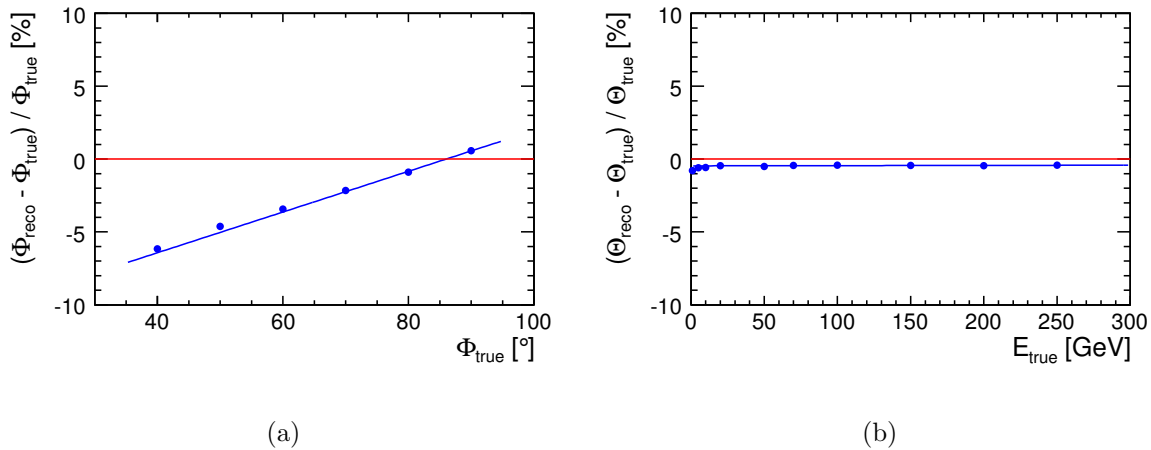
Figure 5.6: Deviation of reconstructed from true particle angle (a) in ϕ as a function of incidence angle and (b) in θ as a function of photon energy.

presented analysis, the deviation between reconstructed and true angle is independent of the energy of the particle. The angular resolution for particles at 90° incidence angle, plotted in figure 5.7(a), is determined to be

$$\sigma_\theta = \frac{(131 \pm 2)\,\mathrm{mrad}}{\sqrt{E\,[\mathrm{GeV}]}} \oplus (3.7 \pm 0.5)\,\mathrm{mrad}. \tag{5.13}$$

This is worse than the angular resolution of $\sigma_\theta = 106\,\mathrm{mrad}/\sqrt{E\,[\mathrm{GeV}]} \oplus 4\,\mathrm{mrad}$, measured with the CALICE Si-W ECAL [102]. As the cell size of the ECAL prototype is larger than that of the ILD calorimeter, the worse angular resolution in the presented analysis hints towards problems in the photon finder algorithm.

The angular reconstruction influences the $\tilde{\chi}_1^0$ lifetime reconstruction. As shown in section 5.4.2, the deviation between true and reconstructed angle has a direct impact on the decay spectra.

Position Reconstruction   The cluster position is determined from its centre-of-gravity $\langle \vec{x} \rangle$ (cf. equation 4.17). The position resolution at 90° incidence angle, as plotted in figure 5.7(b), can be parametrised as

$$\sigma_{\langle \vec{x} \rangle} = \frac{(2.7 \pm 0.2)\,\mathrm{mm}}{\sqrt{E\,[\mathrm{GeV}]}} + (2.80 \pm 0.03)\,\mathrm{mm}. \tag{5.14}$$

The Si-W ECAL measures a position resolution of [102]

$$\sigma_x = 14.8\,\mathrm{mm}/E\,[\mathrm{GeV}] \oplus 3.9/\sqrt{E\,[\mathrm{GeV}]} \oplus 1.04\,\mathrm{mm}.$$

The high noise-term contribution is a result of the track-reconstruction based on drift chambers. At low energies their track resolution is worse than the Si-W ECAL resolution. For energies above 6 GeV, the Si-W ECAL position resolution is much better than the presented resolution of ILD, which is another hint for problems in the photon finder algorithm. An S-curve calibration, which corrects for the cell structure of the ECAL could improve the resolution.
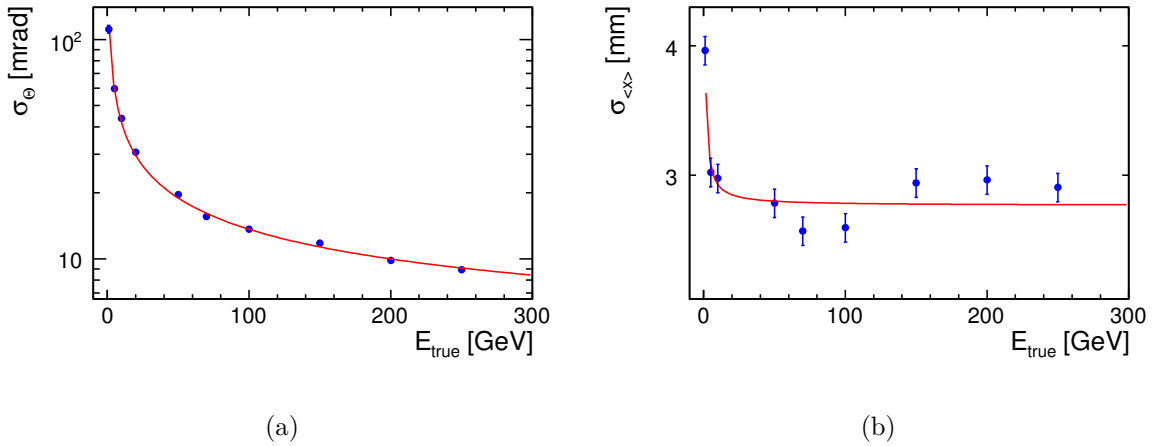
Figure 5.7: (a) Angular and (b) position resolution of the ECAL barrel as a function of photon energy.

5.3 Signal Selection

At the ILC $\int \mathcal{L} \, dt = 500 \, \text{fb}^{-1}$ integrated luminosity at $\sqrt{s} = 500 \, \text{GeV}$ with a polarisation of $\mathcal{P}(e^-, e^+) = (-0.8, +0.6)$, correspond to 217,000 signal events. In addition, there will be at least

- 2,000,000 $\nu_e \bar{\nu}_e \gamma\gamma$ events

- 70,000 $\nu_\mu \bar{\nu}_\mu \gamma\gamma$ events

- 71,000 $\nu_\tau \bar{\nu}_\tau \gamma\gamma$ events

- 3,110,000 $\gamma\, \gamma$ events

Those sum up to at least $5.3 \cdot 10^6$ background events, corresponding to a signal-to-background ratio of $S : B \approx 1 : 24.3$.

The physics signature in the electromagnetic calorimeter is utilised to separate signal from background events. Figure 5.8 and figure 5.9 show the distributions on which the selection is based, before all cuts for the signal process with $\tau_{\tilde{\chi}_1^0} = 2.0 \, \text{ns}$, background processes and combined data. The vertical red lines indicate the chosen cut and the arrow point towards the accepted region.

The major part of the Standard Model events is rejected by applying the following selection to all events in the SUSY and SM samples:

- some activity in the ECAL with $1500 \leq N_{\text{hits}}(\text{ECAL}) \leq 6000$ and $80 \, \text{GeV} \leq E_{\text{sum}}(\text{ECAL}) \leq 450 \, \text{GeV}$;

- at least two reconstructed photons ($N_\gamma \geq 2$) with $E_\gamma \geq 20 \, \text{GeV}$ and $|\cos(\theta_\gamma)| \leq 0.75$;

- $\not{E}_t(\text{ECAL}) \geq 30 \, \text{GeV}$ missing transverse energy in the ECAL from the $\tilde{G}$.
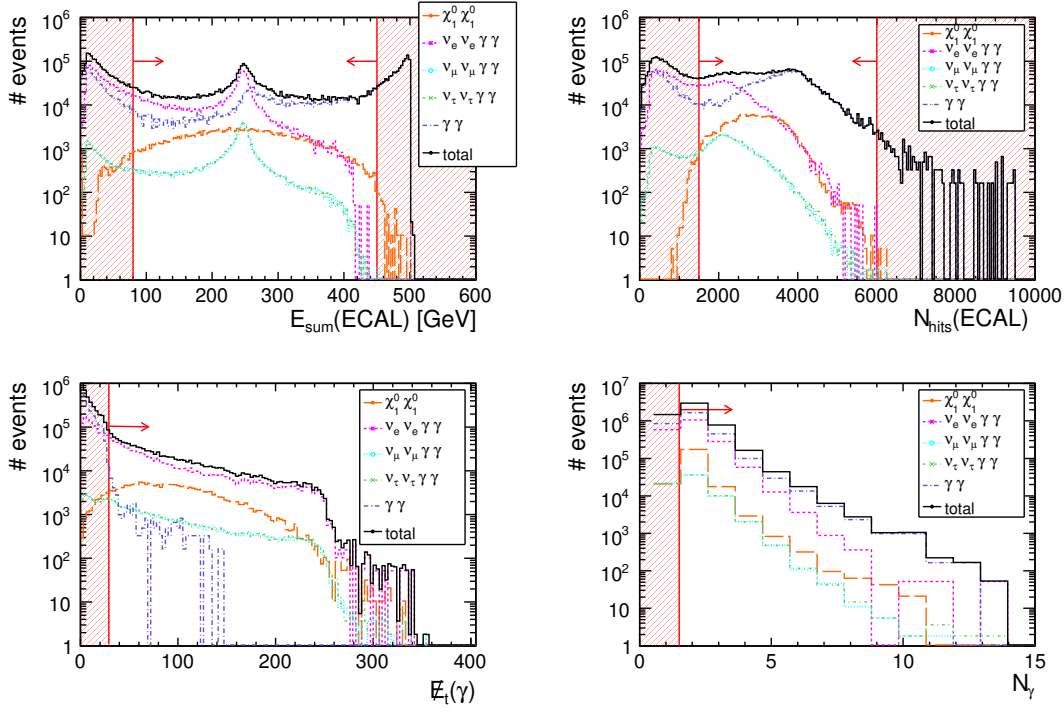
Figure 5.8: Energy sum (upper-left plot) and number of hits (upper-right plot) distributions in the ECAL, as well as missing transverse energy per event (lower-left plot) and number of reconstructed photons (lower-right plot) for signal events with $\tau_{\tilde{\chi}_1^0} = 2.0$ ns (orange hashed region) and background events. All distributions are shown before any selection cut is applied. The red arrows point towards the accepted region, the red hashed area indicates the excluded region.
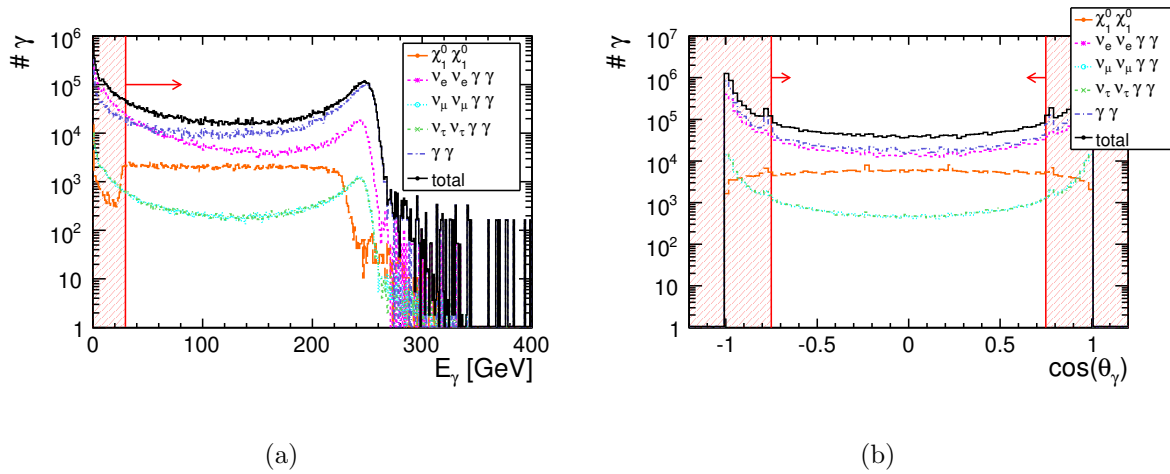

(a)   (b)

Figure 5.9: (a) Photon energy and (b) $|\cos\theta|$ distribution for signal (orange hashed region) and background without any selection cuts applied. All distributions for signal events with $\tau_{\tilde{\chi}_1^0} = 2.0$ ns. The red arrows point towards the accepted region, the red hashed area indicates the excluded region.

$\tau_{\tilde{\chi}_1^0}$ [ns]	Signal : Background
0.2	3.9 : 1
2.0	3.5 : 1
11.0	1 : 1.5

Table 5.4: Signal-to-background ratio after all selection cuts for the three investigated neutralino lifetime samples.

	Signal Process			Background Process			
	$\tau_{\tilde{\chi}_1^0} = 0.2\,\text{ns}$	$\tau_{\tilde{\chi}_1^0} = 2.0\,\text{ns}$	$\tau_{\tilde{\chi}_1^0} = 11.0\,\text{ns}$	$\nu_e \nu_e \gamma\gamma$	$\nu_\mu \nu_\mu \gamma\gamma$	$\nu_\tau \nu_\tau \gamma\gamma$	$\gamma\gamma$
E_{sum}	99.1 %	95.7 %	52.5 %	53.4 %	78.2 %	78.6 %	40.6 %
N_{hits}	98.7 %	93.0 %	40.8 %	45.2 %	70.9 %	71.2 %	69.9 %
$\not{E}_t$	92.3 %	91.1 %	60.3 %	46.6 %	66.8 %	67.3 %	1.0 %
N_γ	99.6 %	90.1 %	22.0 %	70.8 %	69.4 %	69.4 %	73.0 %
E_γ	99.1 %	89.0 %	18.9 %	20.1 %	28.4 %	28.2 %	28.3 %
$|\cos\theta_\gamma|$	62.7 %	60.2 %	13.9 %	6.8 %	6.4 %	6.5 %	9.3 %
all	59.5 %	53.7 %	10.2 %	1.4 %	2.3 %	2.3 %	0.04 %

Table 5.5: Relative amount of events surviving each single cut and all cuts together.

Requiring all of the above criteria reduces the background to 0.6 % of the original amount, while leaving 59.5 % of the signal with $\tau_{\tilde{\chi}_1^0} = 0.2\,\text{ns}$, 53.7 % of the $\tau_{\tilde{\chi}_1^0} = 2.0\,\text{ns}$ sample and 10.2 % of the $\tau_{\tilde{\chi}_1^0} = 11.0\,\text{ns}$ signal sample, respectively. The selection efficiency decreases for the long-lived neutralino sample, mainly because the clustering algorithm tends to split photon showers resulting from long-lived neutralinos.

The corresponding signal-to-background ratios are listed in table 5.4. Table 5.5 gives a more detailed overview of the effect of each single cut on the different types of background and signal. Quoted is the fraction of selected events applying one cut at a time, and all cuts at once. For example, 92.3 % of all signal events emerging from neutralino decays with $\tau_{\tilde{\chi}_1^0} = 0.2\,\text{ns}$ have missing transverse energy $\not{E}_t \geq 30\,\text{GeV}$, while this requirement is only fulfilled by 1.0 % of all $e^+e^- \to \gamma\gamma$ events.

The selection efficiency decreases with increasing neutralino lifetime, thus also the signal-to-background ratio decreases with increasing neutralino lifetime. The clustering algorithm tends to split photon showers resulting from long-lived neutralinos. This significantly reduces the signal selection efficiency to one fifth. Furthermore, samples with longer lifetimes are more sensitive to cuts on the required ECAL energy and number of hits. This is illustrated in figure 5.10, which shows the energy sum in the HCAL, the number of hits in the ECAL and the number of reconstructed photons per event for all three lifetime scenarios. Obviously, the signal contribution in the ECAL decreases with increasing neutralino lifetime, while the signal contribution in the HCAL, which is not included in the photon reconstruction, increases. Longer-lived neutralinos partially decay within, or even outside of the electromagnetic calorimeter. In principle the selection cuts could be individually adjusted for each lifetime scenario, but as the neutralino lifetime is not a priori known and to keep results comparable,
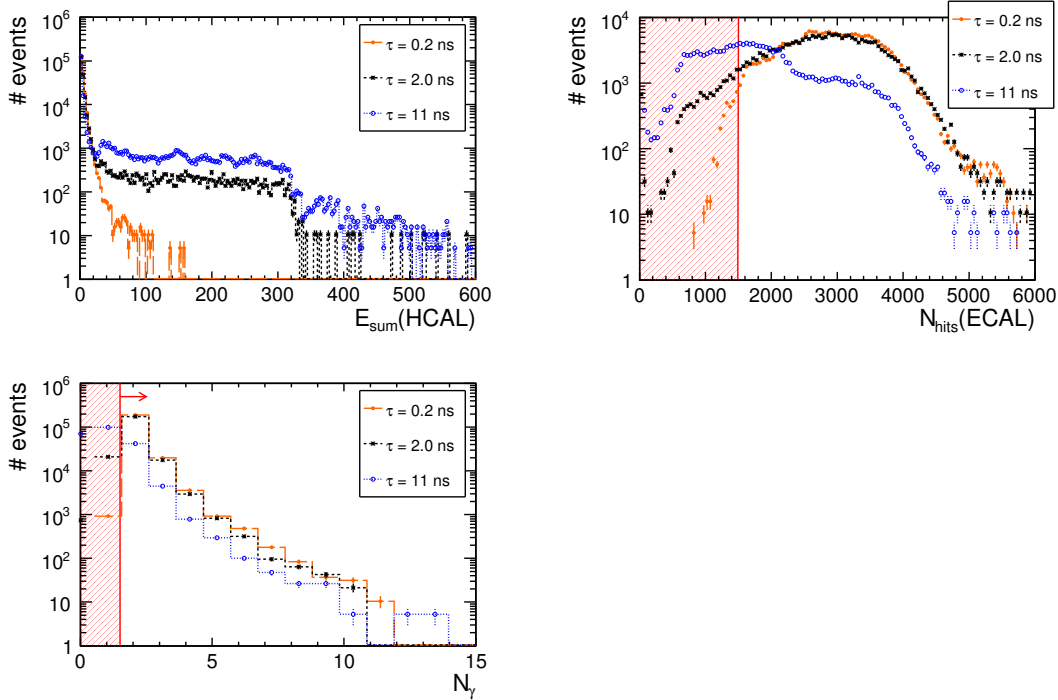
Figure 5.10: Long-lived neutralinos may decay late in the ECAL, resulting in a shower leaking to the HCAL: energy sum per event in the HCAL (upper-left plot) number of hits per event in the ECAL (upper-right plot) and number of reconstructed photons per event (lower-right plot) for neutralinos with 0.2 ns (black dotted line), 2.0 ns (blue dash-dotted line) and 11.0 ns (red solid line), respectively.

this is not done for the presented analysis.

The signal cross section is defined as:

$$\sigma = \frac{N_{\text{signal}}}{\varepsilon \cdot \mathcal{L}}. \tag{5.15}$$

For an integrated luminosity of $\int \mathcal{L}\, dt = 500\,\text{fb}^{-1}$ and $N_{\text{signal}} = N_{\text{generated}} \cdot \varepsilon$ selected signal events, given the selection efficiency ε as stated in table 5.5, this results in $\sigma = 433.5\,\text{fb}$.

5.4 Measurement of $\tilde{\chi}_1^0$ properties

The signal-to-background ratio achieved with the simple cut-based selection method described above, enables the discovery of the short and medium lifetime neutralino. The number of two-photon events, as displayed in figure 5.11, is much higher than the one expected from Standard Model background events. For the short-lived scenario, figure 5.11(a), the distribution is strongly dominated by signal events. However, for long-lived neutralinos, figure 5.11(b), the number of two-photon events is just 1 % above the expectation from the Standard Model background. Thus, the HCAL has to be included in the reconstruction to improve the photon reconstruction in this scenario.
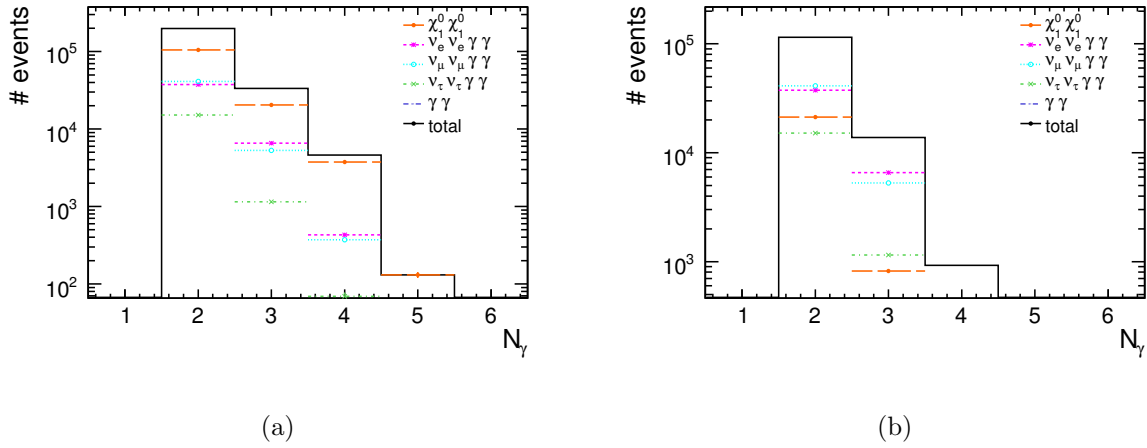
Figure 5.11: Number of reconstructed photons per event after all selection cuts for (a) neutralinos with $\tau_{\tilde{\chi}_1^0} = 0.2\,\text{ns}$ and (b)$\tau_{\tilde{\chi}_1^0} = 11\,\text{ns}$ lifetime and background events.

Once a signature that hints toward physics beyond the Standard Model is established, measurements of the properties of the new particles can be used to constrain the underlying model. As discussed in section 2.3.5, in GMSB models the fundamental SUSY breaking scale can be determined from the NLSP mass and lifetime. Methods to determine the NLSP particle mass from a kinematic edge fit, and the NLSP lifetime, exploring the excellent spatial ECAL granularity, are discussed in the following.

5.4.1 Measurement of the $\tilde{\chi}_1^0$ mass

The $\tilde{\chi}_1^0$ mass can be obtained from the energy spectrum of the photon candidates, since for a two-body decay, assuming effectively massless decay products, the distribution is box-like with edges determined by the neutralino mass $m_{\tilde{\chi}_1^0}$ and the centre-of-mass energy $\sqrt{s}$. Deviations from the pure box shape are due to the beam energy spectrum and the detector resolution. The relation between the $\tilde{\chi}_1^0$ mass and the energy endpoints of the photon is determined by pure kinematics [103]:

$$E_{\text{min,max}}^{\gamma} = \frac{1}{4}\left(\sqrt{s} \mp \sqrt{s - 4m_{\tilde{\chi}_1^0}^2}\right). \tag{5.16}$$

Thus, the neutralino mass can be extracted from a fit to the edges of the photon energy spectrum:

$$m_{\tilde{\chi}_1^0} = \frac{1}{2}\sqrt{s \mp (4 \cdot E_{\text{min,max}}^{\gamma} - \sqrt{s})^2}. \tag{5.17}$$

The lower edge can be smeared out by, e. g. SM background processes with soft photons, whereas the upper edge always comes from decays of directly pair-produced neutralinos.

Figure 5.12(a) displays the photon energy distribution for signal only events without any selection cuts. The upper edge is fitted with:

$$E_{\gamma}(A, m_{\tilde{\chi}_1^0}^2, S, B) = A/\left(1 + \exp\left[\frac{E + \frac{1}{4}\left(\sqrt{s} + \sqrt{s - 4m_{\tilde{\chi}_1^0}^2}\right)}{S}\right]\right) + B, \tag{5.18}$$

(a)   (b)
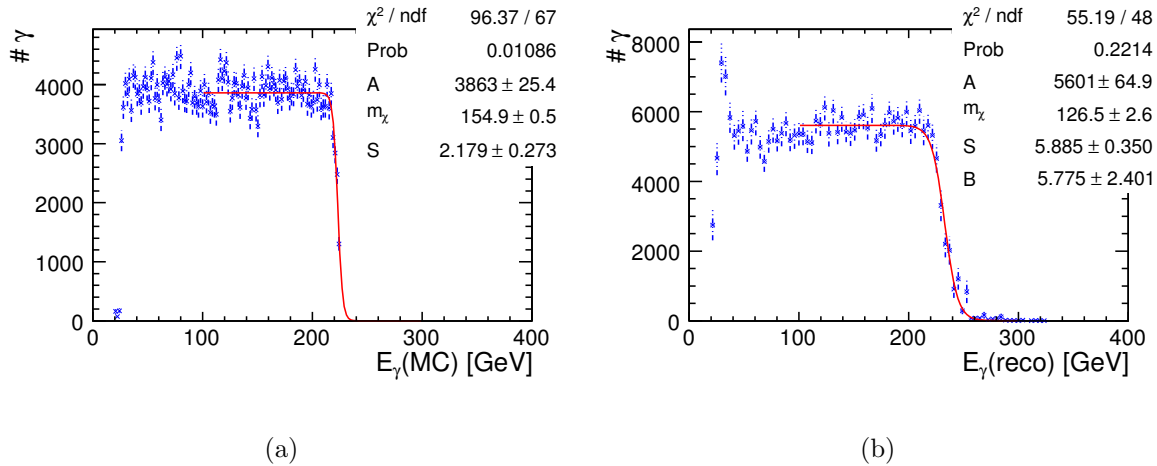
Figure 5.12: $\tilde{\chi}_1^0$ mass determination from photon energy distribution from neutralinos
          with 2.0 ns lifetime after reconstruction. Plotted are (a) signal only events
          without any cuts and (b) reconstructed data (signal + background) events
          after all selection cuts.

	Before Cuts	After Cuts
m_{signal}	$154.9 \pm 0.5\,\text{GeV}$	$148.5 \pm 1.7\,\text{GeV}$
m_{data}	$144.9 \pm 0.8\,\text{GeV}$	$126.5 \pm 2.6\,\text{GeV}$

Table 5.6: $\tilde{\chi}_1^0$ mass as reconstructed from the photon energy distribution from data m_{data}
         and signal only events m_{signal}.

indicated by the red line in figure 5.12. The amplitude A, slope S, background B and
$\tilde{\chi}_1^0$ mass $m_{\tilde{\chi}_1^0}$ are free fitting parameters. The background parameter is set to zero for
the fit to the signal-only sample.

Figure 5.12(a) displays the reconstructed photon energy for signal only events without
any selection cuts applied, while figure 5.12(b) displays the reconstructed photon energy
for signal and background events after all selection cuts. The $\tilde{\chi}_1^0$ mass obtained for the
reconstructed photon energy of the data sample m_{data}, and the photon energy using
only signal events m_{signal}, are listed in table 5.6 for events with and without selection
cuts applied, including their statistical uncertainties.

The $\tilde{\chi}_1^0$ mass estimation using signal only events is higher than the true $\tilde{\chi}_1^0$ mass of
$m_{\text{true}} = 151.0\,\text{GeV}$. This is understandable, since beamstrahlung and initial state radia-
tion have been simulated, but were not accounted for during the $\tilde{\chi}_1^0$ mass reconstruction.
If the true centre-of-mass energy is not $\sqrt{s} = 500\,\text{GeV}$ but only $\sqrt{s} = 497.5\,\text{GeV}$, the
reconstructed $\tilde{\chi}_1^0$ mass yields $m_{\text{signal}} = (151.3 \pm 0.6)\,\text{GeV}$. Thus, it is assumed that this
mass reconstruction method is in principle correct.

On the other hand, the reconstructed mass underestimates the true $\tilde{\chi}_1^0$ mass, be-
cause as shown in figure 5.4(b) the photon energy tends to be overestimated for non-
perpendicular photons. This can be cured by improving the clustering algorithm, or
by re-calibrating the energy measurement with Monte Carlo truth information.

5.4.2 Measurement of the $\tilde{\chi}_1^0$ lifetime

Reconstruction Principle   The $\tilde{\chi}_1^0$ lifetime reconstruction principle is based on simple geometrical constraints, sketched in figure 5.13, and kinematic considerations. The $\tilde{\chi}_1^0$ energy and absolute momentum are constrained by the parameters of the colliding beams and the $\tilde{\chi}_1^0$ mass:

$$E_{\tilde{\chi}_1^0} = E_{\text{beam}}, \quad p_{\tilde{\chi}_1^0} = \sqrt{E_{\tilde{\chi}_1^0} - m_{\tilde{\chi}_1^0}}. \tag{5.19}$$

Thus, the decay angle Δ between $\tilde{\chi}_1^0$ and γ can be determined from the measured photon energy E_γ and kinematic considerations [103]:

$$\cos \Delta = \frac{E_{\tilde{\chi}_1^0}}{p_{\tilde{\chi}_1^0}} - \frac{m_{\tilde{\chi}_1^0}^2}{2 \cdot p_{\tilde{\chi}_1^0} E_\gamma}. \tag{5.20}$$

The resulting $\tilde{\chi}_1^0$ decay length is:

$$\lambda = |\langle \vec{x} \rangle| \cdot \frac{\sin \Psi}{\sin \Delta}, \tag{5.21}$$

where Ψ is the angle between the line connecting the centre-of-gravity of the photon shower with the interaction point $\langle \vec{x} \rangle$ and the principal axis of inertia $\vec{EV}$. The explicit occurrence of the neutralino mass emphasises the importance of an accurate photon energy measurement, as described in section 5.4.1. For the lifetime analysis the neutralino mass is taken from the SUSY spectrum calculator, and not from the reconstruction sketched in section 5.4.1.

In principle there are two neutralinos in each event, which fly back-to-back with an acollinearity angle depending on the initial state radiation and beamstrahlung. This information could be used to constrain the event reconstruction, but it requires a detailed knowledge of the acollinearity angle distribution. Furthermore, it can not be applied to events in which one neutralino is decaying outside of the detector volume. Thus, this analysis treats each neutralino individually.

Neutralinos with an energy of $E_{\tilde{\chi}_1^0} = \sqrt{s}/2 = 250\,\text{GeV}$, and a mass of $m_{\tilde{\chi}_1^0} = 151\,\text{GeV}$, that travel for a time $t_{\tilde{\chi}_1^0}$ cover a distance

$$d_{\tilde{\chi}_1^0} = \frac{c}{t_{\tilde{\chi}_1^0}\sqrt{\dfrac{E_{\tilde{\chi}_1^0}^2}{m_{\tilde{\chi}_1^0}^2} - 1}}. \tag{5.22}$$

Just as the neutralino decay time, the decay length follows an exponential distribution. Individual neutralinos with a decay time shorter than $4.6\,\text{ns}$ decay in front of the ECAL barrel, which has an inner radius of $R_{\text{inner}}(\text{ECAL}) = 185\,\text{cm}$. These events can be reconstructed with the presented algorithm, and hence the lifetime fit is constrained to decay times smaller than $4.6\,\text{ns}$. On the other hand, neutralinos that live longer than $5.1\,\text{ns}$, only decay outside of the ECAL barrel, which has an outer radius of $R_{\text{outer}}(\text{ECAL}) = 202\,\text{cm}$. These events can in principle be recovered, if the analysis is extended to the HCAL.
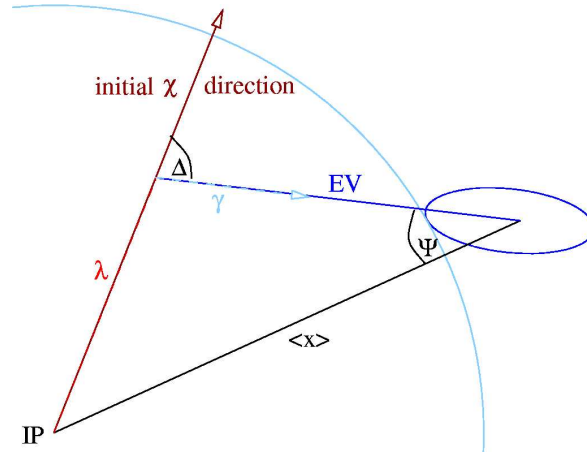
Figure 5.13: Reconstruction principle of the neutralino flight distance (λ). The line connecting the centre-of-gravity from the photon shower with the interaction point ($\langle \vec{x} \rangle$), main axis of inertia (EV), and the angle in between (Ψ) can be measured. The angle between photon and neutralino (Δ) is given by kinematic constraints.

Lifetime Reconstruction using Signal-only Samples   The pure neutralino decay spectra without any selection cuts applied are shown in figure 5.14. They follow an exponential distribution convoluted with the Gaussian shaped detector resolution. The slope, which is a measure for the neutralino lifetime, gets shallower with increasing decay time. The long-lived sample ($\tau_{\tilde{\chi}_1^0} = 11.0\,\mathrm{ns}$), shows the effect of longitudinal leakage. Although most neutralinos decay in front of the electromagnetic calorimeter ($t_{\tilde{\chi}_1^0} \leq 4.6\,\mathrm{ns}$), some also decay within, or even behind the ECAL. The transition of events decaying within the ECAL is visible as sharp drop in the number of reconstructed events. The reconstruction efficiency gets worse with increasing neutralino decay time. Finally, neutralinos that decay only at the rear of the ECAL, or even beyond, cannot be reconstructed at all in the presented analysis.

The neutralino lifetime τ is extracted from a decay model fit, as it is implemented in RooFit [104]:

$$f(t) = \exp\left[\frac{-t}{\tau}\right] \otimes \frac{1}{\sigma\sqrt{2\pi}} \exp\left[-\frac{t'^2}{2}\right]. \tag{5.23}$$

The Gaussian parameter

$$t' = \frac{t - \mu}{\sigma} \tag{5.24}$$

includes the signal width σ, that expresses the experimental resolution on each measurement of the decay time t. The mean value μ parametrises the average bias on that measurement. The underlying Gaussian is assumed to be a result of the detector resolution.

Influence of Selection Cuts   The influence of the cut parameters applied to reduce the number of background events on the lifetime measurement is investigated for all pure signal samples. The neutralino lifetime is reconstructed for all the investigated scenarios, without any selection cuts, after one selection cut at the time and after
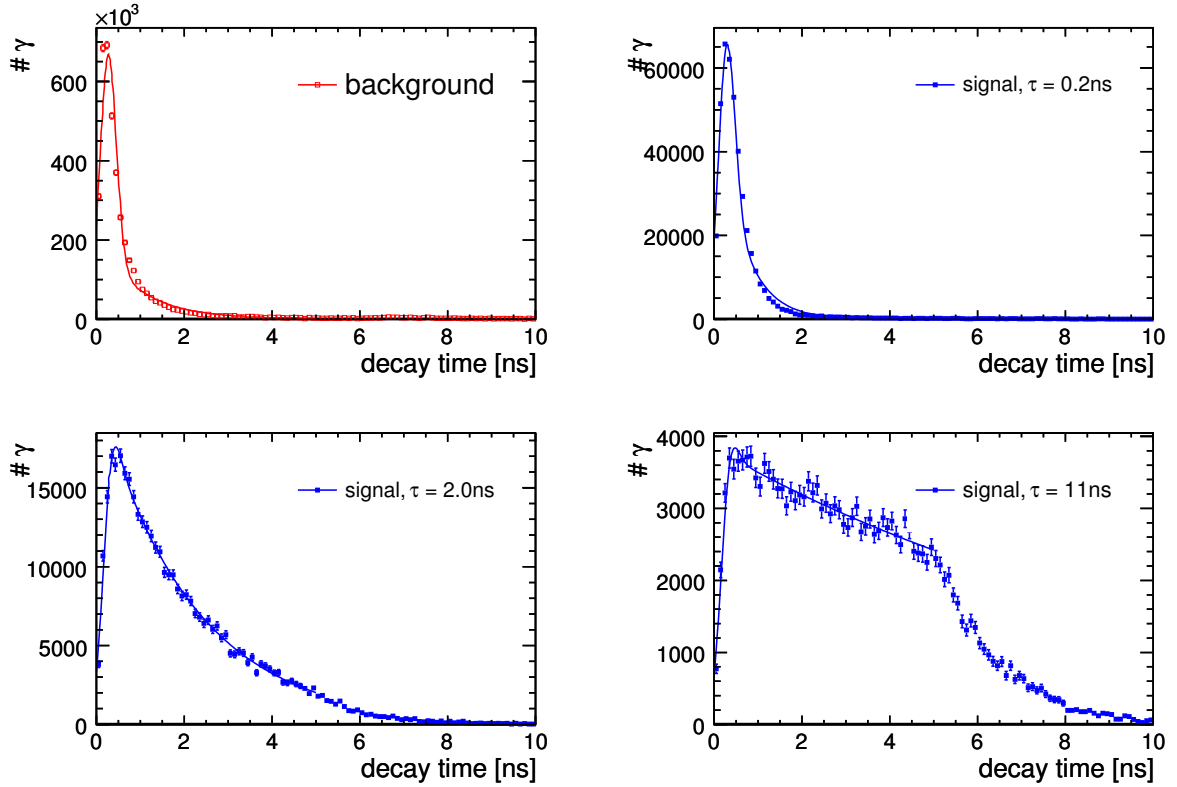
Figure 5.14: Neutralino lifetime reconstruction for background-only events in the upper-left plot, and signal-only events with $\tau_{\tilde{\chi}_1^0} = 0.2$ ns (upper-right plot), $\tau_{\tilde{\chi}_1^0} = 2.0$ ns (lower-left plot) and $\tau_{\tilde{\chi}_1^0} = 11.0$ ns (lower-right plot) input lifetime, respectively. Plotted are events without any selection cuts applied.

| | τ_{reco}[ns] | | |
	$\tau_{\text{true}} = 0.2$ns	$\tau_{\text{true}} = 2.0$ns	$\tau_{\text{true}} = 11.0$ns
no cut	0.575 ± 0.002	2.13 ± 0.01	10.9 ± 0.3
E_{sum}	0.575 ± 0.002	2.13 ± 0.01	10.5 ± 0.3
#hits	0.573 ± 0.002	2.14 ± 0.01	11.2 ± 0.3
$\not{E}_t$	0.569 ± 0.002	2.10 ± 0.01	10.3 ± 0.2
at least two γ with			
E_γ	0.577 ± 0.002	2.14 ± 0.01	11.1 ± 0.4
$|\cos(\theta_\gamma)|$	0.498 ± 0.002	2.20 ± 0.01	15.0 ± 0.9
all cuts	0.477 ± 0.002	2.8 ± 0.01	10.9 ± 0.5

Table 5.7: Influence of the selection cuts on the neutralino lifetime reconstruction for the pure signal samples. Only statistical uncertainties are stated here.

all selection cuts together. The results are listed in table 5.7, including statistical uncertainties.

For the small lifetime scenarios, the reconstructed lifetime is much larger than the input lifetime. In contrast to that, the long lifetime scenario is correctly reconstructed. At small lifetimes the detector resolution smears out the angular and the distance

	$\tau_{\text{true}} = 0.2$ns	$\tau_{\text{true}} = 2.0$ns	$\tau_{\text{true}} = 11.0$ns
$f_{\text{sig}}\,[\,\%\,]$	52.0 ± 0.2	92.0 ± 0.1	91.3 ± 0.2
$\mu\,[\text{ns}]$	$0.570 \pm \text{const}$	$0.570 \pm \text{const}$	$0.570 \pm \text{const}$
$\sigma\,[\text{ns}]$	$0.430 \pm \text{const}$	$0.430 \pm \text{const}$	$0.430 \pm \text{const}$
$\tau_{\text{reco}}\,[\text{ns}]$	0.501 ± 0.002	2.13 ± 0.01	10.8 ± 0.5

Table 5.8: Fitted parameters for the neutralino lifetime reconstruction using kinematic constraints. Stated are only statistical uncertainties.

reconstruction, necessary for the lifetime reconstruction. The resulting Gaussian has a similar width as the neutralino exponential. At longer lifetimes, the influence of the detector smearing is reduced.

Most selection cuts do not significantly disturb the lifetime measurement. Only the cut on the angular distribution seems to have a larger impact, especially on the long-lifetime scenario. However, since it is essential to reduce the background, it is kept for this analysis. An improved selection method can help to improve the lifetime reconstruction in the future.

Lifetime Reconstruction using Data Samples   In reality, the signal will be accompanied by background. For the process under investigation this background is only from Standard Model processes, displayed in the upper left plot of figure 5.14, which are assumed to be known with very high precision. The reconstructed background events do not peak at zero decay time, as one would expect since all events originate from the interaction point. This shift in the mean value can be explained with the shift in angular reconstruction visualised in figure 5.6(a). Since $t \propto \sin \Psi$ (cf. equation 5.21), a $6\,\%$ shift in Ψ introduces up to $4\,\%$ shift in the decay time.

The data samples include signal and background after all selection cuts. The fit resulting from the background-only sample is subtracted and the remaining histogram, plotted in figure 5.15, are taken to be signal events. To account for remaining background the resulting lifetime distribution is fitted with:

$$f(t) = f_{\text{sig}} \cdot \left(\exp\left[\frac{-t}{\tau} \right] \otimes \frac{1}{\sigma\sqrt{2\pi}} \exp\left[-\frac{t'^2}{2} \right] \right) \otimes f_{\text{bkg}} \cdot \left(\frac{1}{\sigma\sqrt{2\pi}} \exp\left[-\frac{t'^2}{2} \right] \right), \quad (5.25)$$

where f_{sig} and f_{bkg} represent the fraction of signal and background events, respectively, with $f_{\text{sig}} + f_{\text{bkg}} = 1$. The underlying Gaussian is assumed to be a result of the detector resolution, and is therefore taken to be the same for signal and background. In principle it can be determined from any physics signature but the signal. Since the background sample is available anyhow, the mean and width are determined from the fit to the background-only sample, and are subsequently fixed for the data sample.

Plotted in figure 5.15 are the pure signal spectrum, as well as the background and the background subtracted data sample with the corresponding fit. The background subtracted data sample follows the same distribution as the signal only sample. And the fitting results, listed in table 5.8 with their statistical uncertainties, show that the remaining background contribution is rather small for the $\tau_{\tilde{\chi}_1^0} = 2.0\,\text{ns}$ and the $\tau_{\tilde{\chi}_1^0} = 11.0\,\text{ns}$ sample.
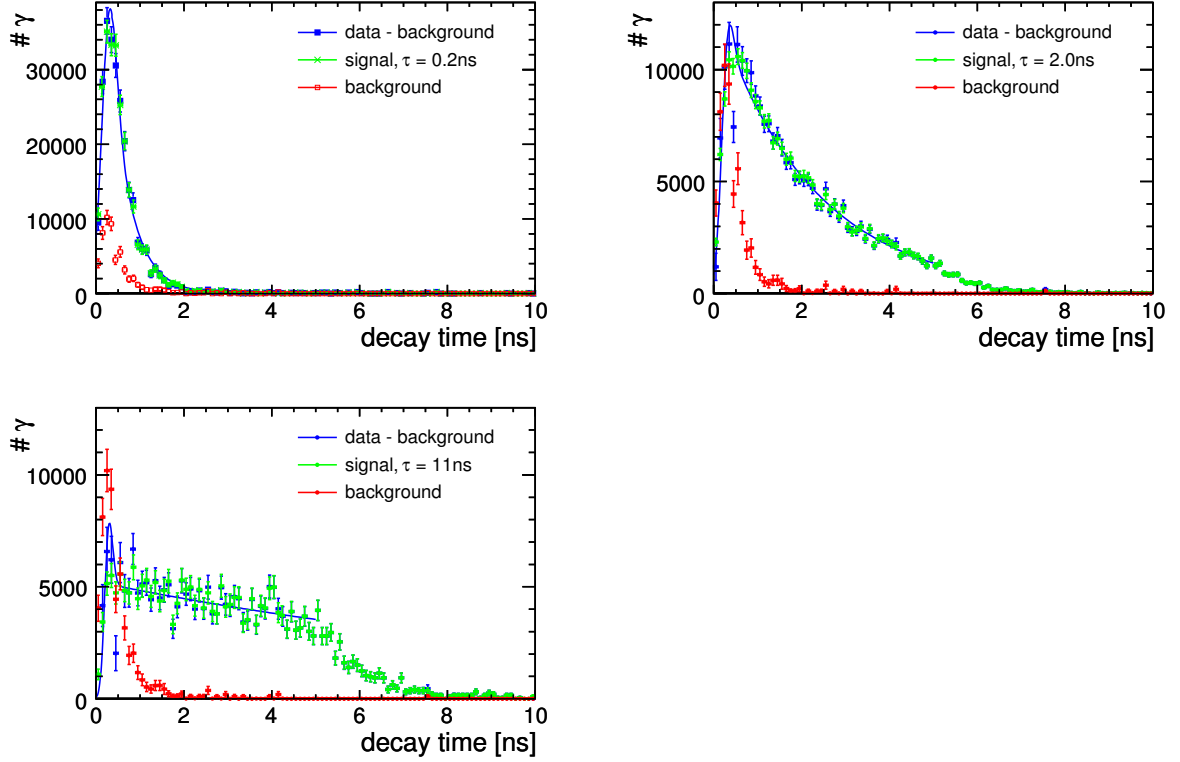
Figure 5.15: Neutralino lifetime reconstruction for $\tau_{\tilde{\chi}_1^0} = 0.2\,\text{ns}$ (upper-left plot), $\tau_{\tilde{\chi}_1^0} = 2.0\,\text{ns}$ (upper-right plot) and $\tau_{\tilde{\chi}_1^0} = 11.0\,\text{ns}$ (lower-left plot) input lifetime, respectively. Plotted are the signal-only sample (green dots) and the background subtracted data (blue dots) with the corresponding fit (blue line) and background (red dots). In each case after all selection cuts.

The resulting lifetime for the long-lived scenario is well in agreement with the fitting result from the pure signal sample after selection cuts and the input lifetime. Neglecting systematic errors, the aspired lifetime resolution of $\Delta\tau/\tau \leq 10\,\%$ can be achieved for this scenario. It might be further improved by implementing the HCAL in the photon reconstruction, to collect also the photon showers starting late in the ECAL and leaking into the HCAL.

Also in the fast decay scenario the reconstructed lifetime is longer than the input lifetime. The fitted background fraction is determined to be $48\,\%$, which is definitely too much, given the signal-to-background ratio is determined to be $3.9 : 1$ and the fit to the background sample has been subtracted. In this scenario the lifetime reconstruction is limited by the algorithm performance and the detector resolution. The reconstructed signal distribution is too close to the reconstructed background distribution to be well determined. The signal lifetime determination could be improved by taking advantage of photons undergoing pair production in the tracking volume, which occurs in $15\,\%$ of the events. These events could be reconstructed with the help of the tracking detectors, which have a much better spatial and angular resolution than the ECAL.

In the medium lifetime scenario the reconstructed lifetime is $6.5\,\%$ higher than the input lifetime. Just as in the short lifetime scenario, the reconstruction is limited by the angular reconstruction. The systematic shift observed in the angular reconstruction

ILD ECAL Geometry and Performance	
Barrel Dimension	$185\,\mathrm{cm} < r < 202\,\mathrm{cm}$
Endcap Dimension	$245\,\mathrm{cm} < |z| < 262\,\mathrm{cm}$
Energy Resolution	$16.7\,\% / \sqrt{E\,[\mathrm{GeV}]} \oplus 0.61\,\%$
Spatial Resolution	$0.4\,\mathrm{cm} / \sqrt{E\,[\mathrm{GeV}]} + 0.8\,\mathrm{cm}$
Angular Resolution	$131\,\mathrm{mrad} / \sqrt{E\,[\mathrm{GeV}]} \oplus 3.7\,\mathrm{mrad}$

Table 5.9: ILD ECAL geometrical dimensions and performance determined with the photon clustering algorithm.

has to be reduced to obtain a better result. Alternatively, the correlation between true and reconstructed angle, presented in figure 5.6 could be used to apply a correction factor to the reconstructed angle.

5.5 Conclusion and Outlook

The overall performance of the detector configuration and the cluster algorithm is summarised in table 5.9. The energy resolution is well in agreement with measurements from a Si-W ECAL prototype (cf. equation 7.4). The achieved spatial resolution is comparable with the estimated performance of $0.4\,\mathrm{cm} / \sqrt{E\,[\mathrm{GeV}]}$ [47]. However, the angular resolution had been estimated to achieve $55\,\mathrm{mrad} / \sqrt{E\,[\mathrm{GeV}]}$ [47], while the measured angular resolution is much worse. Thus, there is clearly room for improvement in the angular cluster reconstruction method. Not only the resolution, but also the deviation between reconstructed and true photon incidence angle should be improved for future ECAL studies.

With this performance, the neutralino mass obtained from a fit to the kinematic edge of the photon energy distribution is $(126.5 \pm 2.6)\,\mathrm{GeV}$. The reconstructed mass is much smaller than the input mass of $151.0\,\mathrm{GeV}$. The mass reconstruction is influenced by the selection cuts, especially the upper bounds on the ECAL energy sum and number of hits, which might have to be adopted to gain a better mass measurement. The mass reconstruction from the signal-only sample yields a better agreement between input mass and fitted mass. The remaining difference is likely to emerge from the effects of beamstrahlung and initial state radiation. They are simulated but not corrected for during reconstruction, thus the true centre-of-mass energy is not $\sqrt{s} = 500\,\mathrm{GeV}$, which disturbs the mass reconstruction. If the true centre of mass energy has not been $\sqrt{s} = 500\,\mathrm{GeV}$ but only $\sqrt{s} = 497.5\,\mathrm{GeV}$, the reconstructed mass for the signal-only sample yields $m_{\mathrm{data}} = (151.3 \pm 0.6)\,\mathrm{GeV}$. Thus, in principle the mass reconstruction method is assumed to be correct, but it has to be further optimised for future studies.

The neutralino lifetime is estimated for three lifetime scenarios, using simple geometrical constraints and kinematic considerations. The reconstructed lifetime for the long-lived scenario is well in agreement with the input lifetime ($\tau_{\tilde{\chi}_1^0} = 11.0\,\mathrm{ns}$). This scenario is challenging due to the short ECAL depth. It can be further improved and extended to even longer lifetime scenarios by implementing the HCAL in the photon reconstruction. In the medium lifetime scenario the reconstructed lifetime is $6.5\,\%$

higher than the input lifetime ($\tau_{\tilde{\chi}_1^0} = 2.0\,\mathrm{ns}$). It is limited by the angular reconstruction. The systematic shift observed in the angular reconstruction has to be reduced to obtain a better result. The problems in the angular reconstruction become even more pronounced in the fast decay scenario, where again the reconstructed lifetime is longer than the input lifetime ($\tau_{\tilde{\chi}_1^0} = 0.2\,\mathrm{ns}$). The reconstructed signal lifetime distribution is too close to the reconstructed background lifetime distribution to be well separated.

It can be concluded that the presented performance is sufficient to get an estimate of the neutralino mass and lifetime in a GMSB scenario. Although there is still room for improvement, this can be achieved in software performance rather than in detector geometry adjustments.

The implementation of timing information in the simulation can help to reach a better distinction between signal and background events. Moreover, it offers an additional possibility to reconstruct the neutralino lifetime from the delayed arrival of the decay photons.

To gain more statistics, the other kinematically accessible SUSY processes listed in table 5.2 can be utilised, since they all decay via the NLSP into the LSP and a photon.

The reconstruction method can be extended to smaller lifetimes, utilising the projective tracking methods. Roughly 15 % of all photons undergo pair-production in the tracking volume. The resulting charged tracks can be used to get a very good estimate on the neutralino direction.

Longer-lived scenarios can profit from the usage of HCAL information. Furthermore, they can be reconstructed with a model-dependent statistical method. As the probability to detect a photon from a neutralino decay is a function of the neutralino lifetime, the ratio of two-photon to one-photon events in SUSY processes is also a function of the neutralino lifetime.

6 The Physics Prototype

An analogue hadron calorimeter (AHCAL) prototype of $5.3\,\lambda_i$ thickness has been constructed by the CALICE[1] collaboration. It consists of a 38-layers sandwich structure of steel plates and highly-segmented scintillator tiles that are read out by silicon photomultipliers (SiPMs).

Ultimately, the physics goals are the study of hadron shower shapes and testing the concept of particle flow. The technical goal consists of testing the performance and reliability of 7608 SiPMs, as well as the calibration and long term monitoring of as many calorimeter cells.

6.1 CALICE prototypes

Together with a silicon-tungsten electromagnetic calorimeter (Si-W ECAL) [105] and a tail catcher and muon tracker (TCMT) [106], the AHCAL has been exposed to muon, electron and hadron test beams at different energies and incident angles [107]. A photograph of the CALICE Si-W ECAL, AHCAL and TCMT in the test beam installation at CERN in summer 2006 is given in figure 6.1.

The design of the CALICE prototypes is inspired by the calorimeter layout of the International Large Detector (cf. chapter 3.3), and the experience gained from the prototype is a guidance for the design of the calorimetric system for an ILC detector.

The first test of the CALICE prototypes were accomplished with test beams at CERN in the years 2006 and 2007. Further studies continued at FNAL in the years 2008 and 2009. The presented analysis is focusing on the August 2006 and July 2007 data sets where the AHCAL has been exposed to electrons without the Si-W ECAL in the beam line (cf. section 7.1).

6.2 The Analogue Hadron Calorimeter

The analogue hadron calorimeter prototype, is a roughly $1\,\mathrm{m}^3$ sandwich structure with 38 active layers. The lateral size guarantees that the core of hadron showers with up to several tens of GeV (the range being most relevant for the ILC) is laterally contained. The longitudinal size is adopted to that of the full-size detector, which is limited by the radius of the magnetic coil of the corresponding ILD detector. The longitudinal segmentation is of the order of one X_0 and the lateral dimension of the active elements is of the order of one Molière radius to resolve the electromagnetic substructure in hadron showers. A detailed description of the detector and its calibration procedure and performance is given in [108].

---

[1]CAlorimeter for the LInear Collider with Electrons
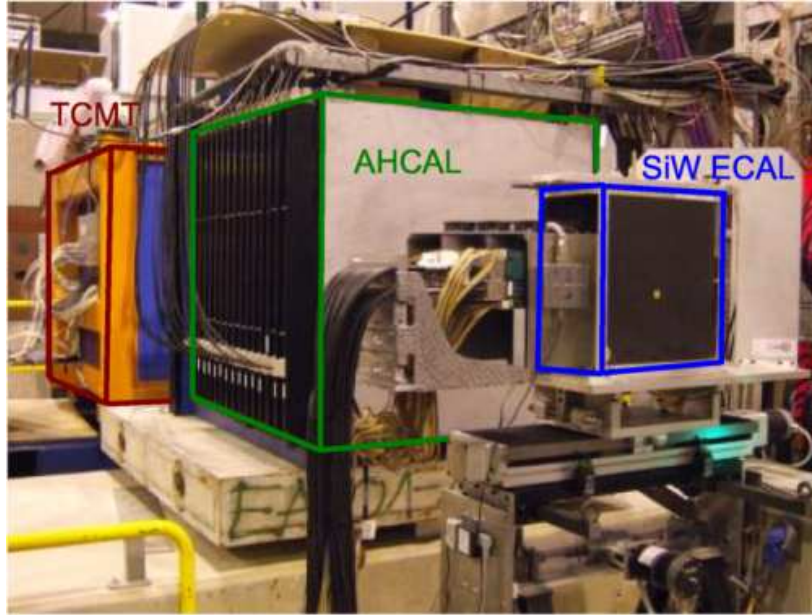
Figure 6.1: Photograph of the CALICE test beam setup.

6.2.1 Cassette Layout

The first 30 layers contain 216 scintillating tiles ranging from a core of 10×10 tiles with $3 \times 3 \, \mathrm{cm}^2$ size, over three rings with $6 \times 6 \, \mathrm{cm}^2$ to a closing ring with $12 \times 12 \, \mathrm{cm}^2$ wide scintillating tiles. A photograph of this mosaic is shown in figure 6.2(a). For the last eight layers the highly granular core is replaced by $6 \times 6 \, \mathrm{cm}^2$ tiles for cost reasons, resulting in 141 channels per layer. This sums up to 7608 scintillating tiles in total, each of them individually read out.

A schematic layout of one AHCAL layer is displayed in figure 6.2(b). The scintillating tile mosaic is covered by reflective foil (3M VN2000 superradiant), to ensure good light collection efficiency. A plastic material (FR4) on top is supporting the coaxial read-out cables and light-guiding fibres from the calibration system (named cable-fibre-mix in table 6.1). All this is housed in stainless steel cassettes with $0.2 \, \mathrm{cm}$ wall thickness. The readout electronics are placed on one side, the calibration and monitoring board on the opposite side of the cassettes. The cassettes are interleaved by steel (S235) absorber plates with an average depth of $1.74 \, \mathrm{cm}$, varying from 1.67 to $1.76 \, \mathrm{cm}$. Air gaps of $4 \, \mathrm{mm}$ width allow easy insertion and/or exchange of single cassettes and compensate for tolerances in the absorber plate thickness. The last AHCAL layer is terminated by a $2.05 \, \mathrm{cm}$ thick steel end-plate.

The composition of a full AHCAL layer is listed in table 6.1 together with the corresponding radiation lengths and the ratio between radiation and interaction lengths. Using these material properties and equation 4.10 the whole prototype with 38 active layers, 38 absorber plates and one end-plate sums up to a depth of $48.0 \, X_0$ or $5.3 \, \lambda_i$ along $122.3 \, \mathrm{cm}$.
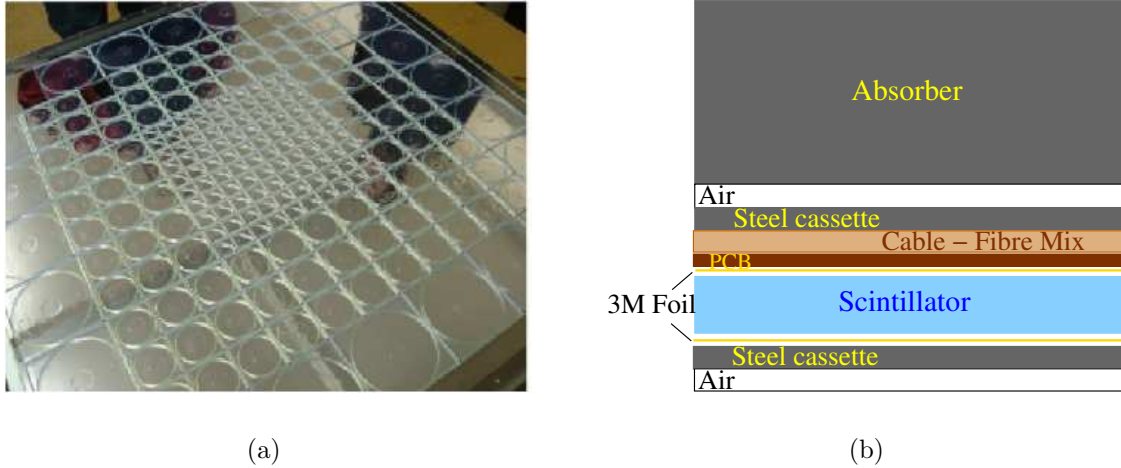
Figure 6.2: (a) Photograph of one fine granular AHCAL layer. (b) Schematic layout of one AHCAL layer.

Material	Depth [cm]	ρ [g/cm^3]	X_0 [cm]	λ_i/X_0	R_M [cm]
Steel	1.74 ± 0.02	7.87	9.64	9.6	1.7
Scintillator	0.50	1.03	41.3	1.7	9.4
FR4 plate	0.10	1.70	17.5	2.8	5.2
Air gaps	0.25	0.001	28516.1	2.5	7330.0
Cable-fibre-mix	0.15	0.12	224.3	3.25	8.3
Reflective foil	0.02	1.07	41.1	1.67	9.4

Table 6.1: AHCAL material and structure composition as implemented in the Mokka geometry.

6.2.2 Read-Out Chain

Particles traversing the prototype are generating light in the scintillating tiles. This light is shifted from ultraviolet to green by a wavelength shifting (WLS) fibre, and detected by semiconductor-based photosensors, called silicon photomultipliers (SiPM). The optical path sketched in the upper row of figure 6.3 is followed by an electronic chain, indicated in the lower row of the same figure. Eighteen SiPM signals are fed into one application-specific integrated circuit (ASIC) chip for amplification and shaping [109]. Twelve ASICs are located on one common Front-End (FE) board. Eight of these FE boards are sampled in one CALICE Readout Card (CRC) port [110], each CRC has eight input ports. Five CRCs are needed to read out the full AHCAL prototype. In the following the single steps of this chain are described in more detail.

The AHCAL prototype is not scalable to a full detector for the ILC. Many now external components, e. g. the read-out electronics, need to be integrated into the ILC detector volume in the future.
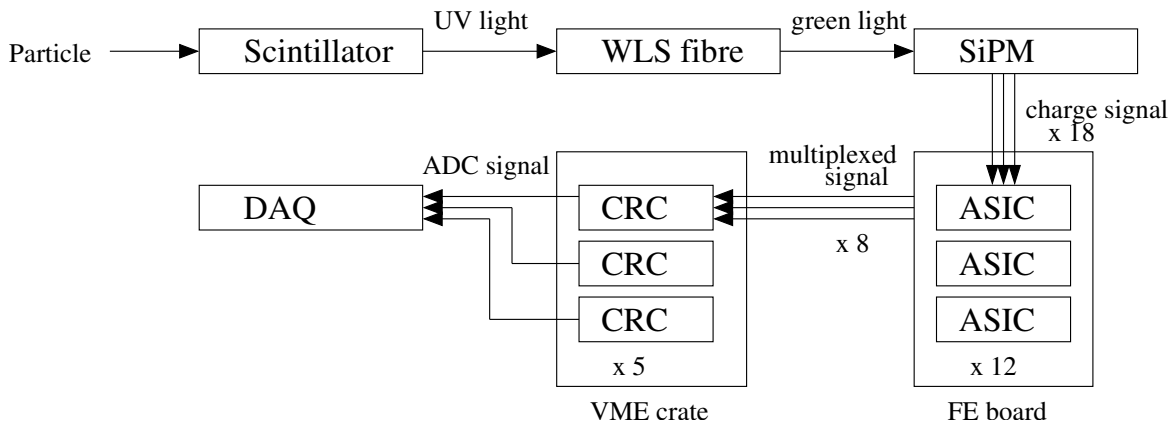
Figure 6.3: Illustration of the AHCAL read-out chain.
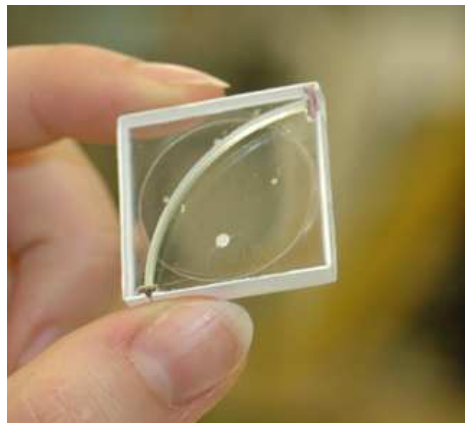
Figure 6.4: Picture of a $3 \times 3\,\mathrm{cm}^2$ scintillating tile with embedded quarter-circle shaped wavelength shifting fibre.

Scintillating Tile The active material is built up from $0.5\,\mathrm{cm}$ thick scintillating tiles from the Vladimir plant, shown in figure 6.4. The scintillator material is p-terphenyle (BASF-130) dissolved in polystyrene. A $0.1\,\mathrm{cm}$ diameter green WLS fibre (Y11(300)) from Kuraray is embedded in each tile. This is realised in a full circle groove for the $6 \times 6\,\mathrm{cm}^2$ and $12 \times 12\,\mathrm{cm}^2$ tiles, while a quarter circle is chosen for the $3 \times 3\,\mathrm{cm}^2$ tiles.

Plastic scintillators are solutions of organic scintillators in a polymerised solid. They can easily be shaped, and are relatively cheap. In addition they give a fast signal (20-30 ns) and sufficient light output. The scintillation molecules get excited by ionising radiation and subsequently emit UV-light during de-excitation. The amount of light is proportional to the deposited energy, on average roughly $100\,\mathrm{eV}$ are needed to produce one photon. The smallest detectable physical signature, a minimum ionising particle (MIP, cf. section 4.2.3), produces approximately 5000 photons. Since the energy of emitted photons is smaller than the energy needed to excite the molecules, the scintillator is transparent for the emitted light.

The tiles are covered by reflective foils at the top and the bottom side to enhance the
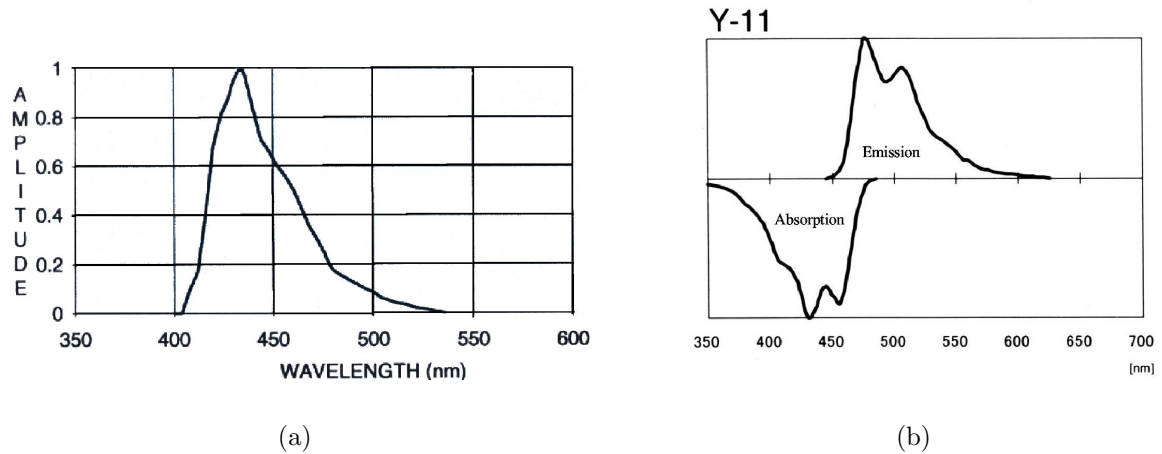
Figure 6.5: (a) Emission spectrum of an example scintillator. (b) Absorption and emission spectrum of the wavelength shifter.

collection efficiency, and chemically treated at the edges for diffuse reflection and to minimise inter-tile crosstalk.

WLS fibres are used to guide the scintillation light to photodetectors. They shift the light from UV to green, since the photodetectors in use have the largest sensitivity in the green wavelength range. As shown in figure 6.5, the absorption spectrum peaks around $\lambda = 420\,\text{nm}$, meeting the scintillator emission peak. The emission spectrum peaks at $\lambda = 500\,\text{nm}$, fulfilling the requirements of the photosensors.

The WLS fibre collects light from the entire scintillating tile. It is coupled to a mirror on one side, and to a photodetector on the other side. To allow a good light guidance, the fibre is cladded with a material of higher refraction index. This leads to reflections for photons hitting the cladding with an angle larger than $\sin \alpha = n_0/n_1$. Thereby, the fibre not only enhances the detection efficiency, but also provides a uniform light collection over the entire scintillating tile [111].

Silicon Photomultiplier A semiconductor device developed by MEPhI/PULSAR and called Silicon Photomultiplier (SiPM) is used as photosensor. A SiPM is a pixelated sensor consisting of an array of avalanche photodiodes operated in Geiger mode. The total SiPM surface of $1\,\text{mm}^2$ is divided in 1156 pixels. A picture of the employed SiPM is displayed in figure 6.6(a). Each pixel corresponds to an individual p-n junction to which an external reverse bias voltage U_{bias} is applied.

As sketched in figure 6.6(b), incident photons create electron-hole pairs in the depletion region, which drift towards the electrodes. Due to the high electric field of 10^5 V/cm, they can knock out electrons from the crystal lattice and thus create new charge carriers. Once the bias voltage exceeds a certain breakdown voltage U_{break}, the number of electron-hole pairs grows faster than they can be collected at the electrodes. As a result the current grows exponentially in this so-called Geiger mode, until it is quenched by a resistor with $R_{\text{pix}} = 1 - 20\,\text{M}\Omega$. Photodetectors operated in Geiger mode achieve a gain of $G_{\text{pix}} \sim 10^5 - 10^6$, comparable with traditional photomultiplier tubes.

Even though the response of each single pixel is binary, the total SiPM response is quasi-analogue, since all pixels are read out in parallel, and the number of fired pixels

(a)

(b)
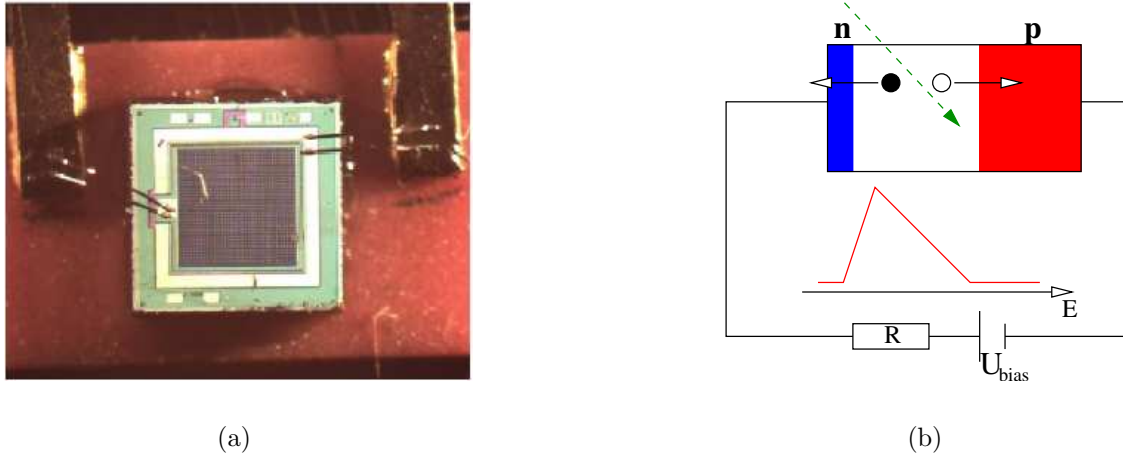
Figure 6.6: (a) Picture of a SiPM. (b) Schematic of a SiPM pixel: a p-n junction.

is proportional to the amount of incident light, at least for small light amplitudes. However, there is only a limited amount of pixels available, and each pixel has a finite recovery time. This recovery time $\tau_R = R_{\text{pix}} \cdot C_{\text{pix}} \approx 25\,\text{ns} - 1\,\mu\text{s}$ depends on the pixel resistor R_{pix} and its capacity C_{pix} [112]. As a consequence, at high light intensities some photons cannot fire a pixel and SiPMs show saturation behaviour.

Photons produced in one pixel during the avalanche can cross the pixel boundaries and induce a new avalanche in neighbouring pixels. For the AHCAL prototype, SiPMs with less than 35 % inter-pixel crosstalk have been selected. In principle this value can be further reduced by optically decoupling each pixel from its neighbours. However, most techniques that reduce the inter-pixel crosstalk add special boundaries between the pixels, which reduce the active area and thus worsen the geometrical efficiency.

After production, the response of each SiPM to an increasing intensity of light is measured under defined conditions before the SiPM is mounted on a tile. The shape of the response function is similar for all SiPMs, and individual curves agree on a level of 15 %. In addition the response curves are constantly monitored for eventual changes, e.g. due to dying pixels, by a calibration and monitoring system, described in [113]. An example curve, plotted in figure 6.7(a), shows the SiPM signal as a function of the light intensity.

An important characterisation of photodetectors is the photon detection efficiency ε_{PDE}. For photomultiplier tubes it is defined as the probability that an incident photon is releasing a primary photoelectron, which is also called quantum efficiency ε_{QE}. For photomultipliers it is usually around $\varepsilon_{\text{QE}} \approx 20\,\%$ [116]. Like other silicon-based photodetectors, SiPMs have a quantum efficiency close to $\varepsilon_{\text{QE}} \lesssim 80\,\%$. Additionally, the probability for a charge carrier to initiate a Geiger discharge $\varepsilon_{\text{Geiger}}$ has to be taken into account. This value is typically close to $\varepsilon_{\text{Geiger}} \approx 100\,\%$ if the SiPM is operated well above its breakdown voltage. Moreover, since not the full SiPM surface is sensitive to light, a geometrical efficiency $\varepsilon_{\text{geo}} = A_{\text{pix}}/A_{\text{tot}}$ describing the ratio of active area A_{pix} to the total SiPM surface A_{tot} has to be considered as well. Depending on the number of pixels per millimetre, the shape of the pixels and the size of the quenching resistors, the geometrical efficiency varies typically between 20 % and 30 % for 1000 pix/mm^2.

(a)   (b)
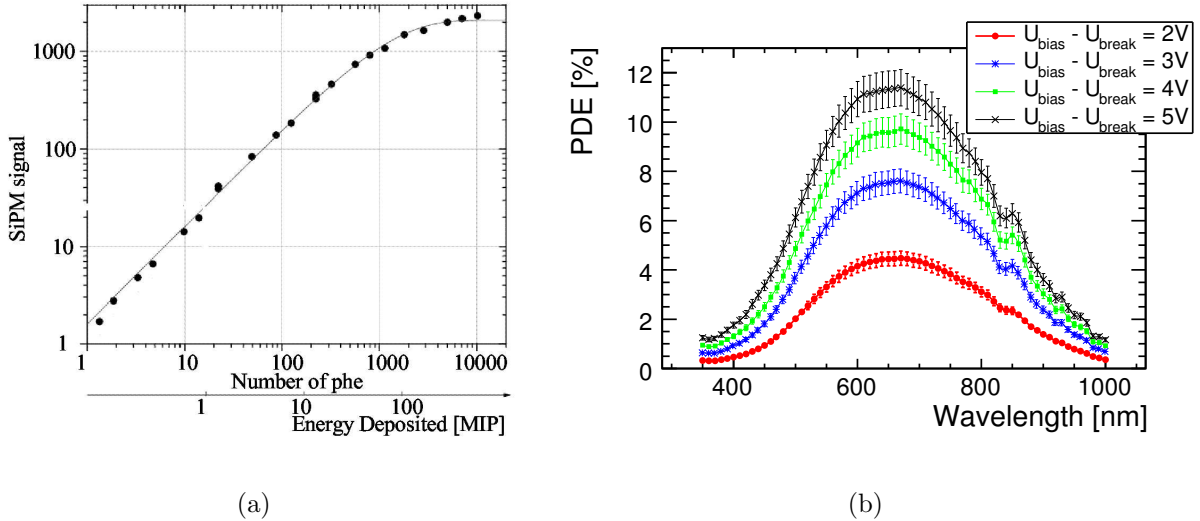
Figure 6.7: (a) SiPM response function [114]. (b) Photon detection efficiency for SiPM
at different operation voltages as a function of the incident wavelength [115].

The overall SiPM photon detection efficiency is defined as

$$\varepsilon_{\mathrm{PDE}} = \varepsilon_{\mathrm{QE}} \cdot \varepsilon_{\mathrm{geo}} \cdot \varepsilon_{\mathrm{Geiger}}. \tag{6.1}$$

The photon detection efficiency is plotted in figure 6.7(b) as a function of incident wavelength for SiPMs at different operation voltages. At $3\,\mathrm{V}$ above breakdown voltage, which is a common operation voltage for SiPMs in the AHCAL, the SiPM photon detection efficiency peaks at $\varepsilon_{\mathrm{PDE}} \approx 7.5\,\%$ for red light ($\lambda = 660\,\mathrm{nm}$). In the peak emission region of the embedded wavelength shifting fibres ($\lambda = 520\,\mathrm{nm}$) the SiPM photon detection efficiency is around $\varepsilon_{\mathrm{PDE}} \approx 4.5\,\%$. With this constellation of scintillating tile and WLS fibre, one MIP releases few tens photoelectrons in the SiPM.

The photon detection efficiency could be further improved by increasing the bias voltage, however this would also increase the SiPM noise. Thermal excitation and tunnelling effects lead to random generation of electron-hole pairs. Due to the Geiger operation, these 'dark' carriers are amplified in avalanches leading to an electrical signal that cannot be distinguished from a light-induced one. In principle, the average dark-count rate can be measured and corrected for, but as it is subject to statistical fluctuations, it is still a source of noise. The selected SiPMs have dark-count rates below $3\,\mathrm{kHz}$ at room temperature above a threshold of half a MIP [108]. This value can be significantly lowered by cooling the SiPMs.

SiPMs offer some advantages in comparison to traditional photomultiplier tubes. They are relatively cheap, which is important, since an ILD-type calorimeter needs millions of them. Their small size, and high gain offer the possibility to mount them directly on each scintillating tile. This avoids long transportation of light, which always implies signal losses. And equally important, they can be operated in high magnetic fields [114], which allows the calorimeter to be placed inside a $3.5\,\mathrm{T}$ magnetic field.

One of the disadvantages is the saturation effect, discussed above. Another point to be taken into account is the temperature and voltage dependence inherent to any semiconductor device. The SiPM signal, gain and noise depend on the difference between

SiPM T&V Dependence				
dG/dV	=	2.6	± 0.3	%/0.1V
dG/dT	=	−1.7	± 0.3	%/K
dA/dV	=	5.6	± 0.8	%/0.1V
dA/dT	=	−3.7	± 1.1	%/K

Table 6.2: Temperature and voltage dependence of SiPM gain G and SiPM response A [117].

bias and breakdown voltage. Obviously this difference changes if the applied voltage changes. But since the breakdown voltage depends on the SiPM temperature, a change in temperature also influences the SiPM behaviour.

It is one of the aims of the physics prototype to prove that these challenges can be handled. How to correct for the saturation behaviour is discussed in section 6.3.3. The dependence of gain G and amplitude A on temperature T and voltage V fluctuations is listed in table 6.2, where the error indicates the spread over all measured SiPMs. How to handle these fluctuations is discussed in section 6.3.4.

Electronics and DAQ The purpose of signal processing is to maximise the signal-to-noise ratio. The SiPM signal is a current pulse with a short rise time below one nanosecond and an exponential decay time up to several hundred nanoseconds. This pulse is integrated over time, resulting in a charge proportional to the detected energy deposition.

The charge is passed to an ASIC chip. Each ASIC, named ILC-SiPM, houses an 18-fold multiplexed chain of pre-amplifier, shaper, and sample-and-hold circuit. It transforms the SiPM charge signal into an amplified voltage signal. A pulse shaper is used to reduce electronics noise, and provide the latency needed for a beam trigger decision. A detailed description of the ASIC chip can be found in [118, 119].

The ASIC chip is used in two different working modes serving the different requirements of calibration and data taking, and therefore called calibration and physics mode. This allows to optimally fit the complete SiPM working range to the used 16-bit analogue-to-digital converter (ADC) range. Single photons have to be resolved for the SiPM calibration. Therefore, a short shaping time (40 ns) and a high amplification (approximately a factor 100) are needed. During data taking signals equivalent to several 100 MIPs have to be recorded. Thus, less amplification (approximately a factor 10) has been chosen to fit the ADC range. Furthermore, the shaping time in physics mode is longer (the effective shaping time is between 180 ns and 200 ns) to provide the latency for the trigger decision. This has the disadvantage that it is not possible to observe single photons, as it also integrates over more SiPM dark-count rate.

Each ASIC chip reads 18 SiPM signals and transforms them into one multiplexed output signal that is then passed to the CRC [110]. They house a 16-bit analogue-to-digital converter for each ASIC output. There is no zero suppression at this signal processing stage, i.e. every signal from every channel is recorded. Each CRC has eight input ports, each receiving the signal from twelve ASIC chips. This results in five CRC boards inserted into one nine-unit Versa Module Eurocard (VME) crate to read

out the whole AHCAL physics prototype. The CRC signal is passed on through the VME bus and a VME-PCI (Peripheral Component Interconnect) interface to the data acquisition (DAQ).

6.3 AHCAL Calibration

6.3.1 Calibration Concept

One of the aims of the test beam effort is to establish a reliable and robust calibration chain. This requires several measurements with beam and with LED light. The calibration chain can be summarised in the following steps:

- equalisation of all cell responses;

- correction of the non-linear SiPM response;

- calibration to the GeV scale with electromagnetic showers from test beam facilities;

- correcting for the e/π-ratio.

The equalisation of all cell responses with minimum ionising particles is described in section 6.3.2. It is the only calibration step necessary for linear devices. However, the AHCAL response is not linear. Thus, different methods to correct for the non-linear SiPM response are introduced in section 6.3.3. The calibration to the GeV scale is subject of the next chapter (chapter 7).

The correction for the e/π-ratio is not discussed in this thesis, which focuses on electromagnetic processes. In principle it can be obtained from the detector response to well defined electron and pion data in a test beam environment. As the ratio is energy dependent, electrons and pions should be measured and compared at several energies. The obtained energy dependence can than be used to correct the measured energy for pions at arbitrary values in a collider environment.

6.3.2 Cell Equalisation

The response of the 7608 AHCAL cells is equalised with minimum ionising particles (MIPs, cf. section 4.2.3). These hypothetical particles are approximated by muons that traverse the full calorimeter chain without showering. To obtain a MIP calibration, the prototype is exposed to a wide beam of $E_{\text{beam}} = 120\,\text{GeV}$ muons. The MIP calibration coefficient $A_{\text{MIP}}\,[\text{ADC/MIP}]$, defined as the pedestal-subtracted amplitude in ADC channels corresponding to the most probable value of the distribution obtained from the passage of a muon at normal incidence [120], determines the absolute energy scale of the detector. At the same time, it provides the threshold ($A_{\text{thr}} = 0.5\,\text{MIP} \sim 430\,\text{keV}$) used to suppress cells without signal.

The response of one AHCAL cell to $E_{\text{beam}} = 120\,\text{GeV}$ muons is plotted in figure 6.8. The signal is fitted with the convolution of a Landau and a Gaussian distribution. The noise spectrum, plotted as solid histogram, is well separated from the muon peak. The
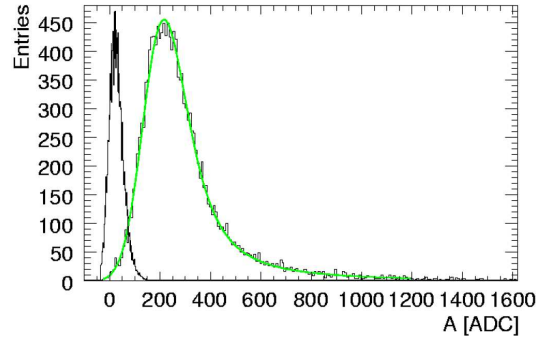
Figure 6.8: Single calorimeter cell response to muons with the corresponding fit (green line) and noise spectrum of the same cell [120].

MIP calibration efficiency, i.e. the amount of successful MIP calibrations, is 98 % for the 2006 and 95 % for the 2007 data set. The calibration fails for cells with broken electrical connection or very noisy SiPMs. The signal over noise ratio, defined as MIP amplitude over pedestal width, is a measure for the separation of a MIP signal and noise. It is found to be $9-10$ in 2007, while a signal over noise ratio of 12 is reached in 2006. Cells without successful MIP calibration are excluded from further analysis.

The uncertainty on the MIP scale has a direct impact on the reconstructed energy. Statistical uncertainties are about one percent, but as most calibration constants the MIP scale changes with temperature and voltage according to table 6.2.

6.3.3 SiPM response

The full calibration of a cell, requires to account for the non-linearity introduced by the limited number of pixels per SiPM and the finite pixel recovery time.

SiPM Response Measurement The response of each SiPM is measured as a function of increasing light intensity before the SiPM is mounted on a scintillator tile. The full SiPM surface is illuminated by homogeneous LED light. The detected SiPM signal is compared to that of a photomultiplier tube with linear response to the same amount of light. The result of this test bench measurement is plotted in figure 6.9. It illustrates the response of 500 arbitrary SiPMs of the AHCAL with respect to the linear photomultiplier tube scale. Assuming a linear SiPM response at low-light intensities, the PMT scale is calibrated by demanding the first three measurements to lie on a one-to-one line. The shape of the response function of all SiPMs is similar, only the saturation level differs.

These test bench measurements can be used to correct for the non-linear SiPM behaviour in the test beam data. The number of 'linear pixels' N_{pe} is estimated from a comparison of the measured amplitude with the corresponding amount of 'linear pixels' from the test bench data. In between data points the curve is interpolated linearly. If the measured amplitude at the test beam is higher than the range of the test bench curve, the last test bench measurement point is used to estimate the correction factor. Cells without response curve measurement are assigned a curve of an arbitrary SiPM.
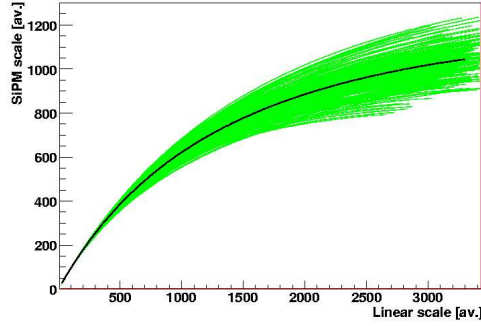
Figure 6.9: Response of 500 arbitrary SiPMs from the AHCAL (green lines) and their mean response (black line) with respect to a linear photomultiplier tube scale.

SiPM Response Parametrisation   Instead of using the measurement of each single SiPM, one can try to parametrise the SiPM response. For a perfect SiPM with N_tot identical pixels, the probability not to fire a pixel with N_γ incoming photons is binomially distributed

$$P_\text{miss} = \left(1 - \frac{1}{N_\text{tot}}\right)^{N_\gamma}. \tag{6.2}$$

Therefore, the number of pixels fired by N_γ incoming photons is

$$
\begin{aligned}
N_\text{pix} &= N_\text{tot} \cdot (1 - P_\text{miss}) \\
&= N_\text{tot} \cdot \left(1 - \exp\left[\log\left(1 - \frac{1}{N_\text{tot}}\right) \cdot N_\gamma\right]\right) \\
&\approx N_\text{tot} \cdot \left(1 - \exp\left[-\frac{N_\gamma}{N_\text{tot}}\right]\right),
\end{aligned}
$$

using the first expansion of the Taylor-series $\log(1 - x) \approx x$, which is valid for small x.

In principle the response function can be expressed in arbitrary units, as long as they are consistent throughout the formula. However, the intuitive scale is the number of fired pixels. This scale is obtained from the SiPM response to low-intensity LED light in the high electronics gain mode. The pulse height spectrum plotted in figure 6.10 shows that the signals from small integer numbers of fired pixels are clearly distinguishable. This excellent resolution provides self-calibration and monitoring of each channel. As the difference between adjacent peaks A_peak is determined by the SiPM gain $G\,[\text{ADC/pix}]$, the distance between adjacent peaks is referred to as gain coefficient. The gain extraction efficiency, i.e. the amount of successful gain calibrations, is 97 % for the August 2006 data set. Cells without successful gain calibration are assigned the average gain value of the corresponding half module, since SiPMs with similar properties, especially a narrow range of bias voltage, are grouped half-module wise.

To account for the different electronic amplification factors used for the gain calibration, which is taken in calibration mode, and the MIP calibration, determined in physics mode, an electronics intercalibration factor C_e is introduced. It is measured from the response of both ASIC configurations to the same LED light intensity. Just
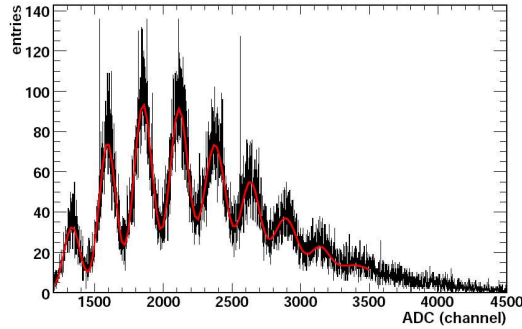
Figure 6.10: SiPM response to low-intensity light [121].

as the gain measurement, this measurement is performed in-situ and is frequently repeated. The extraction efficiency for this method is approximately 99 %, and cells without valid intercalibration factor are assigned the average intercalibration factor of the corresponding half module.

Together with the gain factor, the electronics intercalibration factor translates ADC channels into the number of fired pixels.

$$N_{\text{pix}} = \frac{A_{\text{peak}}^{i+1} - A_{\text{peak}}^{i}}{C_e} = \frac{G}{C_e}. \tag{6.3}$$

The number of fired pixels may not always be identical to the number of incoming photons. Inefficiencies can decrease the effectively available number of pixels, while pixels with a recovery time faster than the sampling time can fire several times and thus increase the effectively available number of pixels. Therefore, the total number of existing pixels N_{tot} has to be replaced by the total number of effectively available pixels N_{max}. Thus, the response function reads

$$N_{\text{pix}} = N_{\text{max}} \cdot \left(1 - \exp\left[-\frac{N_\gamma}{N_{\text{max}}} \right] \right). \tag{6.4}$$

So far, the response function stated in equation 6.4 only describes the SiPM behaviour. To obtain the correction function, it is inverted:

$$
\begin{aligned}
N_\gamma &= -N_{\text{max}} \cdot \log\left(1 - \frac{N_{\text{pix}}}{N_{\text{max}}} \right) \\
&\approx -N_{\text{max}} \cdot \left(-\frac{N_{\text{pix}}}{N_{\text{max}}} - \frac{N_{\text{pix}}^2}{2 \cdot N_{\text{max}}^2} \right) \\
&= N_{\text{pix}} \cdot \left(1 + \frac{N_{\text{pix}}}{2 \cdot N_{\text{max}}} \right),
\end{aligned}
$$

where $\log(1 - x)$ is approximated by $-(x + x^2/2)$, which is valid for small $|x| < 1$. Applying one more approximation valid for small x, namely $1 + x \approx 1/(1 - x)$, the correction function reads

$$N_\gamma \approx \frac{N_{\text{pix}}}{1 - \frac{1}{2 \cdot N_{\text{max}}} \cdot N_{\text{pix}}}. \tag{6.5}$$

(a)

(b)
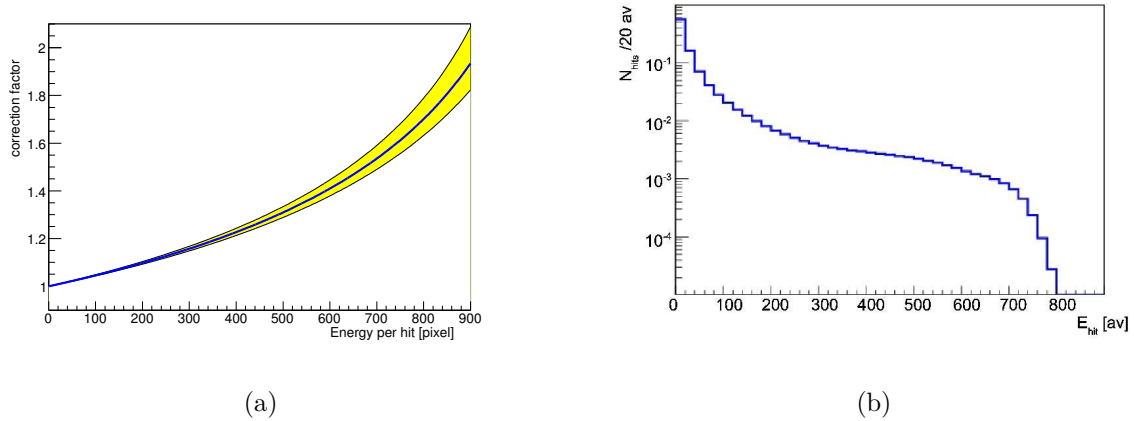
Figure 6.11: (a) Non-linearity correction factor as a function of hit energy. (b) Uncorrected hit energy distribution for a 30 GeV electron run.

The correction factors resulting from the binomial function (cf. equation 6.5) are visualised for $N_{max} = 1000$ pixels in figure 6.11(a) as a function of the hit energy. The yellow band reflects the propagated systematic uncertainties of the calibration coefficients. The frequency with which high correction factors, which have the largest uncertainties, are applied can be estimated from figure 6.11(b). It illustrates the energy deposition per hit during a 30 GeV electron run. One out of 100 hits has an energy deposition above 150 fired pixels, and thus requires correction factors above 1.1, while only every thousandth hit has an energy deposition above 600 fired pixels, which requires correction factors above 1.4. This justifies the approximations applied in the parametrisation, which are only valid for small signals. It is also illustrating that the large uncertainties on the correction factor at high uncertainties are not directly propagated to the energy sum.

6.3.4 Calibration Verification

The figure of merit of the calibration is the so called light yield LY, a measure for the average number of pixels fired by a MIP. The design goal for the AHCAL is 15 pixels per MIP, a compromise between signal detection efficiency and dynamic range. The light yield combines all calibration ingredients, namely the already mentioned MIP calibration, the gain and the electronic intercalibration factor.

The light yield is determined for each of the SiPM-tile systems on a test bench. As shown in figure 6.12(a), the average light yield of 8096 produced cells is 16.6 pix/MIP with an root mean square (rms) spread of 3.6 pix/MIP. The cells closest to 15 pix/MIP are selected for the AHCAL. However, the light yield measured in-situ is found to be lower. During the August 2006 data taking period the average light yield, plotted in figure 6.12(b), is just 8.2 pix/MIP with an rms of 3.1 pix/MIP. The first SiPM bias voltage estimate had not taken into account the voltage drop over the several metres of cable between the AHCAL and the power supply. Consequently, the SiPM bias voltage was raised by 600 mV after the August 2006 data taking period. Illustrated in figure 6.12(c) is the average light yield during the 2007 data taking. It reached 13.3 pix/MIP with an rms of 2.4 pix/MIP, which is still below the design value. The

(a)   (b)   (c)
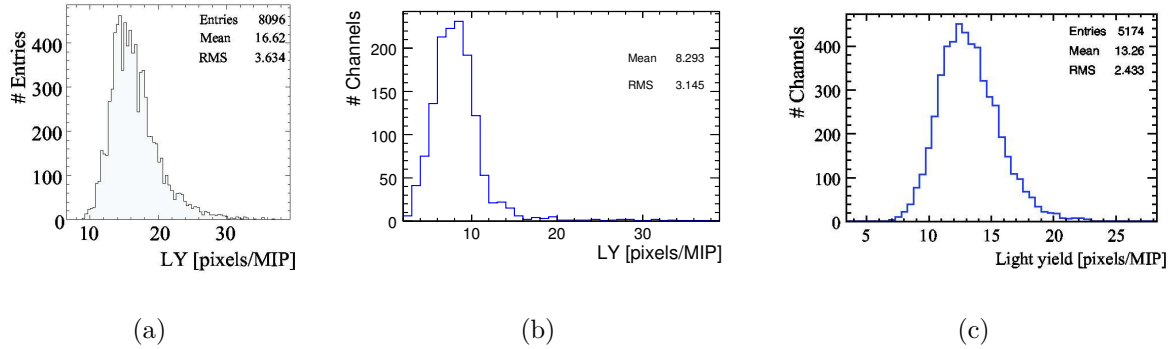
Figure 6.12: Light yield of the AHCAL (a) before installation from a test bench measurement [108], (b) during the August 2006 and (c) during the July 2007 data taking period.

main reason for this discrepancy is the temperature increase during the test beam period.

As explained in section 6.2.2, the SiPM properties depend on the temperature and the voltage. Thus, a given set of calibration constants is only valid for measurements at the same operation conditions. While the gain constants are recorded periodically over the full data taking period, MIP constants are only determined in dedicated muon runs taken before, or after the analysed data set. As shown in figure 6.13, the positron data were recorded at $2.5\,°C$ warmer conditions than the applied muon calibration run in the summer 2007 period.

The voltage and temperature dependencies can be measured, and the calibration constants, as well as the data, can be extrapolated to a defined temperature. Applying this temperature correction yields 12 % higher energies with respect to the uncorrected calibration constants [122].

In principle the light yield drop due to the temperature increase could be compensated by an increase of the SiPM operation voltage. However, an increased bias voltage would also increase the SiPM noise (cf. section 6.2.2). Therefore, an operation at reduced light yield was chosen for the summer 2007 data set.

6.4 Experience from Minical

The Minical [114] is a small prototype of a highly granular hadron calorimeter. Just as the AHCAL it has a scintillator iron sandwich structure with 2 cm absorber plates and 0.5 cm thick scintillating tiles. Each layer consists of a 3×3 matrix of $5.0 \times 5.0\,cm^2$ wide tiles. A full-circle-shaped WLS fibre embedded in each tile guides the light to the photodetector, a SiPM with 1024 pixels. Compared to the AHCAL, the Minical SiPMs have a smaller quenching resistor and thus a shorter recovery time. Therefore, a pixel can be fired several times during the registration time and the saturation level, plotted in figure 6.7 is at 2000 effective pixels.

The Minical has been exposed to $1-6\,GeV$ positrons in the DESY test beam. To correct for the SiPM saturation behaviour, equation 6.5 is applied. The reconstructed energy

(a)   (b)
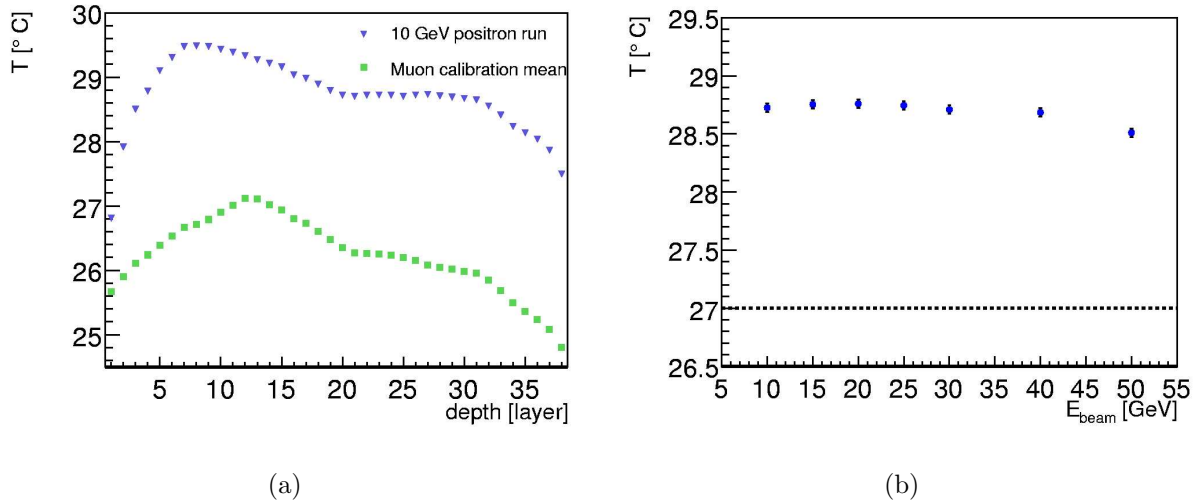
Figure 6.13: AHCAL temperature [122] (a) layer-wise profile in a 10 GeV positron run
(blue triangle) and during a muon calibration run (green squares), and (b)
development during the positron data taking period.

(a)   (b)
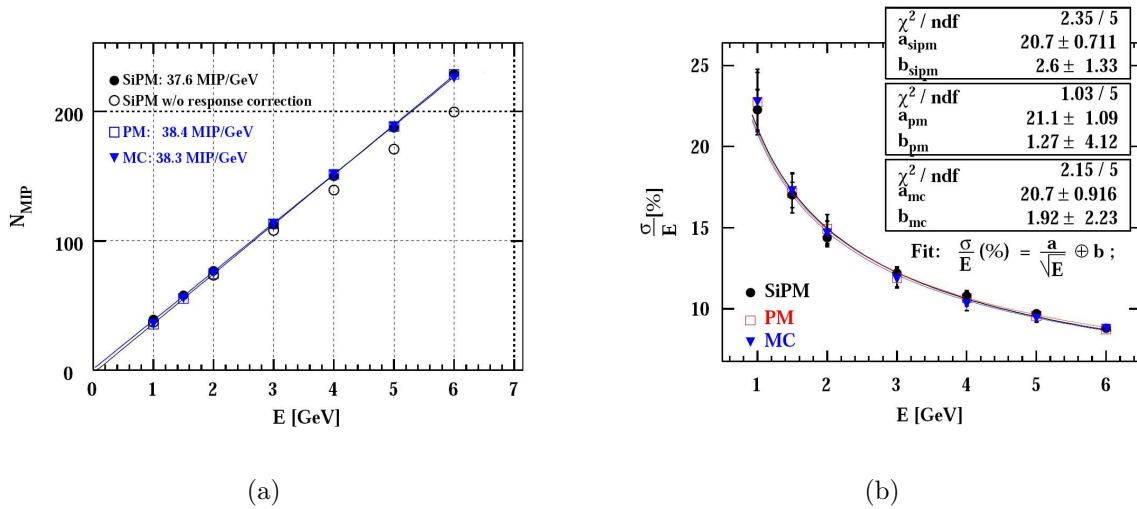
Figure 6.14: Response of the Minical calorimeter to low energetic positrons [114]. (a)
Total signal, normalised to the number of MIPs as a function of the beam
energy. (b) Measured energy resolution for SiPMs (circles), photomultiplier
tubes (squares) and Monte Carlo (triangles).

with and without non-linearity correction is plotted in figure 6.14(a) as a function of
the beam energy. The achieved linearity with non-linearity correction is better than
2 % for the energy range under investigation. The energy resolution is measured to be

$$\frac{\sigma_E}{E} = \frac{(20.7 \pm 0.7)\,\%}{\sqrt{E\,[\mathrm{GeV}]}} \oplus (2.6 \pm 1.3)\,\%. \tag{6.6}$$

The results derived with SiPM readout agree with measurements performed with con-
ventional photomultiplier readout and Monte Carlo simulations.

The parametrised formula stated in equation 6.5 with one fixed number of N_{max} for all SiPMs is sufficient to correct for the SiPM saturation in the energy range investigated by the Minical. One simple function to describe the whole detector simplifies the calibration. Thus, it is also used as a first guess to correct the electron dataset recorded with the AHCAL, which covers electrons and positrons from $E_{\mathrm{beam}} = 6 - 50\,\mathrm{GeV}$.

7 Electromagnetic Analysis

Although the analogue hadron calorimeter prototype is designed to measure hadrons, a look at the electromagnetic scale serves as a calibration validation. First the prototype is calibrated with electromagnetic showers, and all its characteristics are properly investigated. Afterwards, it is possible to go ahead and use the well understood detector to explore the yet unknown physics of hadronic shower propagation.

7.1 Data Taking

This contribution focuses on the performance of the AHCAL detector on the electromagnetic scale. The data taking conditions, and the investigated data sample are introduced in the following.

The AHCAL configuration in August 2006 is referred to as AHCAL-15, while AHCAL-38 denotes the July 2007 setup. Positrons are chosen in the AHCAL-15 configuration, while electrons are under investigation for the AHCAL-38 configuration.

7.1.1 Beam Line

The data discussed in the following have been collected in August 2006 and in July 2007 at the CERN test beam facility H6b at the Super Proton Synchrotron (SPS). The SPS is a 6.9 km circumference proton accelerator, operated at momenta up to 450 GeV. The proton beam is steered at a beryllium target to provide a secondary beam of various kinds of charged and neutral particles with up to ± 205 GeV, where the sign indicates the polarity of the beam particles, to the H6 facility. Typically, H6 runs at ± 205 GeV or ± 120 GeV and tertiary beams range from ± 5 GeV to ± 80 GeV. An electron- or positron-enriched tertiary beam can be obtained by introducing a lead secondary target. The momentum selection is performed by a magnetic spectrometer located behind the secondary target, and can range between 205 GeV and 5 GeV with decreasing beam rate.

The CALICE installation at the H6 test beam facility is sketched in figure 7.1, where the beam is going from left to right. Apart from the CALICE calorimeter prototypes, the beam installation consists of various trigger and beam monitoring devices. Although the tertiary beam is electron enriched, it still contains pion and muon contamination. The beam first passes a Čerenkov counter, which can be used to discriminate between electrons (positrons) and pions. Afterwards the coincidence of two scintillator triggers (Sc) of 10×10 cm^2 size each, is used to trigger the DAQ. Additional scintillator triggers of different sizes can be used to select events. Three delay wire chambers (DWC) provide additional information about the beam position. During the runs analysed in this thesis, the analogue hadron calorimeter (AHCAL) and the tailcatcher and muon
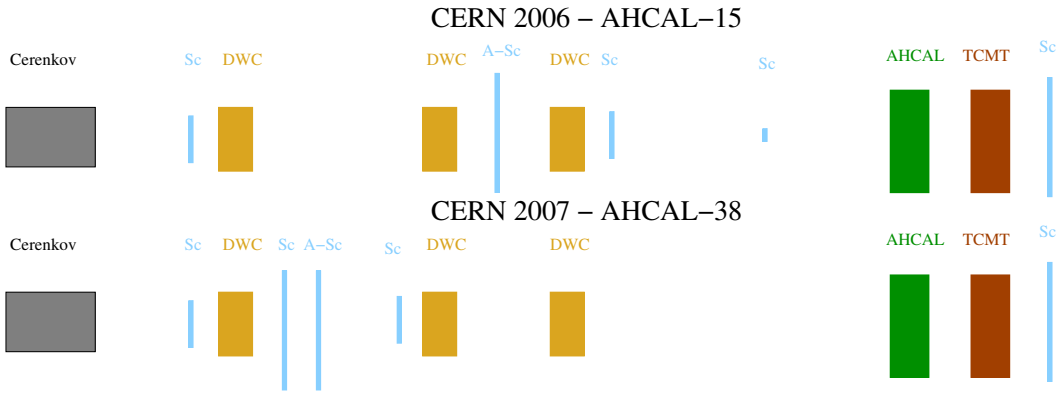
Figure 7.1: Top view of the CALICE beam line instrumentation in August 2006 (AHCAL-15) and in July 2007 (AHCAL-38). Sketch is not to scale.

tracker (TCMT) were present. During most of the rest of the test beam periods, a silicon tungsten electromagnetic calorimeter (Si-W ECAL) was placed in front of the AHCAL. The Si-W ECAL is moved out of the beam line for the analysed data set, because otherwise the electrons would not reach the AHCAL. The beam instrumentation is presented in some more detail in the following. A comprehensive description of the CALICE test beam installation and data taking is presented in [119].

7.1.2 Trigger System

A coincidence of two scintillator plates (Sc) with $10 \times 10\,\text{cm}^2$ area, read-out with fast photomultiplier tubes, serves as a beam trigger. The plates are arranged at a distance of roughly $2.5\,\text{m}$, which restricts the accepted beam trajectory.

For one dedicated scintillator plate (A-Sc) with $20 \times 20\,\text{cm}^2$ area, the analogue signal is recorded in addition to the digital one. This information can be used to identify double particle or pre-showered events, and therefore this scintillator is referred to as multiplicity counter.

A $100 \times 100\,\text{cm}^2$ sized scintillator plate is placed behind the TCMT. The only particles that can pass all detectors without being stopped are muons. Thus, a signal in this last scintillator plate is used to reject muon contamination.

In the AHCAL-15 configuration an additional scintillator trigger with $3 \times 3\,\text{cm}^2$ area was placed close to the AHCAL surface. It only triggers on the central beam, and consequently can help to reject the beam halo.

7.1.3 Particle Identification

A threshold Čerenkov counter allows for particle identification and separation. It is basically an $11\,\text{m}$ long helium vessel, situated $25\,\text{m}$ upstream of the experimental area. Charged particles traversing any material emit Čerenkov light, if they travel faster than the speed of light in the according medium. The Čerenkov counter gas pressure is tuned such that traversing pions do not generate a signal, but electrons do. The threshold pressure decreases with increasing particle momentum, thus it has to be adjusted to

<div align="center">(a)   (b)   (c)</div>
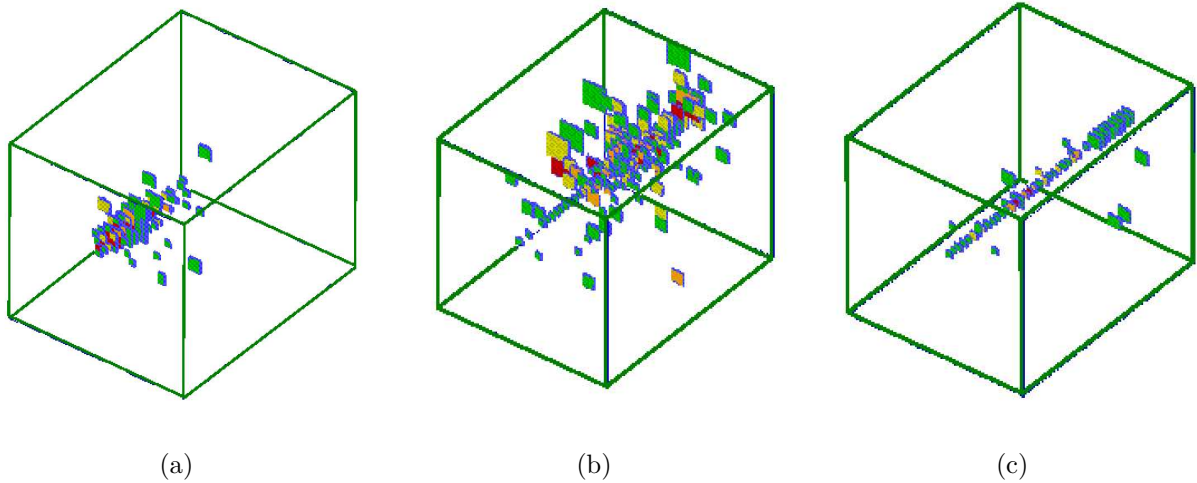
Figure 7.2: Event display of a 30 GeV (a) positron, (b) pion and (c) muon identified event of the same run. See text for further explanation.

the beam momentum. However, this cannot be done down to arbitrarily low values. As a consequence, the electron identification efficiency drops with increasing energy. At 20 GeV the efficiency is just $\approx 30\%$. The chosen pressure varies from 8.4 bar at 6 GeV beam momentum and 0.8 bar for 20 GeV and higher beam momentum.

An example for particle identification in a 30 GeV positron run is shown in figure 7.2. It is performed with the Čerenkov counter, to discriminate between positrons and pions, and the scintillator trigger behind the TCMT, to identify muons. The event displays show a particle identified as positron (with the typical compact shower), pion (with a deeper and wider shower) and muon (leaving a straight track) in the AHCAL.

As this analysis investigates electron and positron induced showers, the Čerenkov counter is required to give signal, which implies that light is detected. The fraction of selected events for the investigated data set is quoted in table 7.2.

Since the e/π-ratio of the AHCAL is approximately 1.2 to 1.3, a remaining pion contamination would be visible as tail to the left of the energy sum distribution. As shown in figure 7.3, the energy sum spectra have a Gaussian shape at all beam energies, thus the electron sample can be assumed to be reasonably pure.

7.1.4 Particle Tracking

The exact impact point of beam particles is measured by three delay wire chambers (DWC) with time-to-digital-converter (TDC) readout. They consist of two layers with 128 signal wires of 25.4 cm length per plane. As the wires of one plane are arranged horizontally, while the wires of the complementing plane are arranged vertically, each DWC provides one x and one y coordinate. This results in three reconstructed space points, with a resolution better than 200 μm, which are fitted by a straight line to extrapolate the beam impact point on the AHCAL surface.
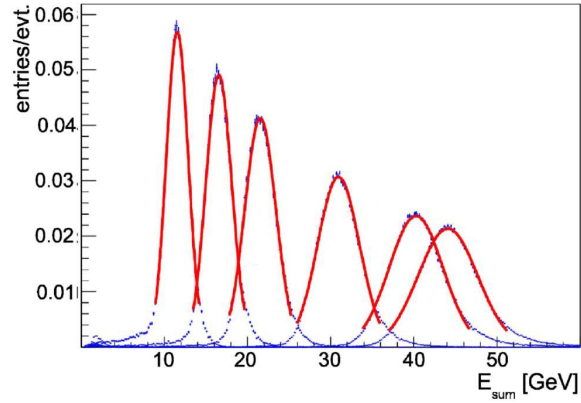
Figure 7.3: Reconstructed energy sums for the investigated electron data together with a Gaussian fit.
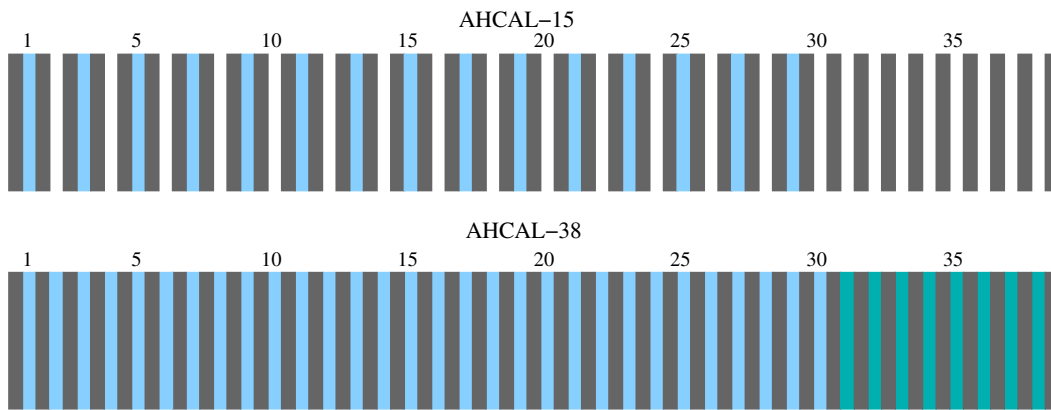
Figure 7.4: AHCAL instrumentation in August 2006 (AHCAL-15) and in July 2007 (AHCAL-38). The grey structure represents absorber plates, the light blue strips indicate cassettes with highly-granular instrumentation (layers 1-30), while the turquoise strips illustrate cassettes with coarse instrumentation (layer 31-38).

7.1.5 AHCAL Configuration

The AHCAL is designed as a sandwich structure with 38-layers. However, during the August 2006 data taking period only 15 highly granular active AHCAL cassettes (cf. section 6.2.1) had been produced, hence the denotation AHCAL-15. All 15 cassettes together comprise 3240 read-out channels. As indicated in the upper part of figure 7.4, every second AHCAL-15 layer was equipped with cassettes, and the last 6 layers were left completely uninstrumented. This constellation yields a depth of $31.9 \, X_0$, or $3.4 \, \lambda_i$, which is already sufficient to contain electromagnetic showers.

In July 2007 all 38 active cassettes had been finished, thus the designation AHCAL-38, and the prototype was operated fully equipped. This is sketched in the bottom part of figure 7.4, where the last eight layers have a coarser instrumentation with 141 scintillating tiles per layer. The AHCAL-38 depth is $48.0 \, X_0$, or $5.3 \, \lambda_i$.

<div align="center">(a)   (b)</div>
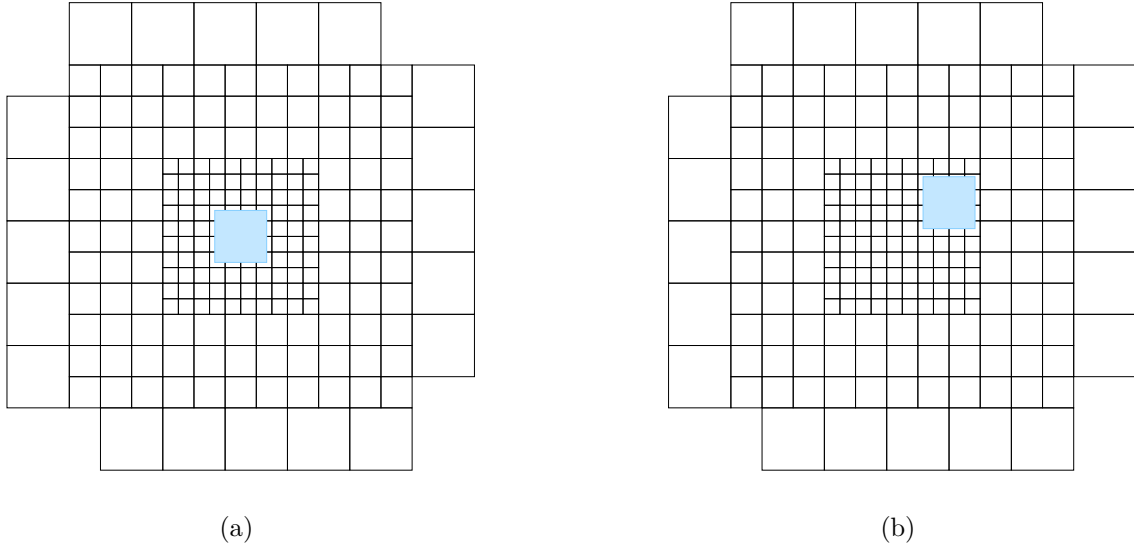
Figure 7.5: Trigger plate position with respect to the AHCAL surface (a) for the AHCAL-15 and (b) the AHCAL-38 configuration.

		AHCAL-15	AHCAL-38
N_{layers}		15	38
N_{cells}		3240	7608
position	cm	$(0.0; 0.0)$	$(-8.8; 6.2)$
depth	λ_i	4.7	5.3
	X_0	45.6	48.0

Table 7.1: Differences between the two investigated AHCAL configurations.

Furthermore, the AHCAL-38 is situated on a movable stage. This allows to shift the detector vertically and horizontally, as well as to rotate it up to approximately 28° with respect to the incident beam. Thus, the stage enables data taking at various beam impact positions and angles. While the beam is centred to the middle of the AHCAL-15 constellation, the AHCAL-38 is shifted 8.8 cm to the left and 6.2 cm down with respect to the beam axis. As illustrated in figure 7.5, the beam hits the highly granular core in both cases. Nevertheless, different cells contribute to the electromagnetic shower. This should not make any difference, if the calibration procedure works correctly. Thus, the different impact positions serve as a validation of the calibration quality. The differences between the investigated configuration sets are summarised in table 7.1.

7.2 AHCAL-15 Performance

The basic reconstruction scheme, with special emphasis on the non-linearity correction, is discussed on the example of the electron data set recorded in August 2006 in the AHCAL-15 configuration.

E_{beam} [GeV]	Run No.	# Beam Evts.	# Selected Evts.	Fraction Selected Evts.
6	320605	$95,554$	$78,962$	$82.6\,\%$
10	320678	$367,601$	$351,861$	$95.7\,\%$
15	320671	$309,751$	$301,598$	$97.4\,\%$
20	320666	$318,012$	$306,319$	$96.3\,\%$
30	320665	$452,948$	$308,205$	$68.0\,\%$
40	320664	$355,798$	$102,571$	$28.8\,\%$
45	320660	$236,037$	$62,989$	$26.7\,\%$

Table 7.2: Investigated electron data set in the AHCAL-15 configuration. Stated are the number of beam events and the fraction of selected events for every beam energy.

7.2.1 Data Sample

Each run is a collection of several ten thousands of beam events of a distinct particle type and energy. In addition, 500 random trigger events, serving as an electronic pedestal reference, and 500 events with constant light amplitude from the calibration and monitoring system, to monitor the detector stability, are recorded periodically within each run.

To avoid any systematic bias, and to keep results from both investigated test beam periods comparable, the event selection is kept as simple as possible. In this analysis, the $10 \times 10\,\text{cm}^2$ beam trigger is demanded on. This decision rejects pedestal and calibration events. In addition, the $100 \times 100\,\text{cm}^2$ trigger plate is demanded off to reject possible muon contamination. The efficiency of the Čerenkov counter drops with increasing particle energy, thus it also rejects an increasing amount of electrons. Nevertheless, to gain an as pure as possible sample, and as the analysis is not limited by statistics, it is demanded to tag electrons.

The selected number of events per run is summarised in table 7.2. More than sixty thousand electron events are selected for each beam energy. With increasing beam energy the electron selection efficiency decreases due to the decreasing Čerenkov counter efficiency described above.

7.2.2 Noise Contribution

Besides beam events, random trigger events are collected. They serve as a pedestal reference, since the pedestal is defined as the mean signal amplitude per cell during random trigger events. In addition to the electronic noise, one has to account for the SiPM dark rate of few kHz (cf. section 6.2.2). These events are reconstructed in the same way as beam events so that they can be subtracted from the beam events in later reconstruction steps. In addition they can be used to monitor the stability of the AHCAL in time.

The total number of random trigger events above threshold during a 30 GeV electron run with the AHCAL-15 configuration is shown in figure 7.6(a). The energy deposition

(a)   (b)
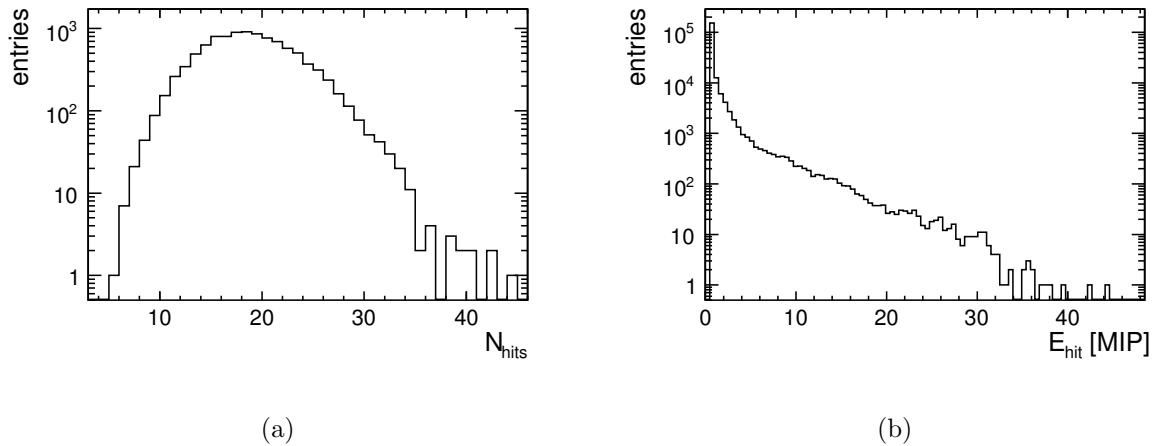
Figure 7.6: Noise in the AHCAL-15 during a 30 GeV electron run. (a) Number of noise
hits summed over the AHCAL-15 and (b) energy deposition per noise hit.

per random trigger hit during a 30 GeV electron run is plotted in figure 7.6(b). Averaged over the entire investigated AHCAL-15 run period, $N_{\text{hits}}(\text{noise}) = 18.96 \pm 0.03$ noise hits per event deposit a total of $E_{\text{sum}}(\text{noise}) = 38.3 \pm 0.3\,\text{MIP}$ in the full AHCAL-15. Distributed over 3240 cells, this results in 1.3 noise hits per layer, or a detector occupancy of $6 \cdot 10^{-3}$. The design goal is a detector with a occupancy below $1 \cdot 10^{-4}$. Since the applied SiPMs turned out to be noisier than expected, the SiPM selection criteria had to be relaxed to gather a large enough sample. The expected detector occupancy is therefore $3 \cdot 10^{-4}$. The noise contribution in the AHCAL-15 configuration is considerably higher than the design goal and also than the expected occupancy. It could be reduced later on (cf. section 7.6.1).

Cells with a pedestal width below 50 ADC channels are considered to be dead. The main reason for this are bad soldering connections. Furthermore, channels without successful MIP calibration are excluded from the analysis. Several channels show very noisy behaviour, and thus cannot be calibrated. The reason for this are scratches on the SiPM surface that appeared during the assembly and the transportation. In the AHCAL-15 configuration 3.8 % of all channels are excluded from the analysis. As shown in figure 7.7, they are randomly distributed over the full calorimeter volume. As explained in section 4.3.5 these dead channels contribute to the leakage and thus reduce the detector performance.

7.3 Data Reconstruction

For every event that passed the trigger criteria listed in section 7.2.1, the pedestal-subtracted amplitude is calibrated to the pixel scale, as described in section 6.3.3. The resulting amplitude in pixels is corrected to a linear scale with one of the saturation correction methods discussed in section 6.3.3. Afterwards, it is transformed to the MIP scale. Every hit smaller than 0.5 MIP and all hits in uncalibrated cells are removed. The resulting energy loss is not compensated for. The AHCAL-15 has two different sampling fractions (cf. section 4.1), since there is only one absorber plate in front of the
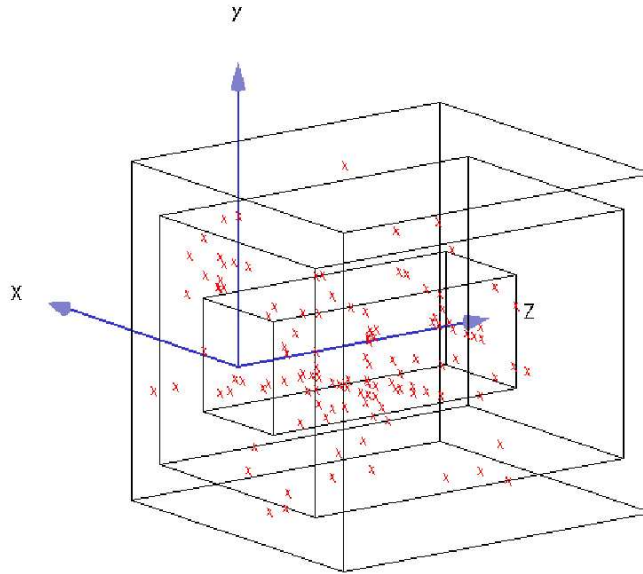
Figure 7.7: Spatial distribution of cells excluded from the AHCAL-15 analysis. The black boxes represent the outer boundaries of cells with $3\,\mathrm{cm}^2$, $6\,\mathrm{cm}^2$ and $12\,\mathrm{cm}^2$ cell size.

first active layer, but two absorber plates in between all consequent active layers. To account for this difference, the remaining hits are scaled with a factor of 1 for the first layer and a factor of 1.78 for all other layers. The factor of 1.78 results from the fact that the absorber plate thickness is only approximately $1.6\,\mathrm{cm}$ and the active layers add another $0.4\,\mathrm{cm}$ steel for each cassette.

As electromagnetic showers are dense and yield high single-hit energy deposition, special attention is given to the non-linearity correction of the SiPMs. The different correction mechanisms, introduced in section 6.3.3, are compared in this section. Furthermore, several parameters influencing the non-linearity correction are investigated using the example of the parametrised correction (cf. section 6.4).

7.3.1 SiPM Non-Linearity Correction

Influence of the Effective Number of Pixels   The dominant free parameter entering the non-linearity correction is the effective number of available pixels N_{max}. The impact of the effective number of pixels on the non-linearity correction is illustrated in figure 7.8(a), which shows the energy deposition per hit in MIP of a $30\,\mathrm{GeV}$ electron run. The blue line represents data without any saturation correction, while the other curves are obtained by applying the parametrised correction, stated in equation 6.5, with $N_{\mathrm{max}} = 1250$, 1000 and 833 pixels, respectively.

The more pixels are available in total, the smaller the non-linearity correction. This behaviour is expected, since less available pixels lead to earlier saturation and thus larger correction factors. Figure 7.8(b) shows the reconstructed energy as a function of the beam energy. At $45\,\mathrm{GeV}$, the energy reconstructed without saturation correction deviates by more than $30\,\%$ from the incident beam energy. The comparison of the

(a) (b)
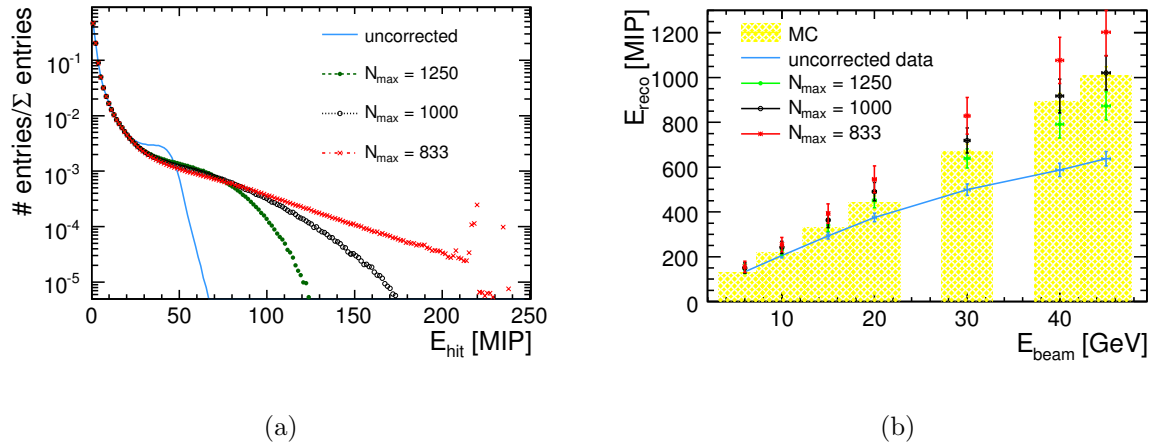
Figure 7.8: (a) Hit energy spectrum for a $30\,\mathrm{GeV}$ e^- run with parametrised correction assuming a different amount of effective pixels: $N_{\mathrm{max}} = 1250$ (green filled dots), 1000 (black open dots) and 833 (red crosses) pixels. (b) Reconstructed energy as a function of beam energy for a different amount of effective pixels and Monte Carlo (yellow area).

(a) (b)
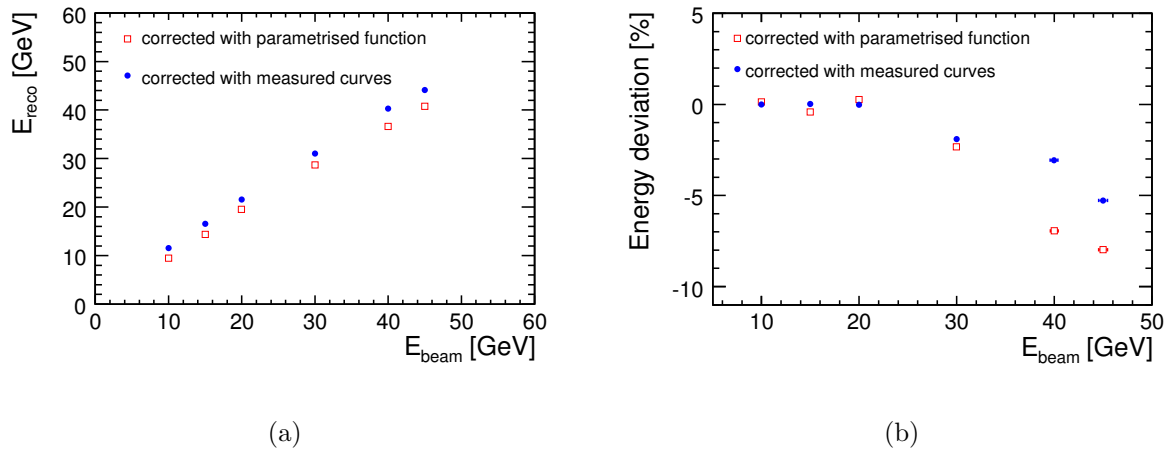
Figure 7.9: Comparison of SiPM non-linearity correction with a parametrised function (filled blue dots) and the measured test bench curves (open orange circles): (a) reconstructed energy sum and (b) deviation from linearity as a function of the beam energy.

effective number of pixels to the simulation illustrate that the best agreement between data and simulation can be achieved for $N_{\mathrm{max}} = 1000$.

Comparison of Correction Methods Possible non-linearity correction methods are discussed in section 6.3.3. To judge which method works best, they are applied to data. Figure 7.9 illustrates the linearity achieved for the AHCAL-15 electron data set corrected by the parametrised function and the method based on test bench measurements. The global energy scale, i.e. the conversion from MIP to GeV, is fixed by
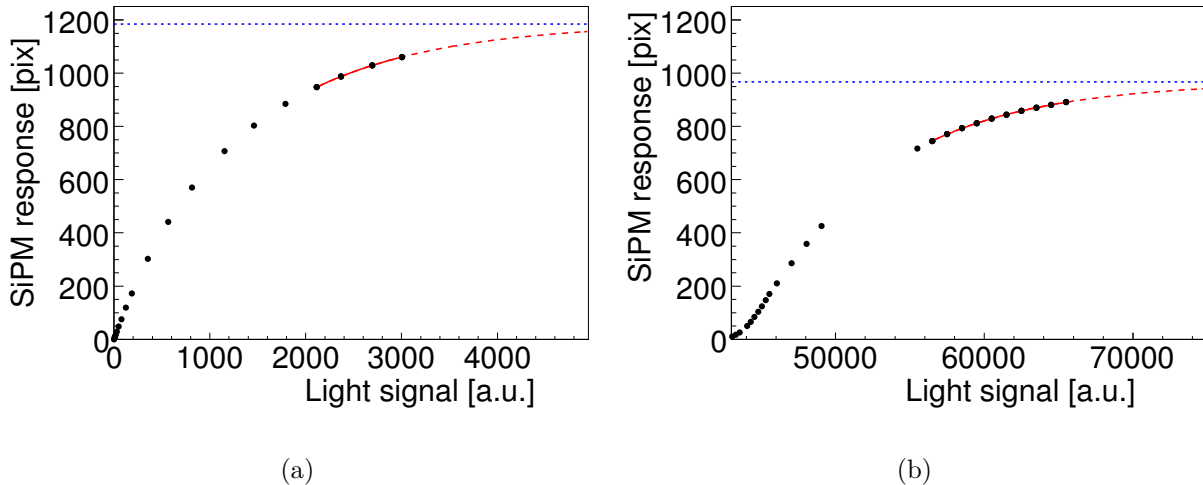
Figure 7.10: SiPM response curve measured [117] (a) on the bare SiPM from a test bench and (b) in-situ during the data taking period.

defining the difference in energy reconstructed for the 20 GeV and the 10 GeV beam energy to be exactly 10 GeV.

Figure 7.9(a) shows the reconstructed energy as a function of beam energy. The deviation from linearity is plotted as a function of the beam energy in figure 7.9(b), where linearity is defined as the straight line connecting the points at 10 GeV and 20 GeV beam energy.

The energy reconstructed with the parametrised function for the non-linearity correction deviates more than 8 % for a 45 GeV electron beam. The SiPM correction based on test bench measurements, has a remaining non-linearity below 6 % for a 45 GeV electron beam and hence will be used for all further studies.

The remaining non-linearity triggered the comparison of the test bench measured SiPM response curves with the in-situ measured ones [117], which revealed that the total number of firing pixels in the in-situ measurements, shown in figure 7.10(b), is on average 80 % lower than the laboratory setup measurements, shown in figure 7.10(a). The laboratory measurements are performed on the bare SiPM, illuminated by an UV LED via a fibre bundle. The in-situ measurements test the full process chain from scintillator via WLS fibre to the SiPM. Due to inefficiencies in the coupling from the 1 mm diameter WLS fibre and the 1 mm^2 SiPM surface not the full SiPM surface is illuminated. Therefore, currently the response functions from the laboratory response curves are rescaled before they are used to correct for the SiPM saturation behaviour. This re-scaling leads to higher correction factors, and thus improves the linearity at high energies. The re-scaling procedure had not been available at the time this analysis was performed and is not included in the presented results.

7.3.2 Inter-tile Optical Crosstalk

Although the scintillating tiles are chemically treated at the edges, a dedicated measurement with two tiles activated by a β-source found 2.5 % optical cross talk to each side [123]. This sums up to a total amount of 10 % light leakage for each tile to its

	produced light	detected light	calibrated signal
Muon	. . . / . 1.0 . / . . .	. 0.025 . / 0.025 0.9 0.025 / . 0.025 .	. . . / . 1.0 . / . . .
Electron	. 3.0 . / 2.0 40.0 3.0 / . 2.0 .	. 4.0 . / 3.0 36.0 4.0 / . 3.0 .	. 4.4 . / 3.3 40.0 4.4 / . 3.3 .

Figure 7.11: Schematic of the influence of inter-tile crosstalk on a MIP track and on an electron shower.

four direct neighbours. Besides redistributing energy, inter-tile crosstalk is an effective change of the MIP scale. Each MIP deposits an energy E_{MIP} in one scintillating tile, of which a fraction of k leaks to the neighbours. Thus, the effectively detected MIP signal is only $E_{\mathrm{MIP'}} = (1 - k) \cdot E_{\mathrm{MIP}}$.

The different influence of optical crosstalk due to the $0.5\,\mathrm{MIP}$ threshold is sketched in figure 7.11. Per definition, each MIP deposits an amount of energy with the most probable value peak at $1.0\,\mathrm{MIP}$ in one cell. Ten percent of this energy leaks to the neighbouring cells. The remaining energy in the central tile is calibrated to be $1.0\,\mathrm{MIP}$, the contribution in the neighbouring cells is neglected due to the threshold cut.

Electrons deposit their energy distributed over several cells. Again, the light leaks to the neighbouring cells and is calibrated with the measured (not crosstalk-corrected) MIP coefficient. In this case the neighbouring cells are already above threshold, and their energy is fully taken into account. Thus, due to the different definition of MIP used in the two cases, the estimated energy deposition in units of MIP' is higher than the originally deposited amount of energy in units of MIP.

The effect of inter-tile crosstalk on electron showers is illustrated in figure 7.12, which plots the ratio between reconstructed and simulated energy sum as a function of beam energy. The simulation used for comparison in this plot does not include any detector effects.

Correcting for crosstalk lowers the reconstructed energy by approximately the amount of the crosstalk. The applied correction of $10\,\%$ yields a much better agreement between data and Monte Carlo. The trend of a decreasing ratio between data and Monte Carlo towards higher beam energies reflects the insufficient non-linearity correction.

For the following analysis, optical crosstalk is not corrected for in data, but included in the Monte Carlo digitisation (cf. section 7.4.2) instead.
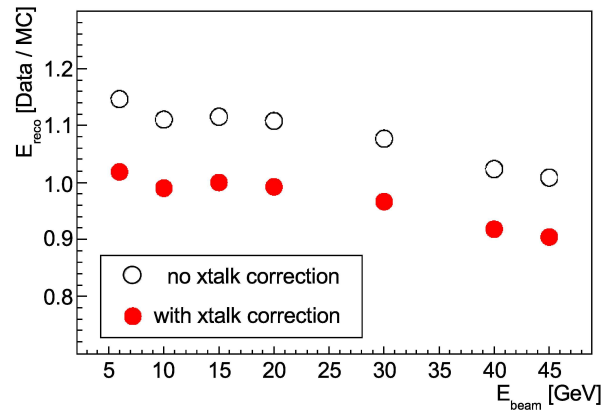
Figure 7.12: Ratio between recorded energy and Monte Carlo prediction as a function of beam energy, with and without inter-tile crosstalk correction. Shown are data events reconstructed with (red filled dots) and without (black circles) crosstalk correction.

7.3.3 Discussion of Systematic Uncertainties

As described in section 6.3.3, three calibration coefficients enter the energy calibration: the MIP, the gain and the electronics intercalibration factor. They are extracted from independent measurements, which are all affected by some systematic uncertainties.

The influence of the calibration coefficients on the energy reconstruction is investigated, to account for any systematic uncertainties in the determination, and the application of the calibration coefficients.

The uncertainty on the MIP scale has a direct impact on the reconstructed amount of energy. From comparison of different MIP selection and fitting methods, and temperature variations of the order of $1\,°C$ during the investigated data period, the total uncertainty on the MIP calibration is estimated to be $3\,\%$. The MIP coefficient has no direct influence on the relation between the number of incident photons and the number of recorded avalanches (cf. section 6.3.3).

A higher gain coefficient also leads to a smaller reconstructed energy and thus to a smaller non-linearity correction. The influence of a raised gain calibration on the non-linearity correction is much more pronounced than that of the MIP calibration, since the gain calibration directly enters the non-linearity correction. The influence of the electronics intercalibration factor is exactly opposite, a higher intercalibration factor leads to higher non-linearity correction factors. The combination of both measurements is stable on the percent level for the investigated data set. The relative uncertainty on the combined gain and electronics intercalibration factor is estimated to be $2\,\%$, accounting for the fit uncertainty and the temperature variations during the investigated data period.

Temperature effects are not corrected for in the presented analysis. Instead the resulting systematic uncertainties are propagated to uncertainties on the energy reconstruction, by applying artificially lowered (raised) calibration constants during the data reconstruction. The application of temperature corrections is expected to improve the systematic uncertainties.

Material	Density [g/cm³]	X_0 [cm]	Constituents	Mass Fraction [g/cm³]
Steel	7.87	1.76	Fe	0.984
			C	0.002
			Mn	0.014
Scintillator	1.03	41.30	H	0.500
			C	0.500
Reflective foil	1.07	41.05	H	0.500
			C	0.500
FR4	1.70	17.50	Si	0.181
			O	0.406
			C	0.278
			H	0.068
			Br	0.067
Cable-fibre-mix	0.12	224.28	air	0.009
			PVC	0.872
			polysterole	0.119

Table 7.3: AHCAL material composition in the simulation.

7.4 Simulation

The description of the full CALICE test beam setup, as sketched in figure 7.1, is implemented in the Mokka detector model `TBCern0806_01`. All physics runs are simulated using Geant4. The generated statistics is comparable to the number of events in the corresponding data run.

7.4.1 Detector Simulation

The steel of the absorber plates and the cassette covers is simulated as an alloy of 98.4 % iron, 1.4 % manganese and 0.2 % graphite. The scintillating tiles are represented by a 1×1cm² grid of polysterene. They are covered by reflective foil simulated as polysterole. The FR4 is simulated as a mixture of 40.6 % oxygen, 27.8 % carbon, 18.1 % silicon, 6.8 % hydrogen and 6.7 % bromide. The cable-fibre-mix is approximated by a 50.0 % hydrogen, 33.3 % carbon and 16.7 % chlorine mix. The composition of one AHCAL layer in the simulation is summarised in table 7.3.

Single particles of defined type and energy are generated by the built-in particle gun of Geant4. The gun is positioned upstream of the Čerenkov detector and simulates a beam in exact z-direction with a lateral Gaussian profile with 25 mm width. The full beam line instrumentation, from the Čerenkov counter to the AHCAL, are considered for realistic pre-showering behaviour.

7.4.2 Digitisation

For a realistic comparison of measured data and Monte Carlo simulation, the simulated events are adapted to the data taking conditions. In other words, the simulation is

digitised such that simulation and data can both be treated in the same way during all further calibration and reconstruction steps. The digitisation procedure takes into account

- the detector granularity,

- light cross-talk between neighbouring tiles,

- non-linearity and statistical fluctuations on the pixel scale,

- SiPM and readout electronics noise.

The simulated active detector layers are assumed to have a uniform granularity of $1 \times 1\,\mathrm{cm}^2$ cell size. To simulate the actual geometry of the AHCAL-15, the signal amplitude of 9 (36, 144) of these virtual cells is summed up to obtain the actual geometry with 3×3 (6×6, 12×12) cm^2 cells.

Light cross-talk between neighbouring cells is simulated assuming that $10\,\%$ of the amplitude leaks homogeneously through the four edges of each tile and takes into account the fraction of circumference shared with the neighbours (cf. figure 7.5).

To simulate the non-linearity effects of the photosensors, the energy deposition is translated from GeV to the number of fired SiPM pixels. For this, an intermediate step is to convert the amplitude simulated in units of GeV to MIP equivalents. The conversion factor is estimated from the simulation of a $100\,\mathrm{GeV}$ muon beam in the AHCAL-15. It is found to be $955\,\mathrm{keV/MIP}$, accounting for the effect of light crosstalk. The amplitude in units of MIPs is then converted into pixels, using the measured light yield of each individual channel. On this scale the measured SiPM response curves from the test bench are used to simulate the SiPM non-linearity. Where not available, the curve of an arbitrary tile is applied.

If N_pix is the amplitude in pixels obtained this way and N_max is the saturation level of the individual channel, statistical effects are accounted for by generating a binomial random number with N_max repetitions and a probability of $N_\mathrm{pix}/N_\mathrm{max}$. The result is treated as the number of pixels firing for this specific event, and is translated back to the MIP scale with the channel-specific light yield.

At this stage, the Monte Carlo signal is equivalent to the response of the AHCAL to the energy deposited by particles in an event. However, both the electronic components and the SiPM dark current induce noise. This noise component is assumed to be completely independent from the physics amplitude in each channel and thus can be taken into account by overlaying each Monte Carlo event with a MIP-calibrated random-trigger-event.

After this step, simulated events are assumed to be equivalent to MIP-calibrated data and are treated the same way for all successive steps. A cell that could not be calibrated in the real detector for any reason, is also ignored in the simulation.

The digitisation effects are studied in detail with muon and electron simulations in [122]. Figure 7.13 shows the layer-wise energy deposition of a real muon and a simulated one with and without noise and missing cell digitisation in the AHCAL-38 configuration. Modelling the detector effects, clearly improves the agreement between data and Monte Carlo.
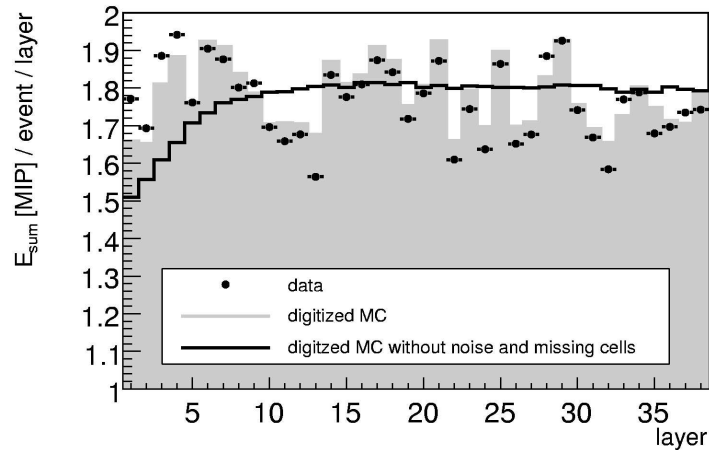
Figure 7.13: Layer-wise energy deposition of real muons (black dots) and digitised muon simulation with (grey area) and without (black line) noise and missing cell digitisation [122].

7.5 Comparison between Data and Monte Carlo

The number of hits above threshold and the hit energy spectrum for data and Monte Carlo are shown in figure 7.14. Simulated events show a systematic shift in the number of hits above threshold, which is not understood so far. At higher energies, there is a small excess of data around 30 hits, which is likely to result from a remaining muon contamination.

The hit energy spectrum shows excellent agreement between data and Monte Carlo, at least for beam energies up to 20 GeV. At higher beam energies, data still shows signs of non-linear behaviour, indicating that the saturation is slightly different from the behaviour used for correction.

The longitudinal profiles for beam energies of 10 GeV and 45 GeV are shown in the left columns of figure 7.15. The error bars account for both statistical and systematic uncertainties. The fit of the predicted shower curve (cf. equation 4.7) to data is shown as well. The comparison between profiles generated by data and Monte Carlo shows a reasonable agreement, especially in the tails. However, the shower in data tend to start earlier and be more compact than showers in Monte Carlo, which hints towards an underestimation of upstream material in the simulation.

Measuring the depth of each absorber plate at the end of the 2008 data taking campaign revealed that the absorber plates are not the expected 16 mm thick, but of varying thickness between 16 mm and 18 mm. Implementing the individual absorber plate sizes in the simulation leads to a good matching of the longitudinal shower development in data and simulation. The information on the true absorber thickness was not available at the time this analysis was performed and is not included in the presented results.

For low beam energies, the agreement is equally good along all layers of the calorimeter, while the shower maximum measured in data systematically lies below the Monte Carlo predictions. This pattern underlines the hypothesis of small remaining non-linear behaviour after correction, which is only expected to yield large effects for cells with high amplitudes occurring in the shower core.
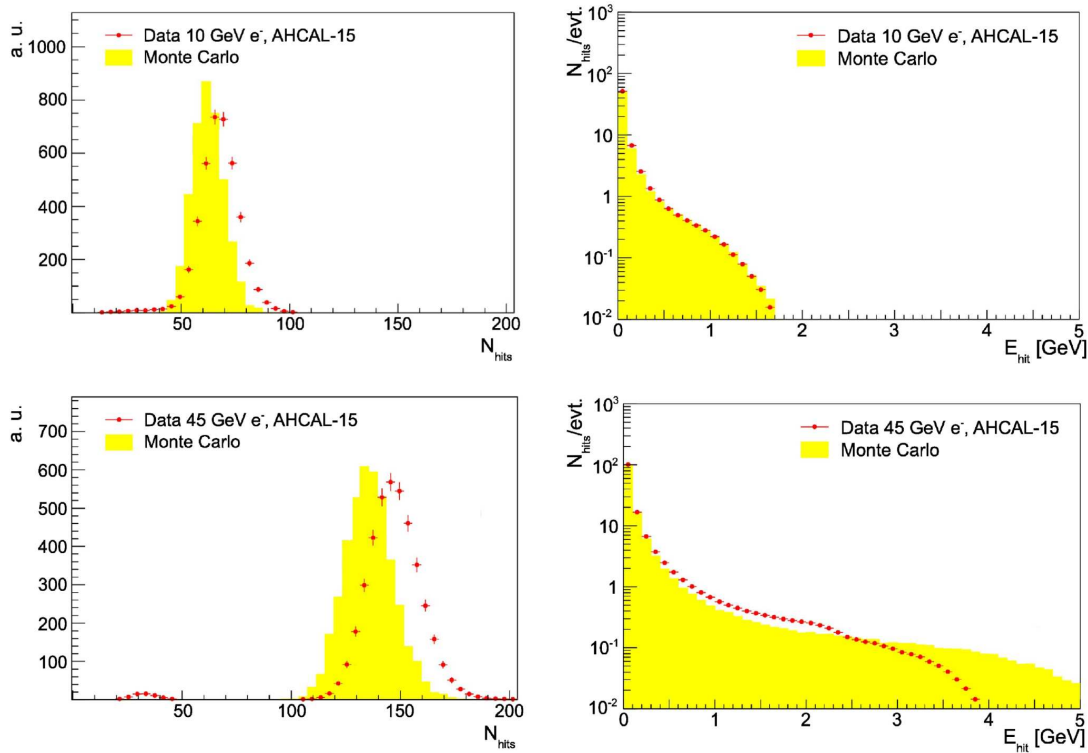
Figure 7.14: Comparison between data (red dots) and Monte Carlo (yellow area): 10 GeV electron run summed number of hits (upper left) and energy per hit (upper right). The same for a 45 GeV electron run in the lower row.

For the lateral shower profile, the two-dimensional centre of gravity of each event is calculated from the energy deposited in each tower, where a tower is defined as cells at the same x-y position in consecutive layers of the calorimeter. This point is systematically shifted due to the uncalibrated cells omitted in the analysis. However, uncalibrated cells are also excluded in the Monte Carlo and any systematic shift does not affect the shown comparison. In the right column of figure 7.15 the lateral shower shape is plotted as the distance-weighted energy sum over all towers with respect to the centre of gravity. The different number of cells in each ring and the growing area of the rings is not accounted for in the presented analysis. The centre of gravity from noise events does not agree with the one of beam events, thus the noise contribution extracted from random trigger events is not subtracted from the presented lateral profiles.

The exponential part of the profile merges with the flat background distribution at a radius of about 10 cm (16 cm) for 10 GeV (45 GeV) showers. The lateral shower shapes obtained from data and Monte Carlo are in reasonable agreement and compatible with the observations in the longitudinal profiles. Less reconstructed energy in data arises at low radii. As expected from the already mentioned remaining non-linearity, the effect is less pronounced at smaller beam energies.

The global energy scale, i.e. the conversion from MIP to GeV, is fixed by defining the difference in the reconstructed energy from the 20 GeV and the 10 GeV beam to be 10 GeV. The conversion factors of 33.3 MIP/GeV for data and 33.8 MIP/GeV for Monte Carlo are determined independently from each other and show good agreement.

The reconstructed energy sum of all runs and respective Monte Carlo simulations is
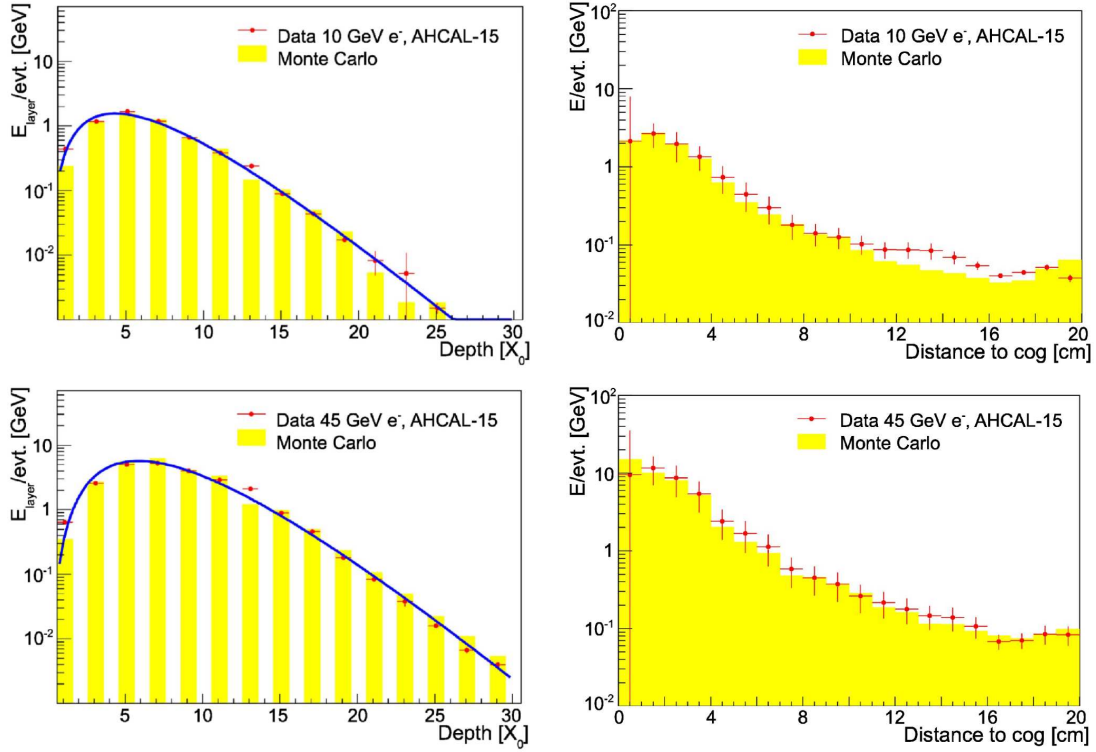
Figure 7.15: Comparison between data (red dots) and Monte Carlo (yellow area): longitudinal profile, including the fit on data (blue line) (left column), and lateral profile (right column) for a 10 GeV (upper row) and a 45 GeV (lower row) electron run.

(a)   (b)
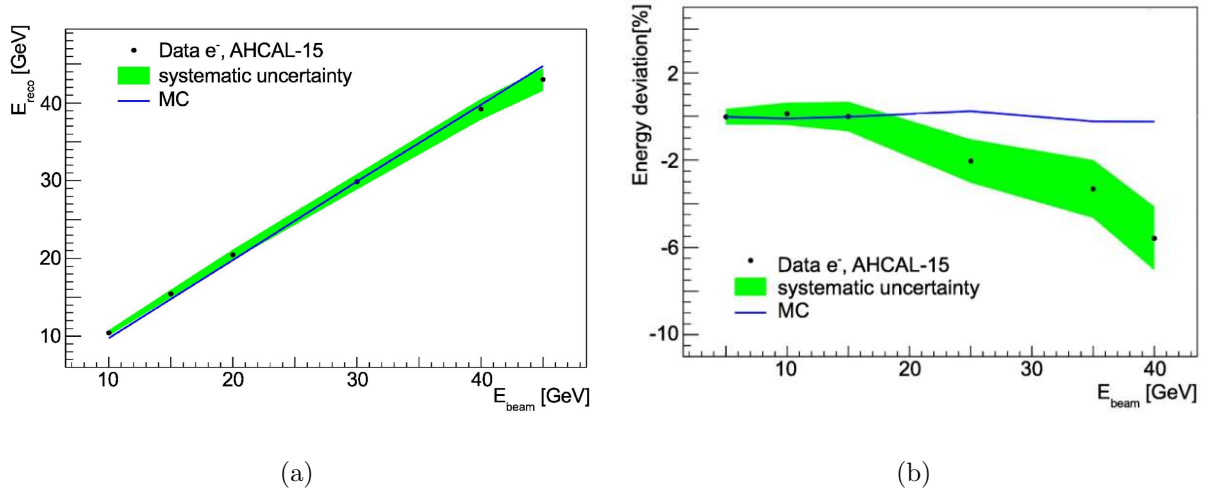
Figure 7.16: Comparison between data (black dots) and Monte Carlo (blue line): (a) Reconstructed energy vs. beam energy and (b) deviation from linearity for the AHCAL-15 data sample.

plotted against the nominal beam energy in figure 7.16(a). The green band indicates the uncertainty region for data resulting from statistical and systematic uncertainties on the MIP and the pixel calibration. The systematic errors are much larger than

E_{beam} [GeV]	Run No.	# Beam Evts.	# Selected Evts.	Fraction Selected Evts.
10	350118	114, 448	109, 411	95.6 %
15	350117	123, 095	117, 612	95.6 %
20	350114	89, 890	77, 728	86.5 %
25	350113	127, 270	88, 778	69.8 %
30	350132	88, 824	75, 305	84.8 %
40	350110	132, 490	18, 797	14.2 %
50	350128	129, 460	23, 989	18.3 %

Table 7.4: Investigated positron data set in the AHCAL-38 configuration. Stated are the number of beam events and the fraction of selected events for every beam energy.

the statistic ones. Figure 7.16(b) shows the deviation from linearity, where linearity is defined as the straight line connecting the points at 10 GeV and 20 GeV beam energy, respectively. As the uncertainty on the MIP coefficient drops out while building the ratio to a linear energy scale, the systematic error band only includes the uncertainty on the pixel scale in this plot.

The Monte Carlo shows no deviation from linearity, and the linearity for data is confirmed within 3 % (6 %) below 30 GeV (45 GeV) beam energy. The linearity as defined before exhibits an offset of −300 MeV for Monte Carlo and 400 MeV for data. This offset corresponds to a remaining noise contribution. Although the mean noise contribution, extracted from random noise trigger, is subtracted from data, statistical fluctuation can cause the remaining noise contribution.

7.6 AHCAL-38 Performance

The AHCAL has by now been operated for several months over four years. The stability of the detector performance over one year of operation is investigated by comparing the AHCAL-15 and the AHCAL-38 data set.

The positron data set collected in the AHCAL-38 configuration is summarised in table 7.4. Several ten thousand positron events are recorded for each beam energy. With increasing beam energy the electron selection efficiency decreases due to the decreasing Čerenkov counter efficiency already described for the AHCAL-15 data set in section 7.2.1. The calibration procedure is the same as for the AHCAL-15 data set.

7.6.1 Noise

The average number of hits and energy deposition by random trigger events is plotted as a function of the beam energy in figure 7.17. Averaged over the investigated run period, 6.94 ± 0.01 noise hits deposit 4.29 ± 0.01 MIP energy per event in the AHCAL-38 configuration. Distributed over 7608 cells this results in 0.2 noise hits per layer,

(a)   (b)
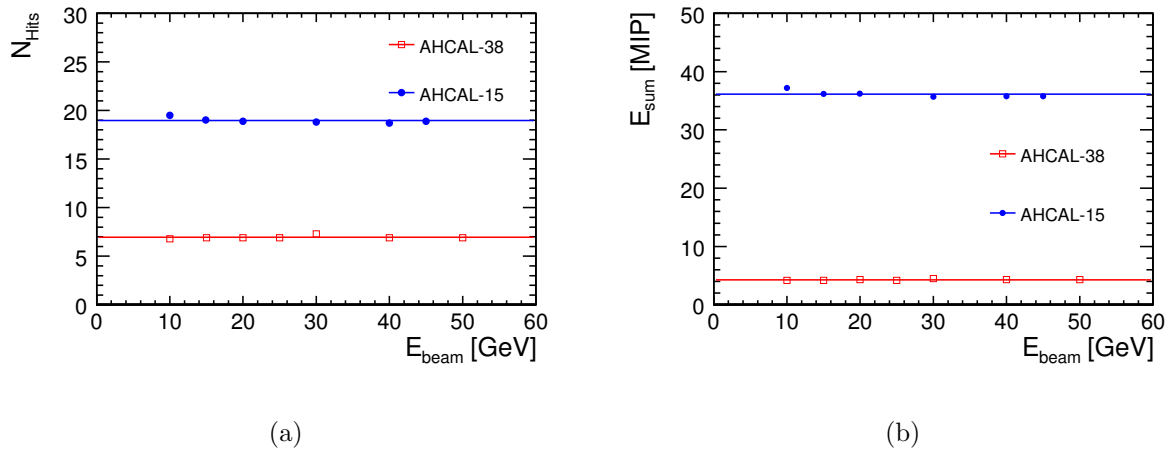
Figure 7.17: Noise in the AHCAL-15 (blue dots) and the AHCAL-38 (orange squares) as a function of beam energy: (a) sum of noise hits and (b) sum of energy deposited by noise hits.

or an occupancy of $1 \cdot 10^{-3}$. In total $1.6\,\%$ of all channels operated in the AHCAL-38 configuration are considered dead. Most of these cells have broken SiPM solder connections.

For the AHCAL-15 configuration, the noise occupancy is three times higher (cf. section 7.2.2). The same number of noise hits deposited the same amount of energy as in the AHCAL-38 configuration, but on one third of the cells. The high noise contribution during the AHCAL-15 configuration is due to coherent noise.

Coherent noise results in correlated fluctuations over all channels. It can occur if some electronic components are shared between readout channels. In this case the noise of each single channel consists of an independent contribution, as well as a coherent one. The coherent contribution is quantified by

$$\sigma_{\mathrm{coh}} = \frac{1}{N_{\mathrm{ch}}} \sqrt{\sigma_{\mathrm{dir}}^2 - \sigma_{\mathrm{alt}}^2}, \tag{7.1}$$

where N_{ch} is the number of contributing channels and σ_{dir}^2 describes the direct sum of all amplitudes while σ_{alt}^2 is the alternating one, i.e. the contribution of one half of all channels is subtracted from the contribution of the other half. Here the channels are divided into even ordering number and odd ordering number.

Figure 7.18(a) shows the correlation between the amplitude sum of even and odd ASIC channels during one noise run. A clear coherent pattern is visible. It could be reduced by the addition of $10\,\mu\mathrm{F}$ filtering capacitors on the supply voltage and the reference voltage line of each ASIC.

Before this intervention the electronics noise corresponded to 36 ± 2 ADC channels [121], while it is 17.7 ± 0.1 ADC channels after modifications. The coherent noise is reduced by a factor of six and the total noise by a factor two. The correlation of the amplitude sum of even and odd ASIC channels after modifications, given in figure 7.18(b), does not show any coherent pattern.

In the AHCAL-15 configuration, several SiPMs in the first two produced cassettes are very noisy. The reason for this are scratches, which cause short-circuits, on the
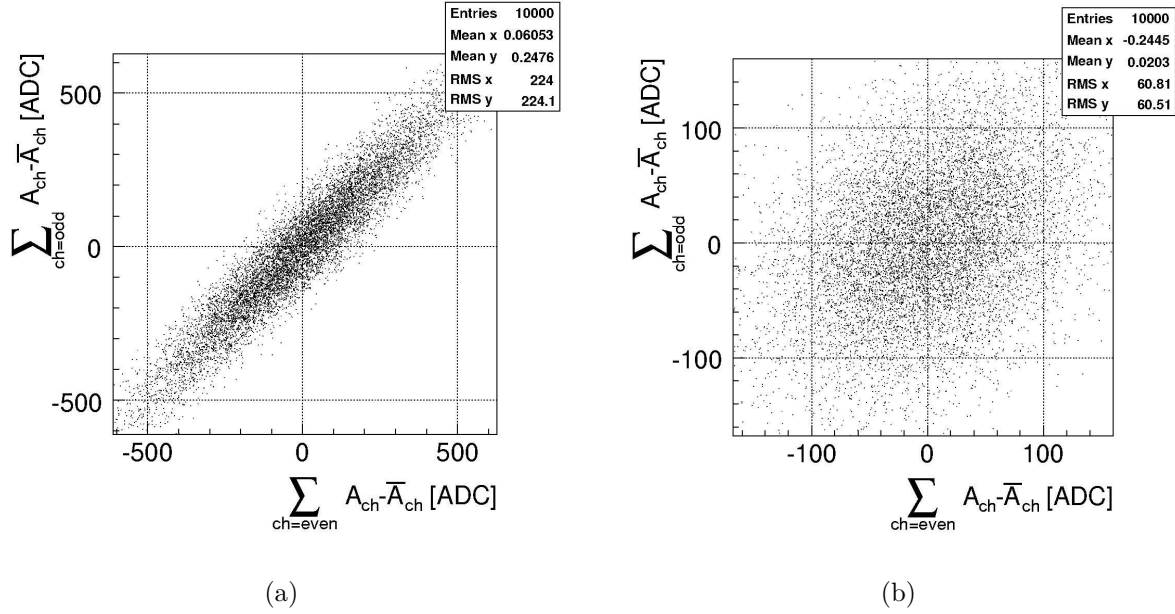
Figure 7.18: Noise amplitude of odd ASIC channels as a function of the noise contribution of even ASIC channels: (a) during the AHCAL-15 data taking period and (b) after hardware modifications.

SiPM surfaces. These scratches emerge during assembly and transportation. As a consequence, the SiPMs produced after the second cassette are covered by a thin surface protection (KO-08). The noisy SiPMs in the first two produced cassettes are replaced in the AHCAL-38 configuration.

7.6.2 Linearity

The global energy scale is fixed by defining the difference in the reconstructed energy from the 20 GeV and the 10 GeV beam to be exactly 10 GeV. The conversion factors for the AHCAL-38 configuration is 32.5 Mip/GeV. This factor agrees with the AHCAL-15 result within 2.5 %.

The reconstructed energy of all runs is plotted against the nominal beam energy for the AHCAL-15 and the AHCAL-38 configuration in figure 7.19(a). The deviation from linearity is shown in figure 7.19(a), where linearity is defined as the straight line connecting the points at 10 GeV and 20 GeV beam energy, respectively.

As expected, there is no visible difference between electron and positron data. The reconstructed energy sums of the AHCAL-15 and the AHCAL-38 data sets are in good agreement. The linearity is better than 3 % (8 %) below 30 GeV (50 GeV) beam energy.

7.6.3 Energy Resolution

The figure of merit in calorimetry is the energy resolution. It is estimated from the width over the mean of a Gaussian fit to the energy sum. The resolution achieved with the AHCAL-38 configuration is plotted as a function of the beam energy in figure 7.20.
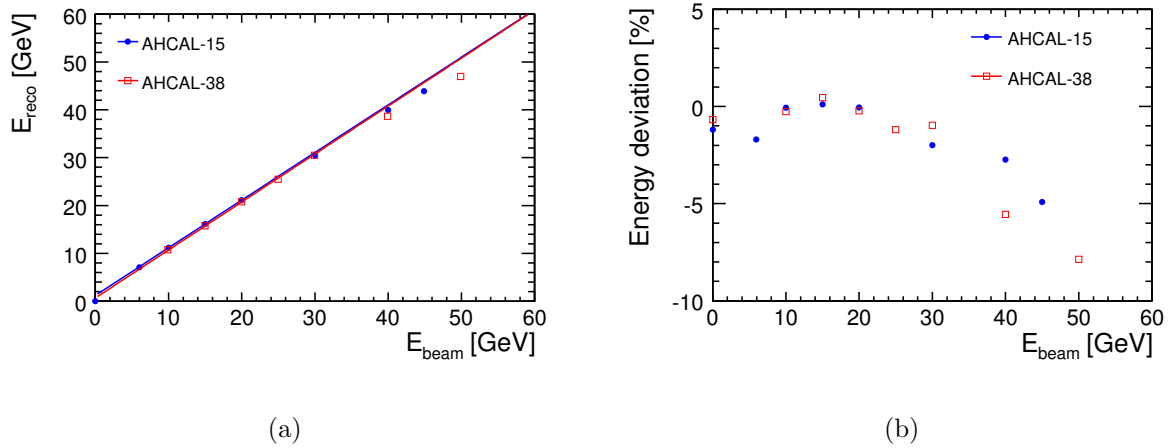
Figure 7.19: Electron data in the AHCAL-15 (blue dots) compared to positron data in the AHCAL-38 (orange squares): (a) reconstructed energy and (b) deviation from linearity as a function of beam energy.
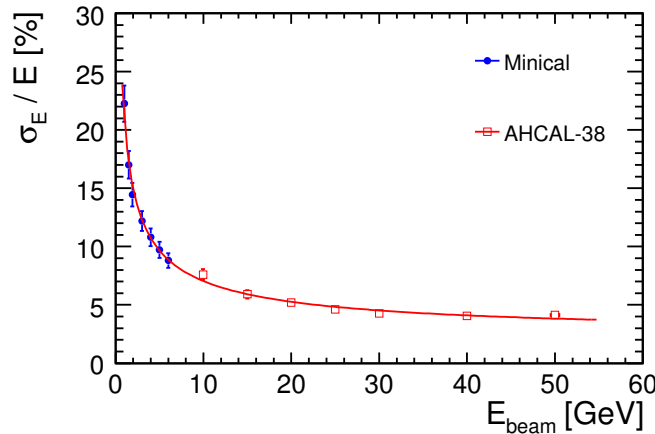
Figure 7.20: AHCAL energy resolution as a function of beam energy. Plotted are measurements from the Minical (blue dots) [114] and the AHCAL-38 configuration (red squares), as well as the fit to the AHCAL-38 measurements extrapolated over the full displayed energy range.

The resolution plotted above $10\,\text{GeV}$ beam energy is obtained from the AHCAL-38 data set, while the energy range between 1 and $6\,\text{GeV}$ corresponds to measurements performed with the Minical (cf. section 6.4). Fitting the AHCAL-38 distribution with equation 4.24 results in:

$$\left.\frac{\sigma_E}{E}\right|^{\text{em}}_{\text{AHCAL-38}} = \frac{(19.0 \pm 1.6)\,\%}{\sqrt{E\,[\text{GeV}]}} \oplus \frac{0.28\,\text{GeV}}{E\,[\text{GeV}]} \oplus (2.7 \pm 0.4)\,\%. \qquad (7.2)$$

The noise parameter is fixed to the noise estimation from random trigger events (cf. section 7.6.1).

As shown in figure 7.20, the obtained energy resolution is well in agreement with the

measurements from the Minical, which is to be expected since it has the same sampling structure. The resolution obtained from Monte Carlo simulation is slightly better:

$$\left.\frac{\sigma_E}{E}\right|_{\mathrm{MC}}^{\mathrm{em}} = \frac{(18.2 \pm 0.6)\,\%}{\sqrt{E\,[\mathrm{GeV}]}} \oplus (0.5 \pm 1.0)\,\%. \tag{7.3}$$

The Monte Carlo is fitted without noise term, since the random trigger events that are used to simulate noise in the digitisation, are the same that are later on subtracted during the reconstruction. Although the Monte Carlo includes digitisation steps, which should make it agree with the data resolution, some aspects of detector response are still missing. A smearing of the calibration constants due to the different voltage and temperature conditions during calibration and data taking (cf. section 6.3.4) should improve the agreement between data and Monte Carlo.

The obtained AHCAL-38 resolution is a bit worse than the resolution of the Si-W ECAL [63]:

$$\left.\frac{\sigma_E}{E}\right|_{\mathrm{SiW\ ECAL}}^{\mathrm{em}} = \frac{(16.6 \pm 0.1)\,\%}{\sqrt{E\,[\mathrm{GeV}]}} \oplus (1.1 \pm 0.1)\,\%, \tag{7.4}$$

which is optimised to measure electromagnetic showers.

The ILD calorimeter design resolution in table 4.2 is stated for hadronic showers. The presented detector understanding of the electromagnetic showers is sufficient to proceed towards hadronic shower analyses, especially since the average hit energy in hadronic showers is much less. Therefore, remaining non-linearities do not severely effect hadronic shower analyses. The hadronic energy resolution of the AHCAL-38 is measured to be [124]

$$\left.\frac{\sigma_E}{E}\right|_{\mathrm{AHCAL\text{-}38}}^{\mathrm{had}} = \frac{(61.3 \pm 0.1)\,\%}{\sqrt{E\,[\mathrm{GeV}]}} \oplus (2.5 \pm 0.1)\,\%. \tag{7.5}$$

Using a simple weighting technique based on the energy deposition per hit, it can be improved to the currently best value of [124]

$$\left.\frac{\sigma_E}{E}\right|_{\mathrm{AHCAL\text{-}38}}^{\mathrm{had}} = \frac{(49.2 \pm 0.4)\,\%}{\sqrt{E\,[\mathrm{GeV}]}} \oplus \frac{(0.50 \pm 0.04)\,\mathrm{GeV}}{E\,[\mathrm{GeV}]} \oplus (2.3 \pm 0.1)\,\%, \tag{7.6}$$

which is well in agreement with the design resolution.

7.6.4 Longitudinal Shower Development

The maximum shower depth t_{max} (cf. equation 4.8) and the shower attenuation λ_{att} (cf. equation 4.9) can be extracted from the fit (cf. equation 4.7) to the longitudinal profile.

As expected, the shower maximum scales linearly with the logarithm of the beam energy. The error bars shown in figure 7.21 accounts for the statistical uncertainty from the fit and the systematical uncertainty on the MIP calibration coefficient. The shower maximum, plotted in figure 7.21(a), scales with the incoming particle energy as

$$
\begin{aligned}
t_{\mathrm{max}}(\text{AHCAL-38}) &= (0.83 \pm 0.08) \cdot \ln E + (2.61 \pm 0.30), & (7.7)\\
t_{\mathrm{max}}(\text{MC}) &= (1.03 \pm 0.03) \cdot \ln E + (2.25 \pm 0.09). & (7.8)
\end{aligned}
$$
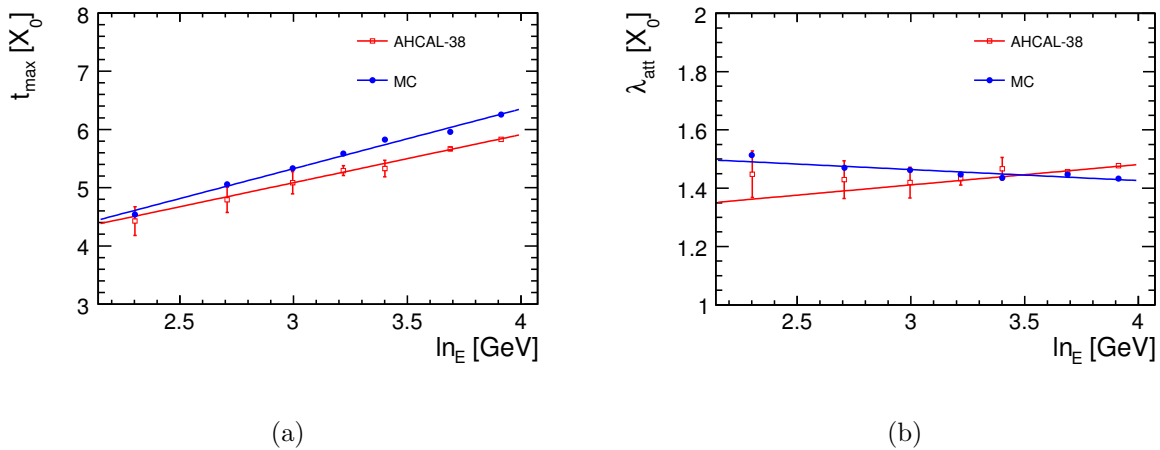
Figure 7.21: Comparison between data (orange squares) and Monte Carlo (blue circles): (a) maximum shower depth t_{max} and (b) shower attenuation factor λ_{att} as a function of beam energy.

Just as for the AHCAL-15 data set, data systematically lies below Monte Carlo predictions around the shower maximum. This effect can be explained by the underestimation of the total absorber material in the simulation (cf. section 7.5).

The shower attenuation is plotted in figure 7.21(b) as a function of the logarithm of the beam energy. The dependence between shower attenuation length and logarithm of the beam energy is found to scale linearly as

$$
\begin{aligned}
\lambda_{\mathrm{att}}(\text{AHCAL-38}) &= (0.07 \pm 0.02) \cdot \ln E + (1.20 \pm 0.06), & (7.9) \\
\lambda_{\mathrm{att}}(\text{MC}) &= (-0.038 \pm 0.003) \cdot \ln E + (1.58 \pm 0.01). & (7.10)
\end{aligned}
$$

The attenuation length is expected to have an almost energy independent scaling, because at large depth the energy deposition of shower cascades is mainly due to low-energy photons, which are attenuated with the corresponding attenuation length. The small rise of the attenuation length with increasing beam energy in data confirms this assumption and is in agreement with other studies [119]. However, in the simulation the attenuation length decreases with increasing energy. Whether this effect results from the wrong absorber plate thickness in the simulation, remains the topic of future investigations.

7.7 Conclusions

The results of the electromagnetic analysis presented in this chapter are a measure of the understanding of the AHCAL. The calibration procedure for a calorimeter with 7608 SiPMs are established and tested with electromagnetic showers. The influence of the calibration ingredients (i. e. the SiPM gain, the most probable signal of a muon, the electronics intercalibration factor, the inter-tile optical crosstalk, the noise, the non-linearity correction) on the reconstruction of electromagnetic showers is investigated, and the achieved AHCAL performance is presented.

Special emphasis is given to the non-linearity correction, which is a key issue for the calibration to the electromagnetic energy scale. A common parametrisation function for all SiPMs would be an elegant solution. However, the large variation in the parameters of the employed SiPMs (e. g. inter-pixel crosstalk, effective number of pixels, gain) makes this method unpractical for the AHCAL.

The response curves of all SiPMs are measured on a test bench and can be used to individually correct each calorimeter cell. Since data are collected with different electronics, the response curves need to be calibrated to an electronics independent scale. This scale is chosen to be the SiPM pixel scale. This calibration step requires the knowledge of the SiPM gain and the determination of the effectively available number of pixels. The uncertainty of these calibration coefficients impact the precision of the non-linearity correction. By the time this thesis is written, the SiPM gain is known at a precision of better than 1%, while for the presented analysis the uncertainty on the SiPM gain was estimated to be 2%. The effectively available number of pixels is by now assumed to be 80% of the number obtained in the test bench measurements. However, this re-scaling of measured response curves is not included in the presented results.

The calibration scheme presented in this analysis achieves a linearity of better than 3% (8%) below $30\,\mathrm{GeV}$ ($50\,\mathrm{GeV}$) beam energy.

The data reconstruction is compared with digitised Monte Carlo simulations. The agreement is at the level of 1% for low beam energies, while the remaining non-linearity leads to deviations at higher hit energies. The main focus of the AHCAL is the investigation of hadronic showers, which have a lower average energy deposition per hit. Thus, the presented agreement between data and Monte Carlo is sufficient to proceed to detailed hadron shower analyses.

The stability of the AHCAL in time is investigated by comparing two independent data sets recorded with one year separation. Special attention is given to the noise situation. The noise level improves in the investigated time slot, since the detector understanding improves with time and problems that occurred during the beginning of the production have been solved in the mean time. The achieved noise occupancy of $1 \cdot 10^{-3}$ is still a factor 10 higher than the design goal. Recent progress on SiPM parameters indicates that the design goal can be accomplished in future prototypes.

The electromagnetic energy resolution of the AHCAL-38 is $\sigma_E/E = 19.0\%/\sqrt{E} \oplus 0.28\,\mathrm{GeV}/E \oplus 2.7\%$, which is comparable to the resolution achieved with an earlier prototype with the same sampling structure.

8 Summary and Outlook

This thesis focuses on two major steps in the optimisation of a calorimetric system that meets the high demands of precision physics at the future linear collider ILC. The philosophy behind this detector development, known as particle flow, demands high spatial resolution rather than excellent energy resolution. During the optimisation process the development of hardware and software are interlinked and only the combination of both can be evaluated. In the first part, this thesis investigated the potential performance of the electromagnetic calorimeter using the example of neutralino decays in a full simulation study. Complementary to this software based study, the second part of this thesis focuses on the analysis of electromagnetic showers from test beam data in a prototype for an analogue hadron calorimeter.

8.1 Summary of the $\tilde{\chi}_1^0$ Analysis

The measurement of the properties from neutralinos that decay into a photon and a gravitino in a gauge-mediated Supersymmetry breaking scenario requires a good energy resolution, as well as excellent position and angular resolution. Thus, this channel is challenging all performance requirements of the electromagnetic calorimeter.

The measurements of the neutralino mass from the kinematic edge of the photon energy distribution depends on the energy resolution, which is measured to be $\sigma/E = 16.7\,\%/\sqrt{E\,[\mathrm{GeV}]} \oplus 0.61\,\%$. The neutralino mass is determined as $126.5 \pm 2.6\,\mathrm{GeV}$. Although the relative error of $2\,\%$ is acceptable, the absolute scale does not meet the expected mass of $151\,\mathrm{GeV}$. This discrepancy is most likely due to beamstrahlung and initial state radiation, which are simulated but not corrected for during reconstruction.

As the initial neutralino conditions are well defined at a lepton collider, the lifetime of each individual neutralino can be reconstructed from the photon shower centre of gravity and its principal axis of inertia. Thus, the position and angular reconstruction of neutral particles are essential for this analysis. They are found to be $\sigma_{\langle \vec{x} \rangle} = 0.4\,\mathrm{cm}/\sqrt{E\,[\mathrm{GeV}]} + 0.8\,\mathrm{cm}$ and $131\,\mathrm{mrad}/\sqrt{E\,[\mathrm{GeV}]} \oplus 3.7\,\mathrm{mrad}$, respectively. With this performance the neutralino lifetime can be measured with an accuracy better than $10\,\%$ for lifetimes between a few tenths to a few tens nanoseconds. At smaller lifetimes, the reconstruction is limited by the angular reconstruction, while at higher lifetimes the reconstruction is limited by the size of the calorimeter.

The analysis can be improved by the implementation of beamstrahlung and initial state radiation in the photon reconstruction. Furthermore, the current angular reconstruction shows a systematic shift in the correlation between true and reconstructed angle. This shift has to be cancelled, either by improving the clustering algorithm or by a calibration utilising the simulation information. A next interesting step would be a scan of the GMSB parameter space, to give a better estimate on the physics potential of this analysis.

8.2 Summary of the AHCAL Analysis

The realisation of a hadron calorimeter with several million readout channels, operated inside a 3.5 T magnetic field, requires the development of new readout techniques. The applied photosensors, so-called SiPMs, are pixelated sensors consisting of an array of avalanche photodiodes operated in Geiger mode. The SiPM response corresponds to the number of fired pixels, which is proportional to the amount of incident light. As the number of pixels available is limited and each pixel has a finite recovery time, the SiPM response saturates at high light intensities.

A cubic metre sized physics prototype with 7608 SiPMs was built and tested in beams of well defined particle type and energy. The investigation of electromagnetic showers serves as calibration validation. Special attention is paid towards the non-linearity correction. The achieved linearity in data was established to within 3 % for beam energies below 30 GeV. The energy resolution of the AHCAL to electromagnetic showers is measured to be $\sigma/E = 19.0\,\%/\sqrt{E\,[\mathrm{GeV}]} \oplus 0.28\,\mathrm{GeV}/E\,[\mathrm{GeV}] \oplus 2.7\,\%$, which is in good agreement to measurements with earlier prototypes of the same sampling structure and readout technology.

In the mean time, the non-linearity correction method has been improved. Inclusion of temperature effects and re-scaling the test bench curves used for the non-linearity correction improved the linearity to better than 2 % for beam energies up to 50 GeV. Also, the discrepancy between data and simulation in the longitudinal profiles has been resolved meanwhile. After inclusion of the true absorber plate thickness in the simulation, the shower development in data and simulation agree to within 1 %.

It has to be noted that the average energy deposition within a single cell in hadronic showers is much lower than that in the electromagnetic shower studied here. The remaining non-linearity at high amplitudes is therefore negligible for studies of hadronic shower properties.

List of Tables

List of Figures

Bibliography

[1] S. L. Glashow. Partial Symmetries of Weak Interactions. *Nucl. Phys.*, 22:579–588, 1961. `doi:10.1016/0029-5582(61)90469-2`.

[2] A. Salam and J. C. Ward. Electromagnetic and Weak Interactions. *Phys. Lett.*, 13:168–171, 1964. `doi:10.1016/0031-9163(64)90711-5`.

[3] S. Weinberg. A Model of Leptons. *Phys. Rev. Lett.*, 19:1264–1266, 1967. `doi:10.1103/PhysRevLett.19.1264`.

[4] C. Amsler et al. Review of Particle Physics. *Phys. Lett.*, B667:1, 2008. `doi:10.1016/j.physletb.2008.07.018`.

[5] H. Fritzsch, M. Gell-Mann, and H. Leutwyler. Advantages of the Color Octet Gluon Picture. *Phys. Lett.*, B47:365–368, 1973. `doi:10.1016/0370-2693(73)90625-4`.

[6] E. Noether. Invarianten beliebiger Differentialausdrücke. *Nachr. Königl. Ges. Wiss. Göttingen*, pages 37–44, 1918.

[7] N. Cabibbo. Unitary Symmetry and Leptonic Decays. *Phys. Rev. Lett.*, 10:531–533, 1963. `doi:10.1103/PhysRevLett.10.531`.

[8] M. Kobayashi and T. Maskawa. CP Violation in the Renormalizable Theory of Weak Interaction. *Prog. Theor. Phys.*, 49:652–657, 1973. `doi:10.1143/PTP.49.652`.

[9] P. W. Higgs. Broken Symmetries, Massless Particles and Gauge Fields. *Phys. Lett.*, 12:132–133, 1964. `doi:10.1016/0031-9163(64)91136-9`.

[10] F. Englert and R. Brout. Broken Symmetry and the Mass of Gauge Vector Mesons. *Phys. Rev. Lett.*, 13:321–322, 1964. `doi:10.1103/PhysRevLett.13.321`.

[11] G. S. Guralnik, C. R. Hagen, and T. W. B. Kibble. Global Conservation Laws and Massless Particles. *Phys. Rev. Lett.*, 13:585–587, 1964. `doi:10.1103/PhysRevLett.13.585`.

[12] J. Goldstone, A. Salam, and S. Weinberg. Broken symmetries. *Phys. Rev.*, 127(3):965–970, Aug 1962. `doi:10.1103/PhysRev.127.965`.

[13] R. Barate et al. Search for the Standard Model Higgs boson at LEP. *Phys. Lett.*, B565:61–75, 2003. `arXiv:hep-ex/0306033`.

[14] The CDF Collaboration, the D0 Collaboration, the Tevatron New Physics, and Higgs Working Group. Combined CDF and D0 Upper Limits on Standard Model Higgs boson Production with $2.1 - 5.4\,\mathrm{fb}^{-1}$ of Data. 2009. `arXiv:0911.3930`.

[15] M. Goebel. Global Fits of the Electroweak Standard Model and Beyond with Gfitter. 2009. `arXiv:0905.2488`.

[16] S. Dimopoulos and H. Georgi. Softly Broken Supersymmetry and SU(5). *Nucl. Phys.*, B193:150, 1981. `doi:10.1016/0550-3213(81)90522-8`.

[17] S. P. Martin. A Supersymmetry Primer. 1997. `arXiv:hep-ph/9709356`.

[18] S. Weinberg. Implications of Dynamical Symmetry Breaking. *Phys. Rev.*, D13:974–996, 1976. `doi:10.1103/PhysRevD.13.974`.

[19] D. Bailin. Cosmology in Gauge Field Theory and Stringtheory. *Institute of Physics Publishing*, 2004.

[20] E. Komatsu et al. Five-Year Wilkinson Microwave Anisotropy Probe (WMAP) Observations: Cosmological Interpretation. *Astrophys. J. Suppl.*, 180:330–376, 2009. `arXiv:0803.0547`.

[21] H. Murayama. Physics Beyond the Standard Model and Dark Matter. 2007. `arXiv:0704.2276`.

[22] C. T. Hill and E. H. Simmons. Strong Dynamics and Electroweak Symmetry Breaking. *Phys. Rept.*, 381:235–402, 2003. `arXiv:hep-ph/0203079`.

[23] L. Randall and R. Sundrum. An Alternative to Compactification. *Phys. Rev. Lett.*, 83:4690–4693, 1999. `arXiv:hep-th/9906064`.

[24] J. Wess and B. Zumino. Supergauge Transformations in Four-Dimensions. *Nucl. Phys.*, B70:39–50, 1974. `doi:10.1016/0550-3213(74)90355-1`.

[25] C. D. Anderson. The Positive Electron. *Phys. Rev.*, 43:491–494, 1933. `doi:10.1103/PhysRev.43.491`.

[26] V. F. Weisskopf. On the self-energy and the electromagnetic field of the electron. *Phys. Rev.*, 56(1):72–85, Jul 1939. `doi:10.1103/PhysRev.56.72`.

[27] I. Simonsen. A Review of Minimal Supersymmetric Electroweak Theory. 1995. `arXiv:hep-ph/9506369`.

[28] A. Djouadi. The Anatomy of Electro-Weak Symmetry Breaking. II. The Higgs bosons in the Minimal Supersymmetric Model. *Phys. Rept.*, 459:1–241, 2008. `arXiv:hep-ph/0503173`.

[29] H. Nishino et al. Search for Proton Decay via $p \rightarrow e^+\pi^0$ and $p \rightarrow \mu^+\pi^0$ in a Large Water Cherenkov Detector. *Phys. Rev. Lett.*, 102:141801, 2009. `arXiv:0903.0676`.

[30] S. Dimopoulos, M. Dine, S. Raby, and S. D. Thomas. Experimental Signatures of Low Energy Gauge Mediated Supersymmetry Breaking. *Phys. Rev. Lett.*, 76:3494–3497, 1996. `arXiv:hep-ph/9601367`.

[31] J. L. Feng and T. Moroi. Tevatron Signatures of Longlived Charged Sleptons in Gauge Mediated Supersymmetry Breaking Models. *Phys. Rev.*, D58:035001, 1998. `arXiv:hep-ph/9712499`.

[32] P. Bechtle, K. Desch, M. Uhlenbrock, and P. Wienemann. Constraining SUSY Models with Fittino using Measurements Before, With and Beyond the LHC. 2009. `arXiv:0907.2589`.

[33] A. Garcia-Bellido. Searches for Gauge Mediated Supersymmetry Breaking at ALEPH with Center-of-Mass Energies up to 209 GeV. 2002. `arXiv:hep-ex/0212024`.

[34] J. Abdallah et al. Photon Events with Missing Energy in e^+e^- Collisions at $\sqrt{s} = 130$ GeV to 209 GeV. *Eur. Phys. J.*, C38:395–411, 2005. `arXiv:hep-ex/0406019`.

[35] M. Gataullin, S. Rosier, L. Xia, and H. Yang. Searches for Gauge-Mediated SUSY Breaking Topologies with the L3 Detector at LEP. *AIP Conf. Proc.*, 903:217–220, 2007. `arXiv:hep-ex/0611010`.

[36] G. Abbiendi et al. Searches for Gauge-Mediated Supersymmetry Breaking Topologies in e^+e^- Collisions at LEP2. *Eur. Phys. J.*, C46:307–341, 2006. `arXiv:hep-ex/0507048`.

[37] D. E. Acosta et al. Search for Anomalous Production of Diphoton Events with Missing Transverse Energy at CDF and Limits on Gauge- Mediated Supersymmetry-Breaking Models. *Phys. Rev.*, D71:031104, 2005. `arXiv:hep-ex/0410053`.

[38] S.-S. Eiko Yu. Searches for New Physics at the Tevatron in Photon and Jet Final States. 2009. `arXiv:0905.2285`.

[39] V. M. Abazov et al. Search for Supersymmetry with Gauge-Mediated Breaking in Diphoton Events at D0. *Phys. Rev. Lett.*, 94:041801, 2005. `arXiv:hep-ex/0408146`.

[40] R. L. Culbertson et al. Low-Scale and Gauge-Mediated Supersymmetry Breaking at the Fermilab Tevatron Run II. 2000. `arXiv:hep-ph/0008070`.

[41] M. Terwort. Study of GMSB Models with Photon Final States using the ATLAS Detector. 2009. DESY-THESIS-2009-033.

[42] M. Terwort. Searches for GMSB at the LHC. 2008. `arXiv:0805.2524`.

[43] G. Moultaka. Very Light Gravitino Dark Matter. *Acta Phys. Polon.*, B38:645–652, 2007. `arXiv:hep-ph/0612331`.

[44] J. R. Primack. Whatever Happened to Hot Dark Matter? *SLAC Beam Line*, 31N3:50–57, 2001. `arXiv:astro-ph/0112336`.

[45] M. Fujii and T. Yanagida. Natural Gravitino Dark Matter and Thermal Leptogenesis in Gauge-Mediated Supersymmetry-Breaking Models. *Phys. Lett.*, B549:273–283, 2002. `arXiv:hep-ph/0208191`.

[46] A. de Gouvea, T. Moroi, and H. Murayama. Cosmology of Supersymmetric Models with Low-Energy Gauge Mediation. *Phys. Rev.*, D56:1281–1299, 1997. `arXiv:hep-ph/9701244`.

[47] J. Brau et al. International Linear Collider Reference Design Report. 1: Executive Dummary. 2: Physics at the ILC. 3: Accelerator. 4: Detectors. 2007. ILC-REPORT-2007-001.

[48] G. A. Moortgat-Pick et al. The Role of Polarized Positrons and Electrons in Revealing Fundamental Interactions at the Linear Collider. *Phys. Rept.*, 460:131–243, 2008. `arXiv:hep-ph/0507011`.

[49] A. Vogel. Beam-Induced Backgrounds in Detectors at the ILC. 2008. DESY-THESIS-2008-036.

[50] Combination of CDF and D0 Results on the Mass of the Top Quark. 2009. `arXiv:0903.2503`.

[51] ILD Concept Group. The International Large Detector – Letter of Intent. 2009. `arXiv:hep-ex/0908`.

[52] ATLAS Collaboration. ATLAS Detector and Physics Performance. Technical Design Report. Vol. 2. 1999. CERN-LHCC-99-15.

[53] G. L. Bayatian et al. CMS Physics: Technical Design Report. 2006. CERN-LHCC-2006-001.

[54] A. Djouadi. The Anatomy of Electro-Weak Symmetry Breaking. I: The Higgs boson in the Standard Model. *Phys. Rept.*, 457:1–216, 2008. `arXiv:hep-ph/0503172`.

[55] P. Garcia-Abia, W. Lohmann, and A. Raspereza. Measurement of the Higgs boson Mass with a Linear e^+e^- Collider. 2005. `arXiv:hep-ex/0505096`.

[56] J. L. Feng. Dark Matter at the Fermi Scale. *J. Phys.*, G32:R1, 2006. `arXiv:astro-ph/0511043`.

[57] J. R. Bond, G. Efstathiou, and M. Tegmark. Forecasting Cosmic Parameter Errors from Microwave Background Anisotropy Experiments. *Mon. Not. Roy. Astron. Soc.*, 291:L33–L41, 1997. `arXiv:astro-ph/9702100`.

[58] M. Oreglia (editors) H. Aihara, P. Burrows. Silicon Detector Letter of Intent, 2009. `arXiv:hep-ex/0911.0006v1`.

[59] M. A. Thomson. Particle Flow Calorimetry at the ILC. *AIP Conf. Proc.*, 896:215–224, 2007.

[60] T. Behnke, S. Bertolucci, R. D. Heuer, and R. (editors) Settles. TESLA: The Superconducting Electron Positron Linear Collider with an Integrated X-ray Laser Laboratory. Technical Design Report. Pt. 4: A Detector for TESLA. 2001. DESY-01-011.

[61] F. E. Taylor. Design and Performance of a 307 Million Pixel CCD Vertex Detector. 1996. Prepared for 28th International Conference on High-energy Physics (ICHEP 96), Warsaw, Poland, 25-31 Jul 1996.

[62] D. Buskulic et al. Performance of the ALEPH Detector at LEP. *Nucl. Instrum. Meth.*, A360:481–506, 1995. `doi:10.1016/0168-9002(95)00138-7`.

[63] C. Adloff et al. Response of the CALICE Si-W Electromagnetic Calorimeter Physics Prototype to Electrons. *J. Phys. Conf. Ser.*, 160:012065, 2009. `arXiv:0811.2354`.

[64] B. Bilki et al. Measurement of Positron Showers with a Digital Hadron Calorimeter. *JINST*, 4:P04006, 2009. `arXiv:0902.1699`.

[65] R. Settles and W. Wiedenmann. The Linear Collider TPC: Revised Magnetic-field Requirements. Technical Report LC-DET-2008-002, LC Note, August 2008.

[66] H. Bethe and W. Heitler. On the Stopping of Fast Particles and on the Creation of Positive Electrons. *Proc. Roy. Soc. Lond.*, A146:83–112, 1934.

[67] U. Amaldi. Fluctuations in Calorimetry Measurements. *Phys. Scripta*, 23:409, 1981. `doi:10.1088/0031-8949/23/4A/012`.

[68] E. Segre. Nuclei and Particles. *Benjamin*, page 65ff, 1964.

[69] H. Bethe. Zur Theorie des Durchgangs schneller Korpuskelstrahlen durch Materie. *Annalen Phys.*, 5:325–400, 1930.

[70] P. M. S. Blackett and G. P. S. Occhialini. Some Photographs of the Tracks of Penetrating Radiation. *Proc. R. Soc.*, 139:699–729, 1933.

[71] Particle Data Group. Atomic and Nuclear Properties of Materials. Available from: `http://pdg.web.cern.ch/pdg/2009/AtomicNuclearProperties/`.

[72] B. Rossi and K. Greisen. Cosmic-Ray Theory. *Rev. Mod. Phys.*, 13(4):240–309, Oct 1941. `doi:10.110/RevModPhys.13.240`.

[73] C. Leroy and P. Rancoita. Physics of Cascading Shower Generation and Propagation in Matter: Principles of High-Energy, Ultrahigh-Energy and Compensating Calorimetry. *Rept. Prog. Phys.*, 63:505–606, 2000.

[74] R. Wigmans. Calorimetry: Energy measurement in particle physics. *Int. Ser. Monogr. Phys.*, 107:1–726, 2000.

[75] C. W. Fabjan. Calorimetry in High-Energy Physics. *NATO Adv. Study Inst. Ser. B Phys.*, 128:281, 1985.

[76] F. Simon. Track Segments in Hadronic Showers: Calibration Possibilities for a Highly Granular HCAL. 2009. `arXiv:0902.1879`.

[77] P. Krstonosic. Measurement of Quartic Boson Couplings at the International Linear Collider and Study of Novel Particle Flow Algorithms. 2008. DESY-THESIS-2008-007.

[78] G. Grindhammer, M. Rudowicz, and S. Peters. The Fast Simulation of Electromagnetic and Hadronic Showers. *Nucl. Instrum. Meth.*, A290:469, 1990. `doi:10.1016/0168-9002(90)90566-O`.

[79] J. Engler. Perspectives in Calorimetry. *Nucl. Instrum. Meth.*, A235:301–309, 1985. `doi:10.1016/0168-9002(85)90568-6`.

[80] B. Lutz. Test Beam Results from the CALICE Tile Hadron Calorimeter Prototype with SiPM Read-Out. *IEEE Trans. Nucl. Sci.*, 2008.

[81] K. Ahmet et al. The OPAL Detector at LEP. *Nucl. Instrum. Meth.*, A305:275–319, 1991. `doi:10.1016/0168-9002(91)90547-4`.

[82] D. Buskulic et al. Performance of the ALEPH Detector at LEP. *Nucl. Instrum. Meth.*, A360:481–506, 1995. `doi:10.1016/0168-9002(95)00138-7`.

[83] M. Aharrouche et al. Energy Linearity and Resolution of the ATLAS Electromagnetic Barrel Calorimeter in an Electron Test-Beam. *Nucl. Instrum. Meth.*, A568:601–623, 2006. `arXiv:physics/0608012`.

[84] S. Akhmadalev et al. Hadron Energy Reconstruction for the ATLAS Calorimetry in the Framework of the Non-Parametrical Method. *Nucl. Instrum. Meth.*, A480:508–523, 2002. `arXiv:hep-ex/0104002`.

[85] M. Ryan. The CMS Electromagnetic Calorimeter at the LHC. *Nucl. Instrum. Meth.*, A598:217–219, 2009. `doi:10.1016/j.nima.2008.08.103`.

[86] A. Bodek. Performance of a Prototype CMS Hadron Barrel Calorimeter in a Test Beam. *IEEE Trans. Nucl. Sci.*, 46:407–409, 1999. `arXiv:hep-ex/9810033`.

[87] A. Baroncelli. Study of Total-Absorption Counters for Very-High-Energy Particles. *Nucl. Instrum. Meth.*, 118:445–451, 1974. `doi:10.1016/0029-554X(74)90649-1`.

[88] R. Wigmans. On the Energy Resolution of Uranium and Other Hadron Calorimeters. *Nucl. Instrum. Meth.*, A259:389–429, 1987. `doi:10.1016/0168-9002(87)90823-0`.

[89] M. Barbi. Calibration and Monitoring of the ZEUS Uranium Scintillator Calorimeter at HERA. 2002. Prepared for 10th International Conference on Calorimetry in High Energy Physics (CALOR 2002), Pasadena, California, 25-30 Mar 2002.

[90] W. Porod. SPheno, a Program for Calculating Supersymmetric Spectra, SUSY Particle Decays and SUSY Particle Production at e^+e^- Colliders. *Comput. Phys. Commun.*, 153:275–315, 2003. `arXiv:hep-ph/0301101`.

[91] M. Battaglia et al. Physics Benchmarks for the ILC Detectors. 2006. `arXiv:hep-ex/0603010`.

[92] W. Kilian, T. Ohl, and J. Reuter. WHIZARD: Simulating Multi-Particle Processes at LHC and ILC. 2007. `arXiv:0708.4233`.

[93] W. Kilian. WHIZARD 1.0: A Generic Monte-Carlo Integration and Event Generation Package for Multi-Particle Processes. Manual. 2001. LC-TOOL-2001-039.

[94] M. Moretti, T. Ohl, and J. Reuter. O'Mega: An Optimizing Matrix Element Generator. 2001. `arXiv:hep-ph/0102195`.

[95] D. Schulte. *Study of Electromagnetic and Hadronic Background in the Interaction Region of the TESLA Collider*. PhD thesis, 1996. TESLA 1997-08.

[96] T. Barklow. Standard Model Data Samples web site. Available from: `http://confluence.slac.stanford.edu/display/ilc/`.

[97] T. Sjöstrand, S. Mrenna, and P. Skands. PYTHIA 6.4 Physics and Manual. *JHEP*, 05:026, 2006. `arXiv:hep-ph/0603175`.

[98] P. Mora de Freitas and H. Videau. Detector Simulation with Mokka and Geant4: Present and Future. Technical Report LC-TOOL-2003-010, LC Note, March 2003.

[99] The Geant4 Collaboration, S. Agostinelli, et al. Geant4: A Simulation Toolkit. *Nucl. Instrum. Meth.*, A506:250–303, 2003. `doi:10.1016/S0168-9002(03)01368-8`.

[100] F. Gaede. Marlin and LCCD: Software Tools for the ILC. *Nucl. Instrum. Meth.*, A559:177–180, 2006. `doi:10.1016/j.nima.2005.11.138`.

[101] O. Wendt, F. Gaede, and T. Krämer. Event Reconstruction with MarlinReco at the ILC. *Pramana*, 69:1109–1114, 2007. `arXiv:physics/0702171`.

[102] M. Gianelli. Study of Position and Angular Resolution for Electron Showers Measured with the Electromagnetic SiW Prototype. *IEEE Trans. Nucl. Sci.*, 2009.

[103] S. Ambrosanio and G. A. Blair. Measuring Gauge-Mediated Supersymmetry Breaking Parameters at a $500\,\text{GeV}$ e^+e^- Linear Collider. *Eur. Phys. J.*, C12:287–321, 2000. `arXiv:hep-ph/9905403`.

[104] W. Verkerke and D. Kirkby. The RooFit Toolkit for Data Modeling. 2003. `arXiv:physics/0306116`.

[105] J. Repond et al. Design and Electronics Commissioning of the Physics Prototype of a Si-W Electromagnetic Calorimeter for the International Linear Collider. *JINST*, 3:P08001, 2008. `arXiv:0805.4833`.

[106] A. Dyshkant. The Tail-Catcher/Muon Tracker for the CALICE Test Beam. *AIP Conf. Proc.*, 867:592–599, 2006. `doi:10.1063/1.2397001`.

[107] F. Salvatore. The CALICE Test Beam Programme. *J. Phys. Conf. Ser.*, 160:012064, 2009. `doi:10.1088/1742-6596/160/1/012064`.

[108] C. Adloff et al. Construction and Commissioning of the CALICE Analog Hadron Calorimeter Prototype. *to be published in JINST*, 2010.

[109] S. Manen et al. Dedicated Front-End Electronics for the Next Generation of Linear Collider Electromagnetic Calorimeter. 2005. `arXiv:physics/0501063`.

[110] P. D. Dauncey. CALICE Electromagnetic Calorimeter Readout Status. 2004. `arXiv:hep-ex/0410001`.

[111] M. Danilov. Scintillator Tile Hadron Calorimeter with Novel SiPM Readout. *Nucl. Instrum. Meth.*, A582:451–456, 2007. `arXiv:0704.3514`.

[112] B. Dolgoshein et al. Status Report on Silicon Photomultiplier Development and its Applications. *Nucl. Instrum. Meth.*, A563:368–376, 2006.

[113] N. Wattimena. Commissioning of an LED Calibration and Monitoring System for the Prototype of a Hadronic Calorimeter. 2006. DESY-THESIS-2006-039.

[114] V. Andreev et al. A High Granularity Scintillator Hadronic-Calorimeter with SiPM Readout for a Linear Collider Detector. *Nucl. Instrum. Meth.*, A540:368–380, 2005.

[115] P. Eckert et al. Characterisation Studies of Silicon Photomultipliers for a Calorimeter for the ILC. In the Proceedings of the 2009 International Workshop on new Photon Detectors (PD09), Shinshu, Japan, 24-26 June 2009.

[116] Philips. Philips Data Handbook. Technical Report PC04, 1990.

[117] N. Feege. Silicon Photomultipliers: Properties and Application in a Highly Granular Calorimeter. 2008. DESY-THESIS-2008-050.

[118] M. Groll. Dedicated Front-End Electronics for an ILC Prototype Hadronic Calorimeter with SiPM Readout. 2005. Prepared for 9th ICATPP Conference on Astroparticle, Particle, Space Physics, Detectors and Medical Physics Applications, Villa Erba, Como, Italy, 17-21 Oct 2005.

[119] M. Groll. Construction and Commissioning of a Hadronic Test-Beam Calorimeter to Validate the Particle-Flow Concept at the ILC. 2007. DESY-THESIS-2007-018.

[120] N. D'Ascenzo. Study of the Neutralino Sector and Analysis of the Muon Response of a Highly Granular Hadron Calorimeter at the International Linear Collider. 2009. DESY-THESIS-2009-004.

[121] B. Lutz. Commissioning of the Readout Electronics for the Prototypes of a Hadronic Calorimeter and a Tailcatcher and Muon Tracker. 2006. DESY-THESIS-2006-038.

[122] S. Richter. Validation of the Calibration Procedure for a Highly Granular Calorimeter with Electromagnetic Processes. 2008.

[123] V. Morgunov. ITEP Activity on HCAL Prototype Cassette Mass Production. 2004. Presentation at the ECFA Workshop (ECFA 04), Durham, England, 1-4 Sept. 2004.

[124] F. Simon. Hadronic Showers in the CALICE Calorimeter Prototypes. 2009. `arXiv:0904.2991`.

Acknowledgements